UNIVERSITY OF OKLAHOMA

GRADUATE COLLEGE

NEW PHYSICS IN HEAVENS:
ASTROPHYSICAL PROBES OF THE DARK UNIVERSE

A DISSERTATION

SUBMITTED TO THE GRADUATE FACULTY

in partial fulfillment of the requirements for the

Degree of

DOCTOR OF PHILOSOPHY

By

BADAL BHALLA
Norman, Oklahoma
2026

NEW PHYSICS IN HEAVENS:
ASTROPHYSICAL PROBES OF THE DARK UNIVERSE

A DISSERTATION APPROVED FOR THE
HOMER L. DODGE DEPARTMENT OF PHYSICS AND ASTRONOMY

BY THE COMMITTEE CONSISTING OF

Dr. Kuver Sinha, Chair

Dr. Brad Abbott

Dr. Howard Baer

Dr. Mukremin Kilic

Dr. Christian Remling

I would like to dedicate this work to my parents, Savita Bhalla and Arvinder Bhalla, who brought me into this world (likely not to pursue physics) and have given me immense love and support throughout the years.

I also dedicate this work to my brother, Dr. Piyush Bhalla, and my grandfather, Har Krishan Bhalla.

Acknowledgements

First and foremost, I would like to thank my advisor, Dr. Kuver Sinha, for shaping me into the researcher I am today. This thesis would not have been possible without his constant support, guidance, and encouragement. A PhD is a challenging journey, and one that is difficult to complete without good mentors. I was very fortunate to have two wonderful mentors, Dr. Tao Xu and Dr. Benjamin Lehmann. I would like to express my deepest gratitude to both of them for patiently listening to me, guiding me, and answering all my questions, no matter how simple they may have seemed. I cannot thank them enough.

I also had the privilege of working with some truly remarkable physicists: Dr. Aurora Ireland, Dr. Hongwan Liu, Dr. Huangyu Xiao, Dr. Doojin Kim, and Dr. Fazlollah Hajkarim. I am deeply grateful to them for their support, encouragement, and for believing in me and in my work. I am especially thankful to Aurora and Hongwan for taking my half-baked ideas seriously and helping me turn them into research papers.

A PhD requires not only intellectual support, but also emotional and mental support. I would therefore like to thank my dear friends Sakshi and Adarsh, as well as my cousins, Varun and Neha Bhandari, for patiently listening to my endless research stories, and being there for me whenever I needed them. Additionally, I would like to thank all the members of the Norman Cricket Club for the fun weekends that helped me stay sane throughout this journey.

Table of Contents

List of Tables

List of Figures

Abstract

Dark matter remains one of the most compelling mysteries in modern physics. Despite decades of effort, its nature and non-gravitational interactions remain unknown. The absence of a definitive direct-detection signal has motivated the exploration of a broad range of dark matter scenarios, including primordial black holes, axion-like particles, and sub-GeV dark matter. At the same time, advances in astrophysical, cosmological, and gravitational-wave observations over the last decade have opened new avenues for probing dark matter. Dark matter may be produced in extreme astrophysical environments, or it may leave observable signatures by modifying, heating, perturbing, or destroying sensitive astrophysical systems.

In this thesis, I develop theoretical and computational frameworks to identify and characterize these signatures. I first show that dynamical friction from dark compact objects and axion minihalos can heat the baryonic gas during the dark ages, producing observable modifications to the global 21-cm signal and its power spectrum. I then study three-body interactions between primordial black holes and binary systems. I demonstrate that although perturbations from fast-moving primordial black holes vanish on average, individual encounters can produce stochastic changes in binary orbits, providing a possible probe of asteroid-mass dark compact objects. I also investigate exchange interactions in which a primordial black hole replaces one member of a binary and show that these processes can produce a small but potentially observable population of binaries containing invisible companions, including systems resembling the black hole binaries observed by Gaia.

I further explore how long-range dark forces can modify the gravitational-wave emission from extreme mass-ratio inspirals. I show that independent mass measurements of the central black hole can break the degeneracies arising from uncertainties in the binary component masses, thereby improving the sensitivity to dark couplings. Finally, I study dark matter produced in core-collapse supernovae and its detection through electron recoils at large-volume neutrino detectors. Together, these studies demonstrate that astrophysical, cosmological, and gravitational-wave observations can probe dark matter across a wide range of masses and interactions, helping unravel its mysteries one signature at a time.

Chapter 1

Dark Matter: From Particles to Compact Objects

"There are more things in heaven and earth, Horatio,

Than are dreamt of in your philosophy."

– William Shakespeare, *Hamlet*

The nature of Dark Matter (DM) remains one of the most puzzling mysteries in modern physics. Evidence for its existence has accumulated for nearly a century, yet all efforts to directly detect it through non-gravitational interactions have so far been unsuccessful. As ideas about what dark matter might be have changed over time, they have reshaped how we search for it and which experiments we build to detect it. In this chapter, I will briefly discuss these ideas, their evolution over the years, and their current status. For a more comprehensive review on DM, see [1, 2, 3, 4].

The existence of dark matter was first postulated by the Swiss astrophysicist Fritz Zwicky [5]. He studied the radial velocities of galaxies in the Coma cluster and found an unexpectedly large velocity dispersion. He attributed this large velocity dispersion to the presence of "dark matter," which must exist in much greater amounts than the visible matter. A similar conclusion was later reached for the Virgo cluster, and by the late 1950s, several papers had studied the mass-to-light ratios of galaxy clusters. These studies all pointed toward the same conclusion: luminous matter alone could not account for the dynamics of galaxies within these clusters. However, the most convincing evidence for dark matter came later from observations of the rotation curves of disk galaxies by Kent Ford and Vera Rubin [6]. They found that the rotation velocities in the outer regions of M31 were much larger than expected from the visible matter alone, indicating the presence of a significant amount of non-luminous matter.

Around the same time, with the development of computational resources, astrophysicists began simulating the gravitational interactions of large numbers of massive particles in order to better understand galaxy evolution. To their surprise, they found that a cold, rotationally supported disk galaxy, such as the Milky Way, is highly unstable. It was later shown by Ostriker and Peebles [7] that a rotationally supported disk can be stabilized if it is embedded in a massive, roughly spherical halo of matter. Since no such halo is directly observed in light, it must be dark. By the 1980s, the instability problem of rotationally supported disk galaxies, together with the observations of flat rotation curves in spiral galaxies, led most astronomers to accept the idea that galaxies are embedded in massive halos of dark matter.

At that time, dark matter was viewed mainly as an astrophysical problem of missing mass. It was thought that the missing matter could be in the form of cold stars, gas, stellar remnants, or other massive collapsed objects. Most of these possibilities were baryonic in nature, meaning that they were made of ordinary matter. Such objects came to be known as MACHOs, which stands for Massive Astrophysical Compact Halo Objects. However, the problem of dark matter soon became deeply connected to particle physics. The Standard Model of particle physics, while accurately describing the strong, weak, and electromagnetic interactions, left many important questions unanswered. For example, is there a theory that unifies these forces at high-energy scales? Are there other fundamental symmetries in nature? Is CP conserved in strong interactions? To answer these questions, many theories of particle physics beyond the Standard Model began to appear, and many of them predicted the existence of massive, stable particles that interact only weakly with Standard Model particles. It was quickly realized that such particles could make up dark matter, thus uniting astrophysics and cosmology with particle physics.

The current consensus is that the dominant component of dark matter must be non-baryonic, whether it consists of particles or compact objects. It should be cold, mostly collisionless, and stable on cosmological timescales. Such candidates may be motivated by physics beyond the Standard Model. Over the years, numerous experiments and observations have searched for dark matter and have significantly improved our understanding of its possible nature. In the following sections, I will briefly discuss some of the most prominent dark matter candidates, the motivations behind them, and their current status.

1.1 Massive Astrophysical Compact Halo Objects

In the early days, as evidence for the existence of dark matter accumulated, one natural possibility was that it consisted of objects that were much less luminous than ordinary stars but still astrophysical in nature, such as brown dwarfs, white dwarfs, neutron stars, and black holes. These objects became famously known as MACHOs. Their masses could span a wide range, from fractions of a solar mass to many solar masses. An obvious way to detect these very faint but massive objects was through gravitational lensing.

Gravitational lensing refers to the deflection of light by massive bodies, as predicted by Einstein's theory of general relativity. It is commonly categorized into three main types: strong lensing, weak lensing, and microlensing. Strong lensing occurs when a massive object lies close to the line of sight between a light source and an observer. In this case, the gravitational field of the lens can cause significant deflection of light, resulting in two or more distinct images of the source being visible to the observer. Weak lensing, on the other hand, occurs when the deflection is small, so that the images of background sources are only slightly distorted. Microlensing occurs when the mass of the lensing object is relatively small, but the source, lens, and observer are aligned. In this case, the multiple images created by the lens cannot be resolved, causing the image to appear brighter during the lensing event.

The search for MACHOs relied on the phenomenon of gravitational microlensing. The strategy involved simultaneously monitoring large numbers of stars in a nearby galaxy in an effort to detect temporary variations in their brightness. This was the approach taken by collaborations such as MACHO, EROS, and OGLE, which carried out extensive microlensing surveys to test the hypothesis that the Milky Way's dark halo consisted of MACHOs. Although these collaborations identified microlensing events, the observed event rate was much lower than expected for a halo dominated by MACHOs. Consequently, in the mass ranges probed by these surveys, MACHOs could account for only a small fraction of the dark matter halo.

Later, measurements of the cosmic microwave background and of the primordial abundances of light elements, which are consistent with Big Bang Nucleosynthesis, implied that the dominant component of dark matter cannot be baryonic. Additionally, null results from microlensing observations made it clear that baryonic MACHOs cannot be the dominant source of dark matter. However, the concept of MACHOs has since broadened to include various non-baryonic possibilities. We will revisit this more general idea in Chapter 2. For now, let us shift our focus to non-baryonic dark compact objects, specifically primordial black holes.

1.2 Primordial Black Holes

Unlike regular astrophysical black holes, which are believed to form predominantly from the gravitational collapse of massive stars, Primordial Black Holes (PBHs) are hypothesized to have formed in the very early Universe. The possibility of black hole formation in the early Universe was first proposed by Yakov Borisovich Zel'dovich and Igor Dmitriyevich Novikov [8] in the 1960s, while Stephen Hawking [9] carried out the first detailed study in 1971. In the early 1970s, the work of Bekenstein, Bardeen, Carter, and Hawking laid the foundations of black hole thermodynamics. This eventually led to the prediction of Hawking radiation, which implies that black holes are not entirely black, but can emit radiation due to quantum effects near the event horizon. A notable aspect of Hawking radiation is that the temperature of a black hole is inversely proportional to its mass. This means that lighter black holes radiate more efficiently than heavier ones. Astrophysical black holes, which are expected to have masses on the order of a solar mass or larger, emit Hawking radiation at an exceedingly low rate, making the effect practically undetectable. The realization that lighter black holes would radiate more intensely motivated Hawking to consider black holes formed in the early Universe through the collapse of enhanced density fluctuations.

Since then, many mechanisms have been proposed for primordial black hole formation [10]. In most scenarios, there is a rough correlation between the mass of a PBH and the mass contained within the cosmological horizon at the time of its formation. This relation can be written as

$$M_{\mathrm{PBH}} \sim \frac{c^3\, t}{G} \sim 10^{15} \left(\frac{t}{10^{-23}\,\mathrm{s}} \right) \mathrm{g}, \tag{1.1}$$

where M_{PBH} is the mass of the PBH, c is the speed of light, t is the time after the Big Bang when the PBH forms, and G is the gravitational constant. Consequently, PBHs could have a vast spectrum of masses. For instance, PBHs that formed around the Planck time, $\sim 10^{-43}\,\mathrm{s}$, would have masses of order the Planck mass, $\sim 10^{-5}\,\mathrm{g}$, whereas those forming about one second after the Big Bang could have masses around $10^5 M_\odot$.

PBHs with initial masses below roughly $10^{15}\,\mathrm{g}$ would have evaporated by now, leaving behind possible observable signatures. Constraints on such PBHs have therefore been established by searching for these evaporative signatures. On the other hand, PBHs with masses well above $10^{15}\,\mathrm{g}$ are much less affected by Hawking radiation and can remain viable dark matter candidates. Such PBHs can have a variety of astrophysical consequences. Sub-solar-mass PBHs can be searched for through gravitational microlensing, while heavier PBHs can be constrained through their dynamical effects on surrounding astrophysical systems. Furthermore, mergers of PBHs would produce gravitational waves, offering another possible avenue for detection.

Existing constraints on the fraction of dark matter in PBHs [10] have excluded PBHs as the dominant component of dark matter over much of the mass range. However, there remains one interesting possibility: the asteroid-mass range, roughly 10^{16}–10^{24} g. These black holes are heavy enough that Hawking radiation is inefficient, but light enough that conventional microlensing searches become challenging. Thus, their direct or indirect detection remains difficult. In Chapter 3, I will present a dynamical way to probe asteroid-mass PBHs. For now, I will end the discussion of dark compact objects here and turn to particle dark matter.

1.3 Weakly Interacting Massive Particles

For much of its early history, most constituents of the Universe existed in thermal equilibrium. However, if the rate of the reaction that maintains a particle in thermal equilibrium falls below the expansion rate of the Universe, the particle decouples from the equilibrium. Once a particle species decouples, its number density decreases only due to the expansion of the Universe, unlike when it is in thermal equilibrium, where the number density decreases exponentially as the temperature falls below the particle's mass. If we assume that dark matter is a particle that was once in thermal equilibrium, we can calculate its thermally averaged annihilation cross section required to produce the correct relic density observed today. For a particle with a mass of approximately 100 GeV, the reaction cross-section required to obtain the correct relic density is about $\mathcal{O}(10^{-26})\,\mathrm{cm}^3\,\mathrm{s}^{-1}$. This value corresponds precisely to the strength of the weak interaction. The apparent coincidence that a thermally coupled dark matter particle in the early Universe must interact weakly, combined with predictions from particle theories beyond the Standard Model that suggest new particles with this interaction strength, came to be known as “WIMP MIRACLE”.

A WIMP, which stands for Weakly Interacting Massive Particle, refers to a broad class of massive dark matter candidates with roughly weak-scale interactions. A notable example of a WIMP is the lightest supersymmetric particle (LSP) [11]. WIMPs were among particle physicists’ favorite dark matter candidates for several decades, as they seemed to kill two birds with one stone: they could solve a particle-physics problem, such as the hierarchy problem, while also explaining the nature of dark matter. However, after years of both direct and indirect searches, large regions of the simplest WIMP parameter space have been ruled out, and the original optimism surrounding WIMP dark matter has significantly weakened. Perhaps nature does not like “miracles.”

WIMPs can have masses ranging from 1 GeV to 100 TeV. They can be searched for in several ways: by measuring the energy deposited when dark matter particles in our Galactic halo scatter off atomic nuclei in deep underground experiments, by producing them at particle colliders, or by detecting the radiation produced by their annihilation. Several direct-detection experiments have been built over the last three decades to search for nuclear recoils from WIMP scattering. Some notable examples are LZ [12], XENONnT [13], and PandaX [14]. Years of exposure of these direct-detection experiments to the Galactic dark matter halo have placed strong constraints on the WIMP-nucleon scattering cross-section [15], excluding large regions of the WIMP parameter space. Current searches for WIMPs are probing even smaller cross-sections. However, there is a limit to how far this strategy can be pushed. At very small cross-sections, events from coherent elastic neutrino-nucleus scattering become an important background. These backgrounds create a boundary in the cross-section versus dark matter mass plane known as the "neutrino fog," below which a dark matter discovery becomes extremely challenging.

The strong constraints on WIMP dark matter have forced theorists and phenomenologists to look beyond weakly interacting particles at the GeV–TeV scale. Recent studies focus on light, sub-GeV dark matter [16, 17], as well as ultraheavy dark matter [18] with masses above the standard thermal relic scale. The models of these particles may or may not arise from UV-complete theories, but their phenomenology can still guide searches for dark matter. Thus, the search for dark matter has shifted from the simplest WIMP models to a broader landscape of thermal and non-thermal candidates. One such highly motivated non-thermal dark matter candidate is the axion.

1.4 Axion and Axion-Like Particles

Originally proposed to explain the absence of observed CP violation in Quantum Chromodynamics (QCD), the axion is a generic pseudo-Nambu-Goldstone boson associated with global $U(1)$ symmetry breaking [19, 20]. Experimental measurements of the electric dipole moment of a neutron place very strong constraints on CP-violating terms in the QCD lagrangian, requiring the angular parameter $\bar{\theta}$ that serves as the measure of CP violation to satisfy $\bar{\theta} \lesssim 10^{-10}$. The smallness of this parameter, commonly known as the "strong CP problem" can be naturally explained by introducing an additional global $U(1)$ symmetry, known as the Peccei–Quinn symmetry, which is spontaneously broken at an energy scale f_{a}. The resulting Nambu–Goldstone boson, also known

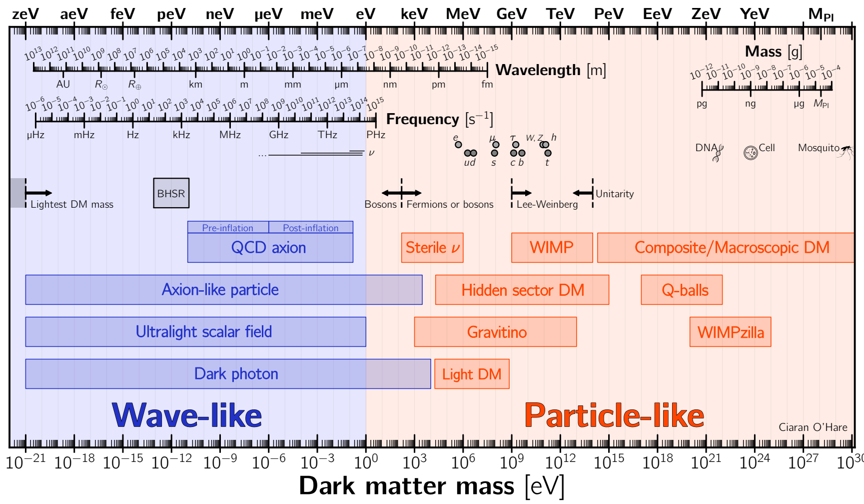

Figure 1.1: Theoretically well-motivated dark matter candidates [21].

as the QCD axion, acquires a mass through non-perturbative effects that is inversely proportional to the decay constant $f_{\rm a}$. Although the QCD axion is very light (since $f_{\rm a}$ is rather large), it can be produced in large enough abundance in the early Universe to act as dark matter, making it one of the leading dark matter candidates.

Axion-like particles (ALPs) are ubiquitous in physics beyond the Standard Model and String Theory [22]. Unlike the QCD axion, ALPs do not necessarily solve the strong CP problem, and their masses and couplings are largely independent parameters. ALPs can therefore span a very broad range of masses, ranging from a few μeV to several keV, depending on the model. A common property shared by all ALPs is their coupling to photons, which serves as the motivation for experimental and observational searches. The ALP-photon coupling $g_{\rm a\gamma\gamma}$ is strongly model dependent and is therefore taken as a free parameter to avoid invoking the details of the UV completeness of the theory. Because of this coupling, ALPs can convert into photons and vice versa in the presence of a magnetic field, resulting in a wide variety of observable phenomena [23, 24].

The abundance of axion dark matter on small scales depends sensitively on whether the Peccei–Quinn symmetry is broken before or after inflation. In the latter case, known as the "post-inflationary Peccei–Quinn symmetry breaking scenario," the axion field can naturally contain substantial density fluctuations. These fluctuations can lead to the formation of compact dark matter structures, often called axion miniclusters or minihalos. The existence of these structures can introduce significant theoretical uncertainty in the local axion density relevant for laboratory-based axion dark matter detection. We will discuss the search for these minihalos in more detail in Chapter 2.

1.5 Current Status and Future Directions

"Ever tried. Ever failed. No matter. Try again. Fail again. Fail better."

– Samuel Beckett, *Worstward Ho*

Consistent with current astrophysical and cosmological observations, dark matter can, in principle, span an enormous range of masses: from ultralight particles with masses as small as $10^{-20}\,\mathrm{eV}$ to compact objects with masses many times larger than the mass of the Sun. Its interaction strength with the Standard Model can also vary widely, from weak-scale interactions to purely gravitational interactions. Thus, the search for dark matter today involves probing a vast parameter space, as shown in Fig. 1.1, large regions of which remain unexplored. While this task may seem daunting, science often resembles the art of searching for a needle in a haystack, because that needle is precisely what matters.

To scan the full space of viable dark matter candidates, we need a wide range of experimental and observational techniques. In this thesis, I will present some astrophysical and cosmological methods to probe dark sector physics [25, 26, 27, 28, 29]. I have attempted to cover a broad range of dark matter masses, from axion-like particles to sub-GeV dark matter to primordial black holes. At the time of writing this thesis, dark matter remains one of the key drivers across many experimental and observational frontiers. While a direct detection signal would provide one of the cleanest paths toward discovery, indirect signatures from astrophysics and cosmology can also help uncover its mystery, one layer at a time.

Chapter 2

Dynamical Heating from Dark Compact Objects and Axion Minihalos: Implications for the 21-cm Signal

Massive Compact Halo Objects (MACHOs) are a class of dark matter (DM) candidates that lie beyond the conventional particle DM paradigm. Proposed examples include primordial black holes (PBHs) [30, 10], axion stars [31, 32, 33], and compact objects formed through dynamics in the dark sector [34, 35, 36, 37]. Many searches for these objects target unique signatures, such as explosive events from axion stars [38, 39, 40]. For PBHs, heating due to the accretion of material around these objects can impact the cosmic microwave background (CMB) [41, 42] and the properties of dwarf galaxies [43, 44, 45]. Such PBH bounds are, however, not applicable to MACHOs that are less dense, which may not accrete efficiently.

More generic MACHO constraints come from gravitational microlensing and dynamical heating. Data from the MACHO [46], EROS-2 [47], and OGLE-IV [48] microlensing surveys have ruled out MACHOs in the $\lesssim \mathcal{O}(10)\, M_\odot$ mass range as the primary component of DM [49]. Meanwhile, higher masses $\gtrsim \mathcal{O}(10)\, M_\odot$ are constrained by the non-observation of dynamical heating of gas and stars in dwarf galaxies [50, 43, 51, 44, 52, 53, 54, 45]. While microlensing and dynamical heating in small-scale structures offer powerful constraints, each is subject to distinct sources of uncertainty, making complementary approaches valuable.

In this *work*, I propose a novel probe of MACHO abundances based on dynamical friction (DF) heating of the baryon fluid in the early universe. As a MACHO moves through baryons, it generates an enhanced-density wake, and the gravitational interaction between the MACHO and its wake gives rise to a drag force. The resulting momentum loss transfers energy to the baryon fluid, heating it. Because this fluid is collisional, the effect is strongly suppressed at early times while the bulk relative velocity $v_{\rm rel}$ is smaller than the photon-baryon sound speed c_s ($\mathcal{M} \equiv v_{\rm rel}/c_s \ll 1$) [55]. Following baryon decoupling and the sharp drop in c_s at recombination, however, typical velocities of $v_{\rm rel} \sim 30\,{\rm km\,s^{-1}}$ [56] correspond to $\mathcal{M} \sim 5$ in the baryon fluid, and so DF becomes efficient.

The resulting increase in the baryon temperature $T_{\rm B}$ could be detectable with 21-cm cosmology. The heating or cooling of baryons due to momentum transfer between the dark sector and baryons during the cosmic dark ages—and its consequences for the 21-cm global signal and power spectrum—has been extensively studied [57, 58, 59, 60, 61, 62, 63, 64, 65]. We therefore expect 21-cm observations to be similarly sensitive to DF heating. Compared to the phenomenology of DM-baryon scattering, however, DF heating is remarkable for at least three reasons. First, the suppression of DF at small $\mathcal{M}$ means that DF is effectively negligible prior to recombination, leading to virtually no impact on the CMB, Lyman-α forest, or small-scale structure. This contrasts sharply with DM-baryon scattering, which affects the evolution of perturbations on scales that enter the horizon before recombination (see *e.g.* Refs. [66, 67, 68, 69, 70, 71, 72]). Second, energy injection from DM-baryon scattering, as well as from DM annihilation and decay, is deposited into several different channels, including ionization, excitation, and heating. Such deposition can then modify both the ionization history and thermal history of the universe.

In contrast, here, all of the deposited energy goes directly into heating. Third, the strong correlation between DF and $v_{\rm rel}$ leads to an *enhancement* in the fluctuations of $T_{\rm B}$, and therefore in the 21-cm power spectrum, relative to ΛCDM expectations.

The dependence of $T_{\rm B}$ on $v_{\rm rel}$ also imprints an enhanced baryon acoustic oscillation (BAO) feature onto the power spectrum relative to ΛCDM [73, 74, 75]. This enhancement is also predicted in models with a millicharged DM subcomponent that can transfer heat between baryons and the dark sector [65], except that here the baryons are heated rather than cooled. The enhancement stands in contrast to the suppression of the power spectrum generically expected from DM annihilation and decay [76, 77, 78, 79, 80], or from PBH accretion [81], where energy injection leads to a more homogeneous 21-cm signal.

These striking signatures of DF heating by MACHOs make it an excellent new-physics target for near-future measurements of the 21-cm global signal [82, 83, 84] and the power spectrum [85, 86, 87]. In this work, we focus on two well-motivated scenarios: 1) MACHOs of a characteristic mass in the $10^2\,\mathrm{M}_\odot$ to $10^5\,\mathrm{M}_\odot$ range comprising some fraction $f_{\rm M}$ of the DM, and 2) axion (or more generally, axion-like particle (ALP)) minihalos. We estimate that both global signal and power spectrum measurements will be sensitive to $f_{\rm M} \sim 0.1$ for MACHOs in the mass range $10^4\,\mathrm{M}_\odot$ to $10^5\,\mathrm{M}_\odot$, and will significantly improve sensitivity to the ALP symmetry breaking scale f_a for ALP masses m_a in the range $10^{-18}\,\mathrm{eV}$ to $10^{-9}\,\mathrm{eV}$. In combination with limits from the apparent absence of black hole superradiance [88, 89, 90, 91, 92], these measurements could potentially rule out ALPs with $m_a \sim 10^{-12}\,\mathrm{eV}$ for any value of f_a.

The DF heating signal depends primarily on the perturber mass and on the well-understood distribution of bulk relative velocities between DM and baryons from linear cosmology. Our estimates are therefore relatively free from the uncertainties that affect other probes like microlensing and UFD heating, such as assumptions about MACHO survivability or accretion, the spatial distribution of MACHOs in galaxies, and baryonic physics. While DF heating has its own uncertainties, which will likely require simulations to determine precisely, our work strongly suggests that 21-cm measurements can achieve unprecedented sensitivity to MACHOs and axion minihalos, and strong complementarity to other constraints in regimes where it is expected to be less competitive.

2.1 Dynamical Friction Heating

For a sufficiently massive DM component streaming through the baryonic fluid, energy exchange will occur through purely gravitational interactions. In particular, the gravitational attraction between the perturber and its enhanced-density wake results in a drag force known as dynamical friction (DF). The energy lost by the perturber in this manner goes into heating the baryonic fluid.

Refs. [93, 94, 55] studied DF in a collisional medium, deriving the magnitude of the drag force on a perturber of mass M in the linear regime–where density perturbations due to the perturber are small–as

$$F_{\rm DF}(M, v_{\rm rel}) = \frac{4\pi G^2 M^2 \rho_{\rm B}}{v_{\rm rel}^2}\, \mathcal{I}(\mathcal{M}, \Lambda)\,, \tag{2.1}$$

with $\rho_{\rm B}$ the cosmological mean density of baryons, the medium of interest to us. The relative velocity between baryons and DM arises from the different evolution of their velocity fields. Before recombination, baryons were tightly coupled to photons, unlike DM, leading to a coherent bulk motion between the two fluids. At recombination, this relative velocity has an rms value of $30\,{\rm km\,s^{-1}}$, which is independent of the formation mechanism of the massive DM components. The function $\mathcal{I}(\mathcal{M},\Lambda)$ depends on the Mach number $\mathcal{M}$ and on the Coulomb logarithm $\ln\Lambda \equiv \ln(b_{\rm max}/b_{\rm min})$, which serves to regulate an integral over impact parameters. The minimum and maximum values $b_{\rm min}$ and $b_{\rm max}$ can be taken to be the smallest and largest length scales for which the approximations used (point-like perturber, coherent medium response, *etc.*) remain valid. An expression for $\mathcal{I}(\mathcal{M},\Lambda)$ valid for all values of $\mathcal{M}$ is provided in Appendix A. Here we simply note that it is maximized for $\mathcal{M}\sim 1$, and has the asymptotic limiting behavior

$$\mathcal{I}(\mathcal{M},\Lambda) \approx \begin{cases} \mathcal{M}^3/3\,, & \mathcal{M} \ll 1\,, \\ \\ \ln\Lambda\,, & \mathcal{M} \gg 1\,. \end{cases} \tag{2.2}$$

In the subsonic $\mathcal{M} \ll 1$ regime, applicable before recombination when $c_s \sim 1/\sqrt{3}$ and the typical baryon-DM bulk relative velocity is $\sim 10^{-5}$ [66], we see that $F_{\rm DF}$ is extremely suppressed and therefore negligible. Physically, the large sound speed results in an almost front-back symmetric density distribution of baryons about the perturber. Following recombination, however, the baryon sound speed drops to $c_s \sim \sqrt{T_{\rm B}/m_{\rm p}} \sim 10\,{\rm km\,s^{-1}}$. Since typical bulk relative velocities at this time are $v_{\rm rel} \sim 30\,{\rm km\,s^{-1}}$ [56], this corresponds to the regime $\mathcal{M} \gtrsim 1$, for which DF becomes relevant. Physically, the supersonic regime is characterized by an enhanced-density region confined to a Mach cone behind the perturber with a half-opening angle $\sin\theta = 1/\mathcal{M}$. Larger $\mathcal{M}$ then corresponds to a narrower Mach cone and a more geometrically asymmetric wake.

In this regime, the value of Λ, set by a choice of $b_{\rm min}$ and $b_{\rm max}$, is important for determining the DF force. We take $b_{\rm max} = \mathcal{M}\lambda_{\rm J}$, where $\lambda_{\rm J} = \sqrt{\pi c_s^2/G\rho_{\rm B}} \sim c_s H^{-1}$ is the Jeans length, with H the Hubble parameter. This is roughly the distance traveled by the perturber over the age of the Universe, a reasonable estimate for the transverse size of the Mach cone and the effective size of the surrounding gaseous medium, and is consistent with Refs. [95, 96]. For $b_{\rm min}$, we take the Bondi-Hoyle-Lyttleton radius for MACHOs, $b_{\rm min} = GM/(c_s^2 + v_{\rm rel}^2)$, based on the conclusion drawn by Ref. [97] that there is no DF from gas within this radius. This is therefore a good choice for MACHOs that have a smaller spatial extent than the Bondi-Hoyle-Lyttleton radius. For axion minihalos, we adopt $b_{\rm min} = 0.35\mathcal{M}^{0.6} r_{\rm vir}$, where $r_{\rm vir}$ is the virial radius of the halo, consistent with the choice made in the simulations of Refs. [98, 95, 96] to match the linear results of Refs. [93, 94, 55].

The DF heating rate per baryon $\dot{Q}_{\rm DF}$ is [99, 100]

$$\dot{Q}_{\rm DF}(v_{\rm rel}, z) = \frac{1}{n_{\rm B}} \int {\rm d}M \frac{\rho_{\rm DM}}{M} \frac{{\rm d}f}{{\rm d}M} v_{\rm rel} F_{\rm DF} \,, \tag{2.3}$$

where $v_{\rm rel} F_{\rm DF}$ is the perturber's rate of kinetic energy loss, $\rho_{\rm DM}$ is the DM energy density, and ${\rm d}f/{\rm d}M$ is the fraction of DM (by mass) in perturbers of mass M. The resulting change in baryon temperature can be estimated by numerically solving the following equations:

$$\frac{\mathrm{d}v_{\mathrm{rel}}}{\mathrm{d}\ln a} = -v_{\mathrm{rel}} - \frac{F_{\mathrm{DF}}}{MH}\,, \tag{2.4}$$

$$\frac{\mathrm{d}T_{\mathrm{B}}}{\mathrm{d}\ln a} = -2T_{\mathrm{B}} + \frac{\Gamma_C}{H}(T_{\mathrm{CMB}} - T_{\mathrm{B}}) + \frac{2}{3}\frac{\dot{Q}_{\mathrm{DF}}}{H}\,, \tag{2.5}$$

where T_{CMB} is the CMB radiation temperature and Γ_C is a rate governing Compton scattering. We also simultaneously evolve the free electron fraction using the three-level atom model [101, 102]; more details can be found in Ref. [103]. The terms in Eq. (2.5) correspond only to adiabatic cooling, heating through Compton scattering with the CMB, and DF heating, respectively. In this work, we only consider the 21-cm signal for $z \geq 17$, and assume no significant X-ray heating has occurred until this point, which is a reasonable scenario given current astrophysical constraints (see *e.g.* Ref. [104]). We also neglect other irreducible sources of heating, including Lyman-α recoils [105, 106, 107, 108], since these are subdominant to the $\mathcal{O}(1)$ heating contribution from DF we will be sensitive to.

These equations are integrated from recombination at $z = 1100$, starting from an initial bulk relative velocity $\vec{v}^*_{\mathrm{rel}}$, down to $z = 17$. Since the DF effect is negligible prior to recombination, the velocity distribution at recombination is Gaussian, as predicted by ΛCDM, *i.e.*

$$f(\vec{v}^*_{\mathrm{rel}}) = \left(\frac{3}{2\pi v_{\mathrm{rms}}^2}\right)^{3/2} \exp\left(-\frac{3v^{*2}_{\mathrm{rel}}}{2v_{\mathrm{rms}}^2}\right)\,, \tag{2.6}$$

where we set $v_{\mathrm{rms}} = 29\,\mathrm{km\,s^{-1}}$ [56]. We thereby obtain $T_{\mathrm{B}}(v^*_{\mathrm{rel}}, z)$ for $0 \leq v^*_{\mathrm{rel}} \leq 100\,\mathrm{km\,s^{-1}}$, which encompasses most of the range relevant for an accurate 21-cm determination. Note that under our approximations, T_B depends only on v_rel^* and z; properly capturing other effects would require simulations, which we leave to future work.

Although the preceding results were derived assuming that all density perturbations are small, for $\mathcal{M} \gtrsim 1$, this is not a self-consistent assumption; in fact, near the edges of the Mach cone, the fluid overdensity becomes large, approaching infinity for a point-like perturber. Despite this inconsistency, Ref. [98] showed that there is a tight correlation between the DF force estimated in simulations and F_DF calculated in the linear regime using Eq. (2.1), finding a large, order of magnitude difference only for very massive halos, extremely small perturbers, or when $\mathcal{M}$ is very close to 1. We find that this discrepancy should not affect our MACHO analysis significantly, but could lead to an $\mathcal{O}(1)$ overestimate of the DF force for heavy axion minihalos in a limited redshift window; see Appendix A for further details.

2.2 MACHOs & Axion Minihalos

We model dark compact object DF heating in two scenarios. First, we adopt a phenomenological approach and simply assume a population of MACHOs with a single characteristic mass M making up a fraction f_M of the DM energy density, *i.e.* $df/dM' = f_\mathrm{M}\delta(M' - M)$. Second, we consider DF heating from axion minihalos; this scenario has a complicated perturber mass function that evolves with redshift, depending on the ALP parameters m_a and f_a.

Axion minihalos (or miniclusters) will form as early as matter-radiation equality due

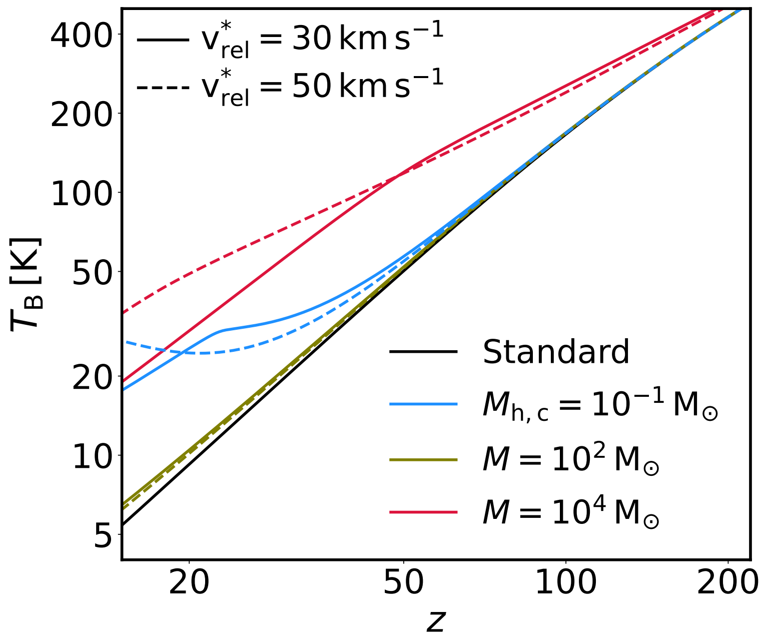

Figure 2.1: Baryon temperature $T_{\rm B}$ as a function of redshift for MACHOs of mass $M = 10^2\,{\rm M}_\odot$ (olive) and $M = 10^4\,{\rm M}_\odot$ (red), and for axion minihalos with an initial mass $M_{\rm h,c} = 10^{-1}\,{\rm M}_\odot$ (blue), assuming MACHOs/axions constitute 100% of the DM. The solid (dashed) lines correspond to a DM-baryon relative velocity at recombination of $v^*_{\rm rel} = 30\,(50){\rm km\,s^{-1}}$.

to the enhanced small-scale fluctuations which are produced by the randomized axion field across different horizons in the post-inflationary scenario [109, 110, 111]. Even in scenarios with pre-inflationary Peccei-Quinn breaking, many production mechanisms can lead to the formation of these dense axion substructures [112, 113, 114, 115, 116, 117]. The initial axion minihalo mass is determined by the DM mass contained within the horizon at the axion oscillation time, when axions start to behave as nonrelativistic matter. Since the initial axion density is $\sim m_a^2 f_a^2$, the oscillation time can be uniquely determined from the relic abundance and axion parameters. Therefore, the initial axion

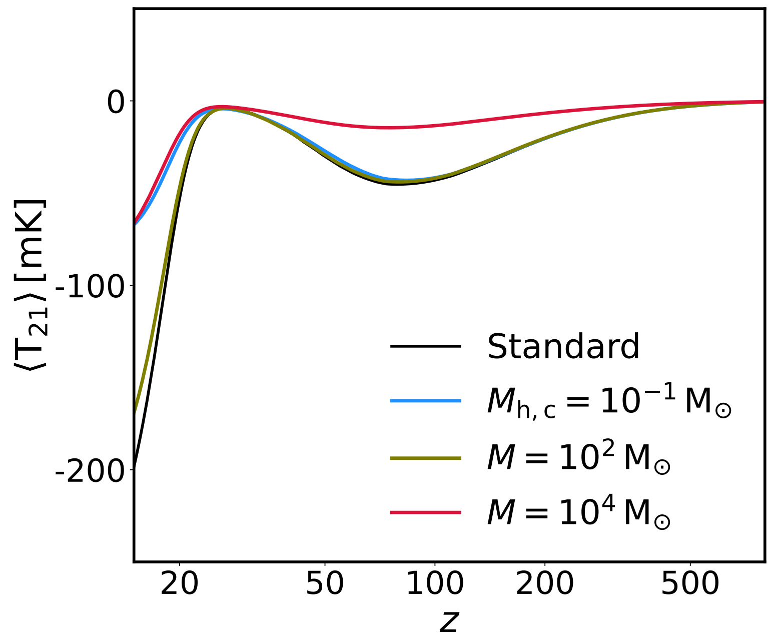

Figure 2.2: The sky-averaged 21-cm brightness temperature $\langle T_{21}\rangle(z)$ for MACHOs of mass $M = 10^2\,\mathrm{M}_\odot$ (olive) and $M = 10^4\,\mathrm{M}_\odot$ (red), and for axion minihalos with an initial mass $M_{\rm h,c} = 10^{-1}\,\mathrm{M}_\odot$ (blue), assuming MACHOs/axions constitute 100% of the DM.

minihalo mass is [40]

$$M_{\rm h,c} \approx 1.5 \times 10^{-11}\,\mathrm{M}_\odot \left(\frac{m_a}{10^{-6}\,\mathrm{eV}}\right)^{-2} \left(\frac{f_a}{10^{11}\,\mathrm{GeV}}\right)^{-2} g_{*,\rm osc}^{-1/2}, \tag{2.7}$$

where $g_{*,\rm osc}$ is the degrees of freedom at the onset of oscillation. Although the value of $g_{*,\rm osc}$ depends on m_a and f_a, we conservatively take it to be 10, which is also consistent with the relevant axion parameters where the bound is the strongest. To model the axion minihalo mass function, we use a semi-analytic Press-Schechter model [118], $\mathrm{d}f_{\rm h}/\mathrm{d}\ln M_{\rm h} = \sqrt{\nu/(2\pi)}e^{-\nu/2}\,\mathrm{d}\ln\nu/\mathrm{d}\ln M_{\rm h}$, where $f_{\rm h}$ is the fraction of DM bound in minihalos, $M_{\rm h}$ is the minihalo mass, $\nu \equiv \delta_c^2/[\sigma^2(M_{\rm h})D^2(z)]$, $\delta_c = 1.68$ and $D(z)$ is the growth function.

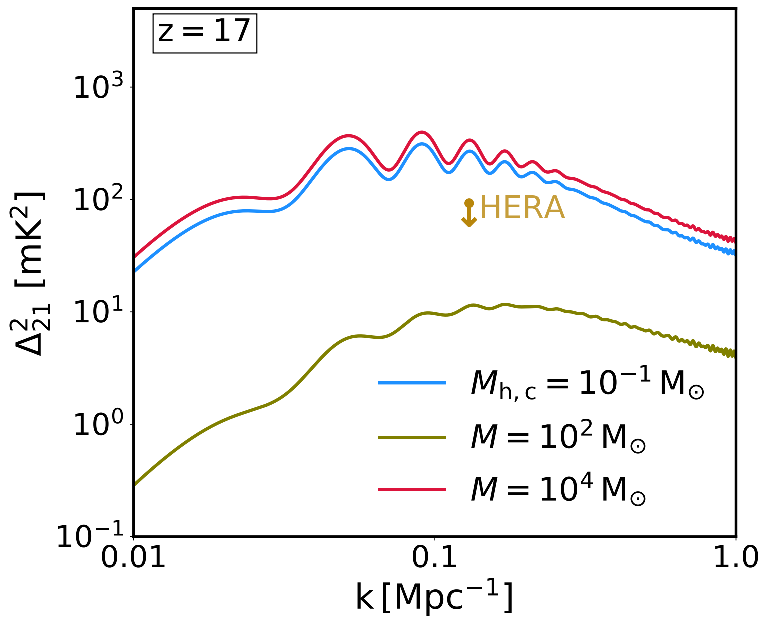

Figure 2.3: The 21-cm power spectrum Δ^2_{21} as a function of comoving wavenumber at $z = 17$ for MACHOs of mass $M = 10^2\,\mathrm{M}_\odot$ (olive) and $M = 10^4\,\mathrm{M}_\odot$ (red), and for axion minihalos with an initial mass $M_{\rm h,c} = 10^{-1}\,\mathrm{M}_\odot$ (blue), assuming MACHOs/axions constitute 100% of the DM. The golden arrow indicates the expected HERA sensitivity of $92.7\,\mathrm{mK}^2$ after 10^3 hours of integration time, following Refs. [63, 65].

This mass function agrees reasonably well with other analytic and numerical studies on the axion minihalo mass function [119, 120, 121, 122]. Since fluctuations on small scales are dominated by the order-unity axion perturbations, one can consider the axion-induced power spectrum independently from the adiabatic fluctuations. In the post-inflationary scenario, a totally randomized axion field is converted to DM inhomogeneities. Therefore, it is well described by a white-noise spectrum, with the characteristic scale determined by the horizon size at the oscillation time. Given the spectrum, the variance entering in the minihalo mass function is computed as $\sigma(M_{\rm h}) \approx \sqrt{3\pi M_{\rm h,c}/(2M_{\rm h})}$.

The white-noise power spectrum accurately characterizes the initial minihalo formation and evolution until massive cold dark matter (CDM) halos form from the adiabatic fluctuations around $z \sim 20$. After that, some fraction of the axion minihalos will be subsumed into the massive CDM halos, effectively freezing their population. The final axion minihalo mass function, including the infall minihalos, is heuristically [122]

$$\frac{\mathrm{d}f}{\mathrm{d}M_\mathrm{h}}(z) = \int_{z_\mathrm{eq}}^{z} \mathrm{d}z' \frac{\mathrm{d}f_\mathrm{col}^\mathrm{CDM}}{\mathrm{d}z'} \frac{\mathrm{d}f_\mathrm{h}}{\mathrm{d}M_\mathrm{h}}(z') + [1 - f_\mathrm{col}^\mathrm{CDM}(z)] \frac{\mathrm{d}f_\mathrm{h}}{\mathrm{d}M_\mathrm{h}}(z) \,, \tag{2.8}$$

where $f_\mathrm{col}^\mathrm{CDM}(z)$ is the collapse fraction of massive CDM halos predicted by the adiabatic fluctuations,

$$f_\mathrm{col}^\mathrm{CDM}(z) = \mathrm{erfc}\left(\frac{\delta_\mathrm{c}}{\sqrt{2}\, \sigma_\mathrm{CDM}(M_\mathrm{cut})\, D(z)} \right) \,, \tag{2.9}$$

where $\sigma^2_\mathrm{CDM}(M)$ is the variance of adiabatic fluctuations and M_cut is the minimal mass of CDM halos that can absorb axion minihalos in the parameter space of relevance. We take $M_\mathrm{cut} = 10^6 M_\odot$ so that the CDM halos are always larger than the axion minihalo for the infall process to be valid, for which $\sigma_\mathrm{CDM}(M_\mathrm{cut}) = 8.2$ [123]. Note that the collapse fraction depends nearly logarithmically on the choice of M_cut due to the power spectrum of adiabatic fluctuations. The collapse fraction of massive CDM halos is only $\sim 1\%$ at $z \sim 17$. Therefore, the majority of axion minihalos remain isolated, and the contribution from CDM halos will be subdominant, which is consistent with previous studies on the dynamical heating from CDM halos [96, 95].

The DF heating rate due to axion minihalos can be evaluated by substituting Eq. (2.8) into Eq. (2.3). We take the lower limit of integration to be $M_\mathrm{h,c}$ and the upper limit to be $M_\mathrm{max} = 10^6\, M_\odot$, which is less than M_cut, and simultaneously avoids the region of parameter space where the linear approximation is poor (see Appendix A for more details). In any case, halos with such a large mass deposit most of their energy through DF while baryons are still tightly coupled to the CMB, leading to insignificant heating.

In Fig. 2.1, we show the evolution of $T_{\rm B}$ as a function of z and $v^*_{\rm rel}$. The DF heating is most noticeable at low redshifts, once the baryons have thermally decoupled from the CMB. The heating rate increases with the perturber mass, but decreases with an increase in relative velocity, which is consistent with the drag force scaling as $F_{\rm DF} \propto M^2 \ln(v^2_{\rm rel})/v^2_{\rm rel}$. Note that baryon heating is only efficient after thermal decoupling from the CMB at $z \sim 150$. As such, for sufficiently small values of $v^*_{\rm rel}$, the perturber could become subsonic before decoupling, leading to reduced heating, especially for larger perturbers. Conversely, for sufficiently large $v^*_{\rm rel}$, DF-induced heating is suppressed at high redshifts, but becomes significant at low redshifts, after the relative velocity has decreased somewhat.

2.3 21-cm Signal

The absorption or emission of 21-cm blackbody CMB photons via the hyperfine transition of neutral hydrogen atoms at redshift z leads to a spectral distortion of the CMB at wavelength $21\,\mathrm{cm} \times (1+z)$, typically reported as a differential brightness temperature relative to the CMB along some line-of-sight $\hat{n}$ and redshift z, $T_{21}(\hat{n}, z)$. The size of this distortion depends on the relative occupation number of the two-level hyperfine system, parametrized by a single temperature $T_{\rm s}$, the spin temperature, which is strongly dependent on the baryon temperature $T_{\rm B}$. Detecting the 21-cm signal would therefore provide us with a relatively direct probe of $T_{\rm B}$ during the cosmic dark ages, allowing us

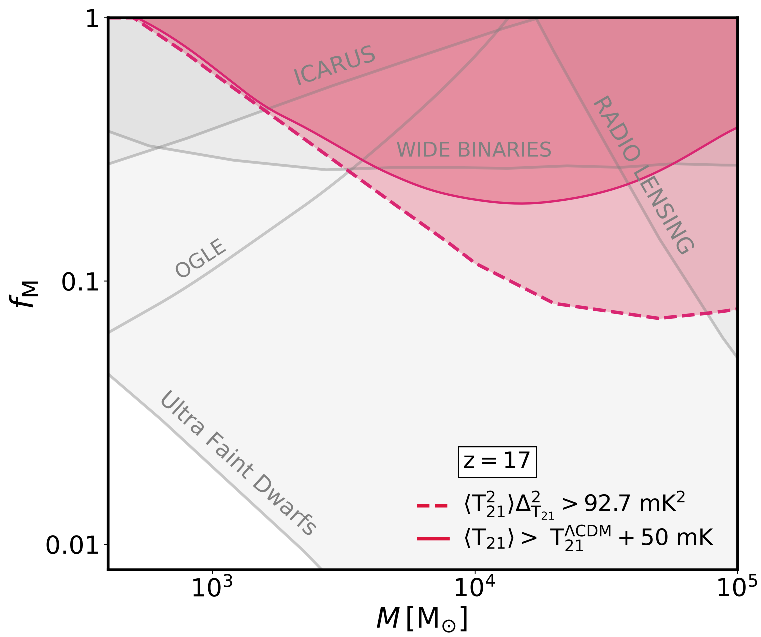

Figure 2.4: Forecasted sensitivity (in red) of the 21-cm signal to the MACHO fraction as a function of MACHO mass. The solid curve marks the region in which DF heating yields a brightness temperature that is 50 mK higher than expected in ΛCDM, while the dashed line corresponds to the forecasted sensitivity from HERA. The other limits come from the observed half-light radius of Ultrafaint dwarf galaxies (UFDs) [52], the existence of wide binaries [124], non-detection of lensing effects of compact radio sources [125], and the caustic crossing of Icarus [126]. See also Refs. [51, 45] for bounds under different assumptions of the MACHO density profile.

to look for anomalous heating due to DF of compact objects. There are two main experimental modes for detecting this signal: the sky-averaged or global signal integrated over solid angle $\langle T_{21}\rangle(z)$, or a measurement of the power spectrum of fluctuations $\Delta^2_{21}(k, z)$, where k is the comoving wavenumber.

The brightness temperature is given by

$$T_{21} = \frac{1}{1+z}(T_\mathrm{s} - T_\mathrm{CMB})(1 - e^{-\tau})\,, \tag{2.10}$$

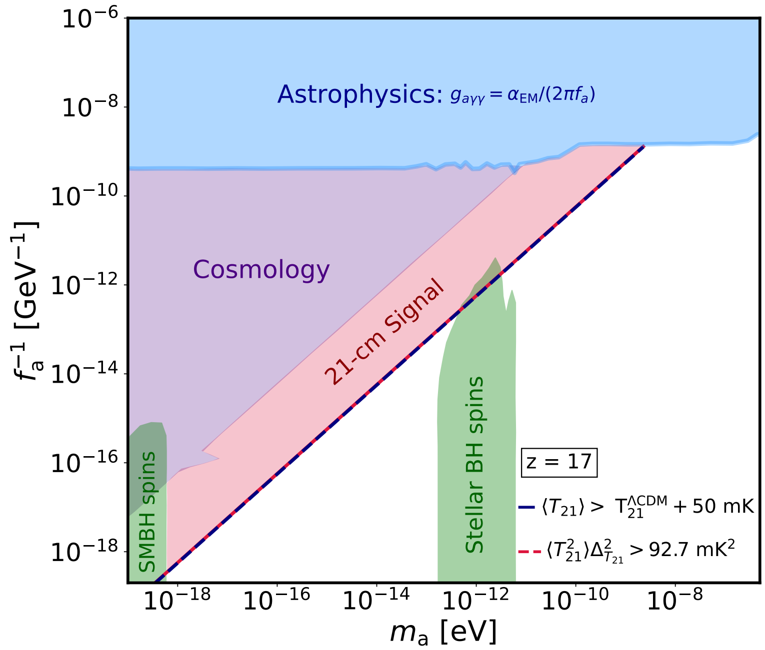

Figure 2.5: Forecasted sensitivity (in red) of the 21-cm signal to ALP symmetry breaking scale f_a for ALP masses m_a. The solid and dashed curves correspond to an axion minihalo with an initial mass of $M_{\rm h,c} = 0.015\,{\rm M}_\odot$. Also shown are bounds derived from astrophysical probes of the axion-photon coupling assuming $g_{a\gamma\gamma} = \alpha_{\rm EM}/(2\pi f_a)$ [127, 128, 129, 130, 131, 132], cosmology (in purple) [133, 134], and the superradiance bounds (in green) taken from Refs. [88, 89, 90, 91, 92], as compiled in Ref. [135].

where τ is the optical depth for resonant 21-cm absorption [136].

The spin temperature is determined by the interactions between the two-level system and CMB photons, other hydrogen atoms, and Lyman-α radiation, according to [136]

$$T_{\rm s}^{-1} = \frac{T_{\rm CMB}^{-1} + x_\alpha T_\alpha^{-1} + x_c T_{\rm B}^{-1}}{1 + x_\alpha + x_c}\,, \tag{2.11}$$

where T_α is the color temperature of the Lyα radiation field, and x_α, x_c are the Lyα and collisional coupling coefficients, respectively. In our analysis, we set $T_\alpha = T_{\rm B}$ which is an excellent approximation for $T_{\rm B} \gtrsim 1\,{\rm K}$ [136], and use the default values of $x_\alpha(z)$

used in `Zeus21` [137]; see Ref. [65] for details of how $x_c(z)$ is computed, based on results in Refs. [138, 139, 140].

We estimate the global signal and power spectrum at $z = 17$ in order to determine the sensitivity to DF heating by compact objects, using $T_{\mathrm{B}}(v^*_{\mathrm{rel}}, z)$ determined from integrating Eq. (2.5) to obtain $T_{21}(v^*_{\mathrm{rel}}, z)$. The sky-averaged brightness temperature is then given by

$$\langle T_{21}\rangle(z) = \int \mathrm{d}^3\vec{v}^*_{\mathrm{rel}}\, f(\vec{v}^*_{\mathrm{rel}}) T_{21}(v^*_{\mathrm{rel}}, z)\,, \tag{2.12}$$

where $f(\vec{v}^*_{\mathrm{rel}})$ is given in Eq. (2.6).

For the power spectrum, we define the 21-cm brightness temperature fluctuation as $\delta_{T_{21}}(\vec{x}, z) \equiv T_{21}(\vec{x})/\langle T_{21}\rangle(z) - 1$. Assuming homogeneity and isotropy, the two-point correlation function (2PCF) reads $\xi(r) \equiv \langle \delta_{T_{21}}(\vec{x}_1)\delta_{T_{21}}(\vec{x}_2)\rangle_r$, where $\langle\cdots\rangle_r$ denotes an average over all pairs of points such that $|\vec{x}_1 - \vec{x}_2| = r$. The 21-cm power spectrum is then obtained via Fourier transform,

$$\Delta^2_{21}(k, z) = \frac{2k^3}{\pi}\langle T_{21}\rangle^2(z)\int_0^\infty \mathrm{d}r\, r^2 \xi(r)\frac{\sin(kr)}{kr}\,. \tag{2.13}$$

$\xi(r)$ is determined by averaging over the joint Gaussian distribution of the relative velocities at separated points,

$$\xi(\vec{r}) = \int \mathrm{d}^3\vec{v}^*_{\mathrm{rel},a}\int \mathrm{d}^3\vec{v}^*_{\mathrm{rel},b}\ \mathcal{P}(\vec{v}^*_{\mathrm{rel},a}, \vec{v}^*_{\mathrm{rel},b}; \vec{r}) \times \delta_{T_{21}}(\vec{v}^*_{\mathrm{rel},a})\delta_{T_{21}}(\vec{v}^*_{\mathrm{rel},b})\,, \tag{2.14}$$

where the exact structure of $\mathcal{P}$ follows from linear theory [73, 74, 65].

The Fig. 2.2 shows the global signal, including only DF heating for both cases considered here. DF heating suppresses the global signal, since $T_{\rm B}$ is brought closer to $T_{\rm CMB}$, leading to less net absorption. Note that although the signals for MACHOs with mass $M = 10^4\,{\rm M}_\odot$ and axion minihalos with $M_{h,c} = 10^{-1}\,{\rm M}_\odot$ are similar at $z \lesssim 30$, they differ significantly at $z \sim 100$, since the masses of axion minihalos grow with time, leading to much less heating at early times. The corresponding power spectrum is shown in Fig. 2.3. We also show an approximate forecast of the sensitivity of HERA to the power spectrum after 10^3 hours of integration time, *i.e.* $\Delta_{21}^2 = 92.7\,{\rm mK}^2$ for $k = 0.13\,{\rm Mpc}^{-1}$ at $z = 17$ [63, 65]. This is comparable to the largest magnitude of the power spectrum anticipated in ΛCDM astrophysical models [104]. In the representative cases considered here, the DF signal can significantly exceed this.

The strong dependence of DF heating on the bulk relative velocity has two effects on Δ_{21}^2. First, it enhances fluctuations in T_{21} significantly, leading to a larger overall amplitude in Δ_{21}^2. Second, the baryon acoustic oscillation feature in the bulk relative velocity power spectrum gets imprinted onto Δ_{21}^2. The signature is striking; for sufficiently large DF heating, Δ_{21}^2 would be larger than ΛCDM expectations, making 21-cm fluctuations easier to detect.

2.4 Results

We estimate the sensitivity of the global signal by requiring that DF heating increases $\langle T_{21} \rangle$ by $50\,{\rm mK}$ relative to the ΛCDM expectation at $z = 17$. For the power spectrum, we instead require that Δ_{21}^2 at $k = 0.13\,{\rm Mpc}^{-1}$ and $z = 17$ exceed the HERA forecasted sensitivity discussed above. The corresponding projected sensitivities are depicted as solid and dashed lines, respectively, in Fig. 2.4. We find that the 21-cm signal can be sensitive to MACHOs comprising 10% of the DM in the mass range $10^4\,\mathrm{M}_\odot$ to $10^5\,\mathrm{M}_\odot$. This improves on searches using wide-binaries [124], lensing of compact radio sources [125], and the disruption of caustics [126], but is still outperformed by dynamical heating of stars in UFDs [50, 52].

For axion minihalos, the mass function and the behavior of such objects within other systems complicate the ability of lensing or dynamical heating to constrain them. The relatively homogeneous conditions of the early Universe, however, means that we have no such concerns. We find that the smallest initial halo mass $M_{h,c}$ to which the 21-cm signal is sensitive to is $0.015\,\mathrm{M}_\odot$, which grows to $\mathcal{O}(10^3)\,\mathrm{M}_\odot$ by $z = 17$. The corresponding sensitivity to f_a as a function of m_a is shown by the solid red curve in Fig. 2.5, extending into new parameter space for $10^{-18}\,\mathrm{eV} \lesssim m_a \lesssim 10^{-9}\,\mathrm{eV}$. Together with bounds on the axion–photon coupling in astrophysical environments [127, 128, 129, 130, 131, 132, 38, 135], cosmological constraints from the Lyman-alpha forest [134] and free-streaming effects [133], as well as bounds from the absence of black hole superradiance [92], the 21-cm signal can completely rule out ALPs with a mass $m_a \sim 10^{-12}\,\mathrm{eV}$. Note that the limits on f_a derived from the axion-photon coupling $g_{a\gamma\gamma}$ assume the standard proportionality factor of $g_{a\gamma\gamma} = \alpha_{\mathrm{EM}}/(2\pi f_a)$, while all other probes considered here are directly sensitive to f_a.

Although we have only discussed the 21-cm signal just before the onset of cosmic dawn at $z \sim 17$, DF heating from dark substructures will also lead to a 21-cm signal deep in the cosmic dark ages ($z \sim 80$), and provides a strongly motivated new-physics benchmark for plans to build radio telescopes on the far side of the moon [141, 142].

The estimates here entirely rely on analytical results–backed by numerical simulations–of a single perturber at constant Mach number moving through gas at a fixed sound speed. The real picture is, however, more complicated: we have instead some number density of perturbers progressively decelerating through baryonic gas that is cooling as the Universe expands, with many wakes dissipating into heat throughout the cosmic volume. We have also not explored how the signal would change depending on the details of the cosmic dawn. Finally, since DF changes the bulk relative velocity between DM and baryons at cosmic dawn, this will also impact how baryons fall into DM potential wells when the first structures were formed [56]—we have not attempted to model the impact of this on the 21-cm signal in any way. A full treatment of DF and its impact on the 21-cm signal requires dedicated simulations, which we leave for future work.

Chapter 3

Three-Body Interactions with Primordial Black Holes

The search for dark matter (DM) has always spanned an enormous range of candidates and scales. For the past several decades, the field has been dominated by the prospect of discovering weakly interacting massive particles (WIMPs) at $\mathcal{O}(100\,\mathrm{GeV})$, but a wide variety of other possibilities have been recognized from the earliest days of DM science [143]. Now that collider searches and laboratory experiments have placed the WIMP paradigm under pressure [144, 145, 146], other classes of candidates at much lower and much higher mass scales are resurgent, from axion-like particles at $\mathcal{O}(10^{-20}\,\mathrm{eV})$ to dark compact objects at masses up to $100\,\mathrm{M}_{\odot}$.

The latter category subsumes many DM candidates predicted by a wide range of microphysical scenarios [147]. These include Q-balls [148, 36], boson stars [149, 32], axion miniclusters [109], and, most prominently, primordial black holes (PBHs) [8, 150, 151, 152, 30, 10, 153, 154]. Dark compact objects can contribute to the DM density over an enormous span of masses, but the parameter space of greatest interest at present is the so-called asteroid mass range, roughly 10^{-17}–$10^{-12}\,\mathrm{M}_{\odot}$ (10^{17}–$10^{22}\,\mathrm{g}$). In this window, no observational probes currently rule out compact objects as accounting for all of the DM, despite many ongoing efforts [155]. While microlensing is effective at higher masses, the typical Einstein radius of an asteroid-mass object is too small, rendering such probes ineffective due to the nonzero angular size of light sources and the nonzero wavelength of the light itself [156, 157, 158]. Additionally, PBHs in particular are unconstrained by evaporation in this regime, meaning that simple PBH models can account for the DM abundance without invoking any new degrees of freedom beyond those required for cosmic inflation [159].

Constraining asteroid-mass objects requires qualitatively new probes. One promising direction leverages the same philosophy that has historically been applied to constrain MAssive Compact Halo Objects (MACHOs) at masses of order $100\,\mathrm{M}_\odot$ and above: dynamical effects. It has long been recognized that if the DM consists of ultramassive objects, then encounters between these objects and stars will result in large perturbations to stellar trajectories. This was used to develop what may have been the very first constraint on the DM mass: in 1969, Ref. [160] argued that due to tidal distortions, DM could not be composed of objects with masses between 10^8 and $10^{13}\,\mathrm{M}_\odot$. Since then, with the advent of more sophisticated theoretical tools and much larger datasets, these constraints have been substantially refined, and provide robust limits on compact objects as DM at masses above $\sim 100\,\mathrm{M}_\odot$. Recently, several groups have proposed the use of high-precision timeseries measurements to search for perturbations induced by much smaller compact objects [161, 162, 163], with potential sensitivity in the unconstrained asteroid-mass window. Other proposals take advantage of dynamical processes that can leave a light perturber trapped in the system [26, 164, 165]. These ideas rely on the exquisite precision of measurements within the Solar System or in the immediate Solar neighborhood.

However, it is also possible that a wide variety of other systems might provide useful dynamical probes of light compact objects. Here, it is instructive to revisit the mechanisms that have been used in the past to constrain more massive compact objects.

The state of the art uses perturbations to wide binary systems [166, 167, 124, 168, 50, 169] or dynamical heating of cold systems [52]. The latter method provides a particularly intuitive explanation for the efficacy of constraints at this mass scale. The velocity distributions of stars and DM particles are comparable, each being determined by the Galactic potential. If the DM particle is much more massive than stars, then the effective temperature of the DM fluid is higher than that of the stellar fluid, meaning that energy is inevitably transferred as heat from the DM to the stellar distribution.

In the opposite limit, where the DM particle is much lighter than stars, the stars should transfer energy to the DM. This indeed takes place via dynamical friction [170]. One might thus hope to observe energy loss from binaries (i.e., hardening), as opposed to the energy gain (softening) used as a probe by Refs. [166, 167, 124, 168, 50, 169]. However, probing DM with dynamical friction is extremely challenging, and no known systems are capable of directly probing the dark matter abundance expected in their environments [171]. A major difficulty is the hierarchy of velocities between the DM and stellar binary components. As already anticipated in Chandrasekhar's original work [170], the dynamical friction induced by particles much faster than the binary's orbit is negligible. Typical binaries have orbital velocities of $\mathcal{O}(0.1\text{–}10\,\mathrm{km/s})$, whereas the DM velocity in the Galactic halo is $\mathcal{O}(230\,\mathrm{km/s})$. Thus, dynamical friction from DM on stellar binaries is strongly suppressed.

But dynamical friction is not the only means by which perturbers can harden a binary. Three-body processes feature complicated dynamics that can either soften or harden a binary, depending on the parameters of the encounter. As a rule of thumb, Heggie's law [172] states that binaries that are soft with respect to the perturber (i.e., with binding energy lower in magnitude than the energy of the perturber) are likely to soften further in an encounter, whereas binaries that are hard with respect to the perturber (i.e., with binding energy greater in magnitude) are likely to harden further. Since we are interested in light perturbers, which have accordingly low energy, typical binaries are already hard according to this classification, and thus might be further hardened by repeated encounters with light perturbers. This is a distinct effect from dynamical friction, which is an essentially many-body effect, and scales differently with the parameters of the binary and the perturbers.

Despite the differences between dynamical friction and three-body hardening, one caveat remains: the naïve interpretation of Heggie's law breaks down when the perturbers are much faster than the orbital velocity of the binary. Refs. [173, 174] have shown that in this regime, the average energy transferred from the binary to the perturber quickly vanishes. Thus, three-body hardening by dark compact objects is often neglected. However, as we will explain, three-body hardening is only suppressed in this regime when *averaged* over many encounters. If the number density of perturbers is low, a typical observing period may only feature one or several encounters. In this case, while the mean energy transferred is close to zero, the *width* of the distribution of energy transfers is not. This suggests a new opportunity in the regime of *rare, high-velocity* perturbers: the fast and the few.

In this chapter, we investigate such *stochastic* binary hardening due to light compact objects. We revisit the computation of the hardening rate originally performed by Refs. [173, 174], and develop a framework for estimating the energy transferred cumulatively over a small number of encounters. Since these perturbations can have either sign, the net effect is not "hardening," per se, but rather a kind of Poisson noise. We thus revive three-body dynamics as a probe of light compact objects, just as three-body softening has proven so valuable as a probe of massive compact objects.

This work is structured as follows. In section 3.1, we review the physics of three-body encounters, and discuss the evolution of Heggie's law from the original proposal in Ref. [172] to the revised versions of Refs. [173, 174]. In section 3.2, we update Heggie's law further to correctly account for stochasticity in the limit of few perturbations, and we develop a full estimate of the hardening rate in this regime. In section 3.3, we apply these results to a set of realistic systems, and evaluate the prospects for detecting compact objects by this means. We discuss our results and conclude in section 3.4.

Throughout this work, we denote quantities associated with the two objects in a binary by subscripts 1 and 2, and those associated with the perturber by a subscript 3. In particular, v_{12} denotes the relative velocity of the two components of the binary; v_3 denotes the velocity of the perturber relative to the center of mass of the binary; $m_{12} \equiv m_1 + m_2$ denotes the total mass of the binary; and E_{12} denotes the (negative) total mechanical energy of the binary. We denote the semimajor axis of the binary by a. We use a superscript star (e.g., $a^\star$) to denote parameter values used in reference simulations.

3.1 Three-body scattering

Three-body scattering is notoriously complicated, and outcomes are highly sensitive to initial conditions. Nonetheless, three-body encounters are important in a number of astrophysical contexts, particularly in cases where many encounters cumulatively affect the evolution of a binary. As a result, various heuristic and statistical approaches have been developed in the astrophysical literature to classify and predict the outcomes of an ensemble of three-body encounters. We now review the features of three-body encounters that have been well studied, and we situate the current work in that context.

3.1.1 Outcomes of three-body encounters

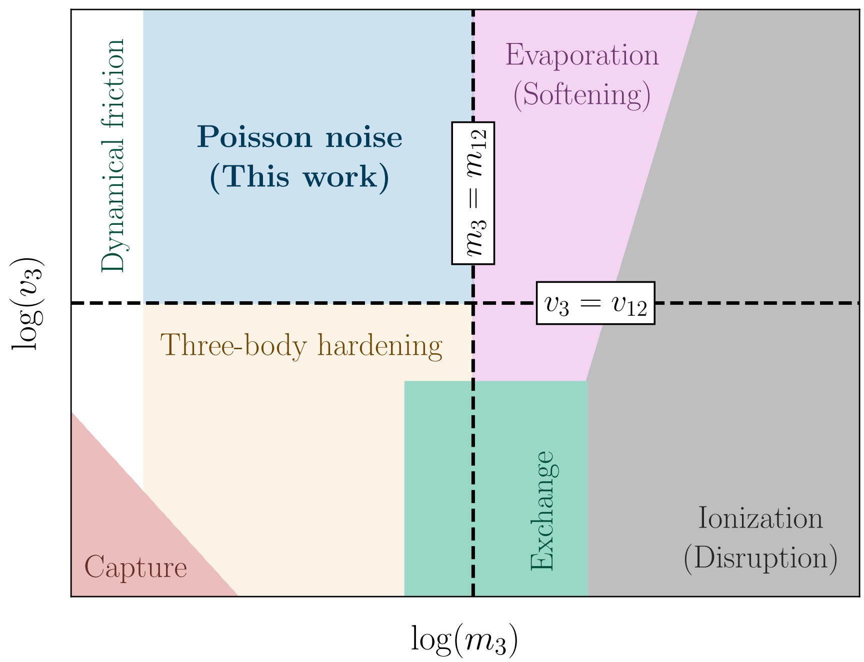

Figure 3.1: Schematic description of the regimes in which different processes are relevant. These regimes are shown in the plane of perturber mass and velocity, on logarithmic axes. The boundaries between regions are only illustrative: realistically, several of these processes can occur in overlapping regions. Note that "evaporation" and "ionization" are terms used in the three-body scattering literature to refer to softening and disruption, respectively, and are unrelated to Hawking evaporation and atomic ionization. The dashed black lines indicate the mass and velocity of the binary. In this work, we study the light blue region, where velocities are high (*fast*), but number densities are still low (*few*) compared to the dynamical friction regime.

Three-body encounters can be usefully classified on an energetic basis. The initial mechanical energy of the binary and the perturber determine important features of the encounter, and outcomes can be classified by the final energies of the objects. Specifically, given a particular perturber, the binary can be categorized as "hard" (tightly bound) or "soft" (weakly bound) with respect to the perturber, which we will soon define concretely. A classic paper by Heggie [172] shows that *on average,* a hard binary becomes harder following a three-body encounter, whereas a soft binary becomes softer. This is known as Heggie's law.

This is easy to understand in the limit of an extremely hard or extremely soft binary. Consider a binary system with component masses m_1 and m_2 and semimajor axis a, and a perturber with mass m_3 and velocity v_3. Now, suppose that $m_3 \gg m_1, m_2$, and suppose that v_3 is comparable to the orbital velocity of the binary. During the encounter, the potential binding the components of the binary is small compared to the potential sourced by the perturber, so the interaction of the perturber with each component is well approximated by elastic $2 \to 2$ scattering. In the limit of large m_3, corresponding to a very soft binary, the typical energy transfer to each component is large compared to the binding energy. Thus, a generic encounter leads to a final state in which the components are free, i.e., the binary is no longer bound. This is called "disruption" or "ionization," and corresponds to extreme softening. On the other hand, for an extremely hard binary with $m_1, m_2 \gg m_3$ and orbital velocity $v_{12} \gg v_3$, the scattering process tends to accelerate the perturber, causing the binary to become more tightly bound (harder).

Disruption is only kinematically allowed for soft binaries. The total energy of the three-body system, measured in the rest frame of the center of mass of the binary, is given by

$$E_{123} = \frac{1}{2} m_3 v_3^2 - \frac{G m_1 m_2}{2a}. \tag{3.1}$$

Disruption entails that all three objects are free in the final state, so the total energy must be positive in the initial state. Thus, conservation of energy only allows for disruption if the binary is sufficiently soft in the initial state. On the other hand, if the total energy of the three-body system is negative, at least two objects must remain bound in the final state, but these need not be the original components of the binary. In certain cases, the perturber can transfer enough energy to one component to disrupt the binary, but lose so much energy in the process that the perturber becomes bound to the other component. These are exchange processes. On the other hand, if the initial energy of the perturber is too low, then it can become bound without unbinding either component of the binary, forming a triple system. These are capture processes.

All of these processes have been used as probes of dark compact objects. The disruption process has been used extensively as a probe of compact objects that are much more massive than stars, i.e., in the regime where binaries are typically soft [175, 176, 177, 166, 178, 167, 124, 168, 50, 169]. Capture and exchange processes have also been studied for this purpose [179, 164, 26], as they become relevant for dark compact objects at different masses. However, designing probes based on softening and hardening, beyond the simplest disruption processes, requires a more precise formulation of Heggie's law. The rate of softening and hardening—and indeed, whether these take place at all—cannot be determined directly from the energetics of the perturber. A precise definition of hard and soft binaries, as well as their distinguishing characteristics, is required.

The definition of hard and soft binaries is a topic of significant debate. According to Heggie [172], a binary system should be considered hard if its binding energy is much greater than the kinetic energy of the perturber, or soft if the binding energy is much less than the kinetic energy of the perturber. A second definition was given by Hills [180], who found that in numerical experiments, perturbers traveling faster than the binary's orbital speed, v_{12}, tend to soften the binary, while those traveling slower tend to harden it. The analytical estimates provided by Heggie align with the numerical experiments conducted by Hills when all three objects involved in the encounter have the same mass. However, if the third object is fast but is significantly less massive than the two binary stars, the two definitions are in conflict.

This is particularly problematic for constraining compact objects as a DM candidate. The objects of greatest interest are those in the asteroid-mass range, much lighter than the components of most observationally-accessible binaries, but DM particles or compact objects have velocities on the order of the dispersion of the Galactic halo, much faster than typical binary orbits. The various outcomes of three- or many-body encounters are illustrated schematically in the plane of perturber mass and velocity in fig. 3.1, for particular choices of binary parameters. The remaining window for compact object DM corresponds to the top-left quadrant of the figure (light blue), in the regime where the classical hardening and softening behaviors are not readily applicable. Understanding hardening and softening in this regime requires different methods.

3.1.2 Hardening via multiple encounters

The issue of fast low-mass objects was first addressed by Gould [173] and later investigated numerically by Quinlan [174]. (See also Ref. [181].) We first give a concrete definition of the hardening rate considered in that work. Consider a binary in a background of perturbers with fixed abundance and velocity. Ref. [174] defines a dimensionless energy transfer

$$C = \frac{m_{12}}{2m_3}\frac{\Delta E_{12}}{E_{12}}, \tag{3.2}$$

and the hardening rate is the average value of C over all of the parameters of a three-body encounter. The hardening rate determines how fast the orbit of the binary with semimajor axis a would shrink in a medium of perturbers with number density n, and is defined as

$$\frac{\mathrm{d}}{\mathrm{d}t}\left(\frac{1}{a}\right) = \frac{Gnm_3}{v_3}H_1. \tag{3.3}$$

In practice, we define $\langle C\rangle|_b$ to be the average of C over all angular parameters at fixed impact parameter b. Ref. [174] then computes the hardening rate H_1 by

$$H_1 = 8\pi\int_0^\infty \mathrm{d}b\,\frac{b}{b_0^2}\,\langle C\rangle|_b, \tag{3.4}$$

where b_0 is the impact parameter with pericenter distance equal to the semimajor axis, i.e., $r_p = a$, with r_p defined by the relation

$$b^2 = r_p^2 \left(1 + \frac{2Gm_{12}}{r_p v_3^2}\right). \tag{3.5}$$

That is, $b_0^2 = a^2[1 + 2Gm_{12}/(av_3^2)]$. The definition of H_1 averages the dimensionless energy transfer over possible impact parameters, weighted by their cross sections: the cross section for an impact parameter b corresponds to the area of a circle of radius b, so the appropriate measure of integration is $b\,\mathrm{d}b$. The definition of b_0 accounts for gravitational focusing: slow objects have pericenter distances much smaller than their impact parameters.

Notice that the hardening effect from multiple successive three-body encounters is distinct from the traditional definition of dynamical friction. Dynamical friction slows a massive object at a rate

$$\dot{\mathbf{v}}_1 = -\frac{16\pi^2 \log(\Lambda) G^2 m_1 \rho_3 \mathbf{v}_1}{v_3^3} \int_0^{v_1} \mathrm{d}v\, v^2 f(v), \tag{3.6}$$

where f is the velocity distribution function and $\log\Lambda$ is a Coulomb logarithm, typically $\mathcal{O}(10)$. This is second-order in G. Physically, this is because dynamical friction is due to the interaction of a massive object with its wake in the density field: as particles pass by the massive object, they are gravitationally focused into an overdensity on the other side, which then pulls the massive object back. Dynamical friction couples the velocity of a single massive object to the average velocity of the medium, independent of the three-body dynamics that take place when perturbers interact with a binary.

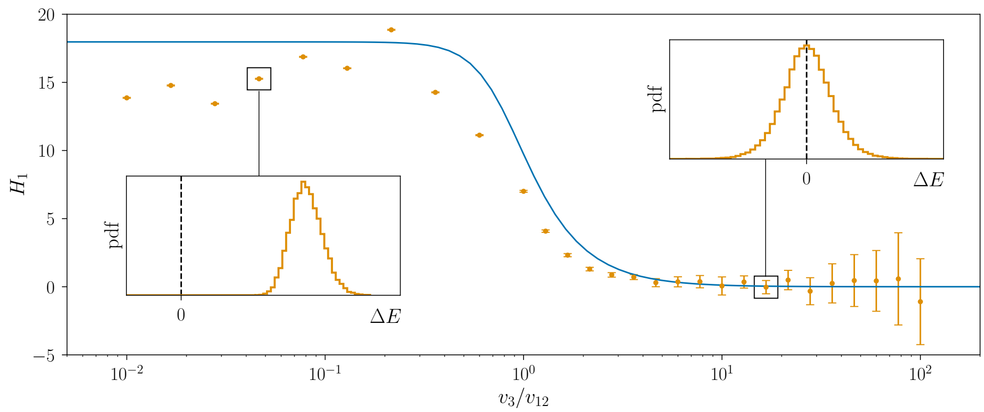

Figure 3.2: Hardening rate as a function of velocity. Orange points are computed from an ensemble of simulations. The blue curve shows the fit from Ref. [174]. Error bars indicate 1σ uncertainties on the mean values. Insets show the full distribution of energy transferred in a single encounter for selected velocities, and are shown to scale. For high perturber velocities $v_3 \gg v_{12}$, while the mean energy transfer goes to zero, the width of the distribution remains nonzero.

Thus, although there are some similarities between dynamical friction and three-body hardening, the two are not the same, and the effects we discuss here need not match onto dynamical friction in the low-mass limit.

Figure 3.2 shows the hardening rate as a function of perturber velocity, as computed by Quinlan [174]. Quinlan further provides a fitting formula for the velocity dependence, as

$$H_1(v_3) = H_1(0)\left[1 + \left(\frac{v_3}{v_{12}}\right)^4\right]^{-1/2}, \tag{3.7}$$

from which we may note that the hardening rate is suppressed by $(v_3/v_{12})^{-2}$ for large perturber velocities $v_3 \gg v_{12}$. Based on these findings, Quinlan proposed a new convention for classifying hard binaries: a binary system with masses $m_1 \geq m_2$ should only be considered hard if the perturber velocity falls below a critical threshold of the form

$$v_3 \lesssim 0.85\, v_{12}\sqrt{\frac{m_2}{m_{12}}}, \tag{3.8}$$

where the value of the prefactor and the scaling behaviors with masses were extracted from numerical experiments.

To understand this definition, observe that further hardening of the binary in a three-body encounter corresponds to acceleration of the perturber by the gravitational slingshot mechanism. Here, the perturber (m_3) has a close encounter with the lighter of the two bodies (m_2), undergoing a process that is very nearly elastic two-body scattering in the center-of-mass frame of m_2 and m_3. Since m_2 and m_3 have a close encounter, each mass experiences the same acceleration due to m_1, so the encounter can be treated as a two-body scattering process that takes place in an accelerated reference frame. Thus, in the center-of-mass frame of m_2 and m_3, the speed of recession is equal to the speed of approach, so the encounter corresponds to a deflection of the perturber. When this final state is transformed out of the accelerated m_2-m_3 frame, back to the inertial center-of-mass frame of the entire three-body system, this deflection corresponds to the acceleration or deceleration of the perturber, depending on the details of the encounter.

If $m_3 \ll m_2 \ll m_1$, then the center-of-mass frame of m_2 and m_3 is approximately the rest frame of m_2 alone, and the center-of-mass frame of the entire system is approximately the rest frame of m_1, which sits at the barycenter. The accelerated m_2-m_3 frame follows the orbit of m_2 around m_1. In this case, working in the barycentric rest frame, where $v_1 \approx 0$, the mass m_3 can only be accelerated (i.e., the binary can only be hardened) if $v_3 < v_2$ prior to the encounter. This means that some hardening processes are only available for low-velocity perturbers, even at very low energies. The critical perturber velocity below which the binary should be considered hard cannot be inferred strictly from the relative energy of the binary and the perturber: the relative velocities themselves are necessary, regardless of the masses.

The dynamics involved in hardening are quite complicated, so, despite these arguments, the speed at which the transition from hard to soft occurs is difficult to identify from first principles. Quinlan's seminal work was oriented towards computing the hardening rate of massive black hole binaries. Such massive binaries have high velocities, typically larger than the Galactic dispersion velocity. As such, it was not necessary for Quinlan to evaluate the hardening rate for $v_3 \gg v_{12}$, nor would this have been particularly interesting: the evolution of massive black hole binaries proceeds over long timescales subsuming many encounters, so the average hardening rate can be used directly, and the $(v_3/v_{12})^{-2}$ suppression then implies that hardening due to fast-moving perturbers is negligible.

However, when considering encounters between a MACHO and a system such as a binary pulsar, the situation is very different. Firstly, the binary velocity is much lower, so perturbers with the Galactic dispersion velocity are quite fast: $v_3 \gg v_{12}$. Secondly, the period of observation is much shorter, with far higher precision. Measurements of binary pulsars in particular are exquisitely sensitive to the gain or loss of energy, but unlike massive black hole binaries, the evolution of the system is not influenced by many successive encounters over the relevant timescale. For some compact object populations, the expected number of close encounters in the observing period is $\mathcal{O}(1)$. This means that while the *average* hardening rate does suffer from a substantial suppression, the average is not necessarily the appropriate quantity.

In particular, while the average value of the hardening rate is quickly suppressed at large v_3, the rms value of the energy transfer decays much more slowly. As shown in the insets of fig. 3.2, the width of the distribution of energy transfers across encounters is nearly the same for perturbers in the slow and fast regimes, and this width is not much smaller than the mean value itself for slow perturbers. This suggests that the most promising route for detecting encounters of this type might lie in their *stochasticity:* while many encounters average away to null effect, the Poisson noise associated with a few encounters might be detectable. We thus label the top-left quadrant of fig. 3.1 as the "shot noise" regime, and in the next section, we study the statistics of these stochastic perturbations in detail.

3.2 Statistics of multiple perturbations

As summarized in the preceding section, it is well known that fast-moving perturbers will neither harden nor soften a binary, on average. That is, the distribution of perturbations delivered to the energy of a binary has a mean of zero. However, this distribution still has nonvanishing width, and if there are not very many encounters over a given period of measurement, there is a nonvanishing stochastic hardening rate expected. In this section, we develop a set of semianalytical estimates for the size of these perturbations, calibrate them using simulations of three-body encounters, and validate them using Monte Carlo sampling.

3.2.1 Analytical framework

To understand the origin (and eventual disappearance) of these stochastic fluctuations, suppose that each perturber encounter imparts a change δE in the energy of the binary. The perturbation δE is a random variable whose distribution has some variance σ_E^2. Now, consider several successive perturbations $\delta E_1, \ldots, \delta E_N$ over the observing period. By the central limit theorem, for large N, the total perturbation $\Delta E^{(N)} = \delta E_1 + \cdots + \delta E_N$ is normally distributed with a variance of $N\sigma_E^2$. For light perturbers with $m_3 < m_{12}$, observe that δE scales linearly with the mass of the perturber, meaning that $\sigma_E^2 \propto m_3^2$, while $N \propto 1/m_3$ if the mass density of perturbers is held fixed. This means that $N\sigma_E^2 \propto m_3$, so at large N, $\Delta E^{(N)}$ is normally distributed with a standard deviation that scales as $m_3^{1/2}$, vanishing in the low-mass limit.

In other words, stochastic perturbations arise because the energy transferred in each encounter has a high variance but a mean of zero. The total energy transfer thus behaves as a random walk, with an expectation scaling with the square root of the number of encounters. The number of encounters is inversely proportional to the mass, but this growth at low mass is compensated by the linear mass dependence of the energy transfer in each encounter.

In the rest of this subsection, we make this picture firmly quantitative. Firstly, we define a figure of merit for comparison with observations. We then identify the scaling behavior of this quantity with the parameters of the perturbations. Finally, we define an estimator that combines the effects of many perturbations to serve as a quick indicator of observational accessibility.

3.2.2 From encounters to detection probabilities

For observational purposes, the most important quantity is not the expectation value of the total energy transfer, but rather, the probability that the total energy transfer exceeds some threshold $E_{\min}$. We denote this probability by p_{obs}. Formally, p_{obs} can be written as

$$p_{\text{obs}} = \sum_{k=1}^{\infty} \mathbb{P}(N = k) \times \mathbb{P}\Big(\big|\Delta E^{(k)}\big| > E_{\min}\Big), \tag{3.9}$$

i.e., the probability of exceeding the threshold with exactly k encounters weighted by the probability of having exactly k encounters, summed over all values of k.

The probability $\mathbb{P}(N = k)$ of encountering exactly k perturbers is just the pmf of the Poisson distribution $\mathrm{Poiss}(\lambda)$, where λ is the average number of perturbers expected to interact with the system over the observing period. Computing the exact distribution of $\Delta E^{(k)}$ is challenging for a general distribution of δE, but we can easily approximate p_{obs} in two regimes. First, if $\lambda \ll 1$, we can neglect all terms $k > 1$, so that we need only $\Delta E^{(1)}$, which has the same distribution as δE. On the other hand, if $\lambda \gg 1$, we can approximate the Poisson distribution as a delta distribution at its mode, writing $p_{\text{obs}} \approx \mathbb{P}\big(\big|\Delta E^{(\lambda)}\big| > E_{\min}\big)$. We can then use the central limit theorem to evaluate the distribution of $\Delta E^{(\lambda)}$, obtaining

$$p_{\text{obs}}(\lambda) \approx \begin{cases} \lambda e^{-\lambda} \mathbb{P}\big(|\delta E| > E_{\min}\big) & \lambda \ll 1, \\ \\ \mathrm{erfc}\left(\dfrac{E_{\min}}{\sigma_E \sqrt{2\lambda}}\right) & \lambda \gg 1. \end{cases} \tag{3.10}$$

The quantity $E_{\min}/(\sigma_E\sqrt{2\lambda})$ scales with $m_3^{-1/2}$, so at large λ (small m_3), the probability $p_{\rm obs}$ is exponentially suppressed. However, when λ is $\mathcal{O}(1)$, $p_{\rm obs}$ can be significantly enhanced over the case of a normal distribution. Specifically, $p_{\rm obs}$ is enhanced for rare encounters if the distribution of δE has heavier tails than a normal distribution with the same variance. We will see that this is indeed the case for three-body encounters.

3.2.3 Scalings with encounter parameters

We can also estimate the dependences of $p_{\rm obs}$ on other parameters of the perturbers. In particular, as long as the encounter is fast, we can use the impulse approximation. Assuming that the imparted momentum to the binary, δp_{12}, is small compared with the momentum p_i of each component, the imparted energy is given by $\delta E \simeq (p_{12}/m_{12})\, \delta p_{12}$. The impulse approximation predicts that the imparted momentum scales as $\delta p_{12} \propto m_3/v_3$, and therefore, so does δE.

We can also predict the behavior with the impact parameter, at least at large b. Here, while the impulse approximation would predict a b^{-1} scaling for the momentum imparted to a single component, the perturbation to binary parameters depends only on the difference between the momenta imparted to the two components: if m_1 and m_2 are given the same impulse, the only perturbation is to the center of mass of the binary, not to the relative configuration of the components. When the perturber encounters one component with impact parameter b, the impact parameter with respect to the other differs by $\mathcal{O}(a)$. Thus, while the momentum imparted to the first component scales with b^{-1}, the momentum imparted to the second is of order $(b+a)^{-1}$, so the difference between them scales with $b^{-1} - (b+a)^{-1}$, or a/b^2 for large b. This is equivalent to the statement that the binary is perturbed by the tidal potential, for which the impulse goes like $1/b^2$ for $b \gg a$. For $b < a$, an exact prediction is difficult, but the dependence on b should be much gentler, and we approximate it as constant, imposing continuity at $b = a$. At this point, this is purely an assumption, but we will soon see from numerical simulations that it provides a good fit to the energy transfer as a function of impact parameter. Putting these components together, we have

$$\delta E(b) \simeq \delta E^\star \left(\frac{m_3}{m_3^\star} \frac{m_{12}}{m_{12}^\star} \right) \left(\frac{v_3}{v_3^\star} \frac{a}{a^\star} \right)^{-1} T(a,b);\; T(a,b) = \begin{cases} 1 & b < a, \\ \left(\frac{b}{a}\right)^{-2} & b > a, \end{cases} \tag{3.11}$$

where $\delta E^\star$ is the energy transfer for reference parameters $m_3^\star$ and $v_3^\star$, which must be determined by numerical simulations.

3.2.4 Combining multiple perturbations

Now, recognizing that σ_E has the same scalings as δE, we can use the large-λ limit of eq. (3.9) to estimate the parametric dependence of the overall probability of observation over many encounters. Consider successive annuli of impact parameters with boundaries $\{b_1, \ldots, b_n\}$. The contribution of each annulus to the total perturbation ΔE is a normally distributed random variable with standard deviation $\sigma_k = \sqrt{\lambda_k}\sigma_E \times [\delta E(b_k)/\delta E^\star]$, where λ_k is the average number of objects passing through the kth annulus. The total perturbation is then a normally distributed random variable with variance

$$\sigma_{\text{tot}}^2 = \sum_k \sigma_k^2 = \sigma_E^2 \left(\frac{m_3 m_{12} v_3^\star a^\star}{m_3^\star m_{12}^\star v_3 a} \right)^2 \sum_k \lambda_k T(a,b), \tag{3.12}$$

and the total probability of an observable perturbation is given by $p_{\rm obs} \approx p_{\rm many} \equiv \mathrm{erfc}(E_{\rm min}/\sqrt{2}\sigma_{\rm tot})$. The mean number of objects passing through each annulus is given by

$$\lambda_k = \frac{\rho_3 v_3\,\Delta t}{m_3} \times \pi(b_{k+1}^2 - b_k^2) \simeq \frac{2\pi b_k\,\rho_3 v_3\,\Delta t}{m_3}\,\Delta b, \tag{3.13}$$

meaning that the sum in eq. (3.12) can be approximated as an integral in the continuum limit. Strictly speaking, this is doubly approximate, since $\lambda_k \to 0$ as $\Delta b \to 0$, meaning that there is only a small number of encounters. This invalidates the application of the central limit theorem, which only holds for a sum of many random variables. As such, the use of eq. (3.12) in this regime cannot be justified a priori, and constitutes a separate assumption. Notwithstanding this caveat, we have

$$\sum_k \lambda_k T(a,b) \approx \int_{b_{\rm min}}^{b_{\rm max}} \mathrm{d}b\,\frac{2\pi b\rho_3 v_3\,\Delta t}{m_3}\,T(a,b) \tag{3.14}$$

$$= \frac{\pi\rho_3 v_3\,\Delta t}{m_3}\left[\left(a^2 - b_{\rm min}^2\right)\Theta(a - b_{\rm min}) + 2a^2\log\left(\frac{b_{\rm max}}{\max\{b_{\rm min}, a\}}\right)\right]. \tag{3.15}$$

The $b_{\rm max}$ dependence persists in the form of a Coulomb logarithm, typically of order 10. However, since this computation only applies for fast encounters, we set $b_{\rm max}$ such that the crossing time of a perturber fits within the observing period, i.e., $b_{\rm max} = v_3\,\Delta t$, which can result in a much smaller (or vanishing) Coulomb logarithm. We choose $b_{\rm min}$ such that $\lambda = \lambda_{\rm min}$ for $b < b_{\rm min}$, i.e., $b_{\rm min} = \sqrt{\lambda_{\rm min} m_3/(\pi\rho_3 v_3\,\Delta t)}$, and we take $\lambda_{\rm min} = 10$ in computations. Now we can write the probability of an observable perturbation as

$$p_{\rm many} \simeq \text{erfc}\left[\frac{E_{\rm min} m_3^\star m_{12}^\star a/(\sigma_E v_3^\star m_{12} a^\star) \times \sqrt{v_3/(2\pi\rho_3 m_3\,\Delta t)}}{\sqrt{\left(a^2 - b_{\rm min}^2\right)\Theta(a - b_{\rm min}) + 2a^2\log\left(\frac{b_{\rm max}}{\max\{b_{\rm min}, a\}}\right)}}\right]. \tag{3.16}$$

This result indicates that we can neglect the slow-moving tail of the DM velocity distribution: the pdf of the speed distribution scales as v_3^2 at small v_3, so the factor $\sqrt{v_3/\rho_3}$ in the numerator goes as $1/\sqrt{v_3}$, meaning that the argument of erfc diverges in the low-velocity limit.

For $\lambda < 1$, the central limit theorem does not apply, and combining perturbations from different impact parameters is nontrivial. However, we can still make a similar estimate using the fact that $\lambda e^{-\lambda}$ is fairly sharply peaked at $\lambda = 1$, with a width of $\mathcal{O}(1)$. We thus conservatively take just a single annulus $b_{\rm min} < b < b_{\rm max}$ such that the width $\Delta b \equiv b_2 - b_1$ is half of the average value of b on the annulus and such that $\lambda = 1$. We neglect all energy transfers originating from encounters with impact parameters outside this annulus. This corresponds to

$$b_1 = \sqrt{\frac{8m_3}{(9+\sqrt{33})\pi\rho_3 v_3\,\Delta t}}, \quad b_2 = \frac{1}{4}\left(1+\sqrt{33}\right)b_{\rm min}, \tag{3.17}$$

with $\langle b\rangle \approx 0.57\sqrt{m_3/(\rho_3 v_3\,\Delta t)}$. However, we must also impose the requirement that $\langle b\rangle < b_{\rm max}$, so we take $b = \min\{\langle b\rangle, b_{\rm max}\}$ and $\Delta b = \frac{1}{2}b$, and compute λ as in eq. (3.13). Then the probability of an observable perturbation from an encounter within just this annulus is

$$p_{\rm obs} \;\approx\; p_{\rm ann} \;\equiv\; \lambda(b)e^{-\lambda(b)}\mathbb{P}\Big(\big|\delta E(b)\big| \;>\; E_{\rm min}\Big); \quad b \;=\; \min\{\langle b\rangle\,, b_{\rm max}\}. \quad (3.18)$$

An independent conservative estimate is to admit only $0 < b < a$, i.e., impact parameters that cross within the orbit of the binary. This gives a lower bound, and since there is no b dependence in this regime, the estimate is straightforward:

$$p_{\rm obs} \;\approx\; p_{\rm orb} \;\equiv\; \frac{\pi\rho_3 v_3 b^2\,\Delta t}{m_3}\exp\left(-\frac{\pi\rho_3 v_3 b^2\,\Delta t}{m_3}\right) \times\; \mathbb{P}\big(|\delta E(b)| \;>\; E_{\rm min}\big). \quad (3.19)$$

where $b = \min\{a, b_{\rm max}\}$. Since these are two different conservative estimates, the actual probability should be greater than each one. Thus, we conservatively estimate the total probability of an observable perturbation as the maximum of the probability through each of these channels, i.e.,

$$p_{\rm tot} \approx \max\left\{p_{\rm orb}, p_{\rm ann}, p_{\rm many}\right\}. \quad (3.20)$$

3.2.5 An estimator for probability of observation

In typical scenarios, $p_{\rm tot}$ exhibits two peaks as a function of m_3, since $p_{\rm orb}$ and $p_{\rm ann}$ dominate over $p_{\rm many}$ but peak at different masses, which we denote by $\hat{m}_{\rm orb}$ and $\hat{m}_{\rm ann}$, respectively. This doubly-peaked behavior is an artifact of the division between these

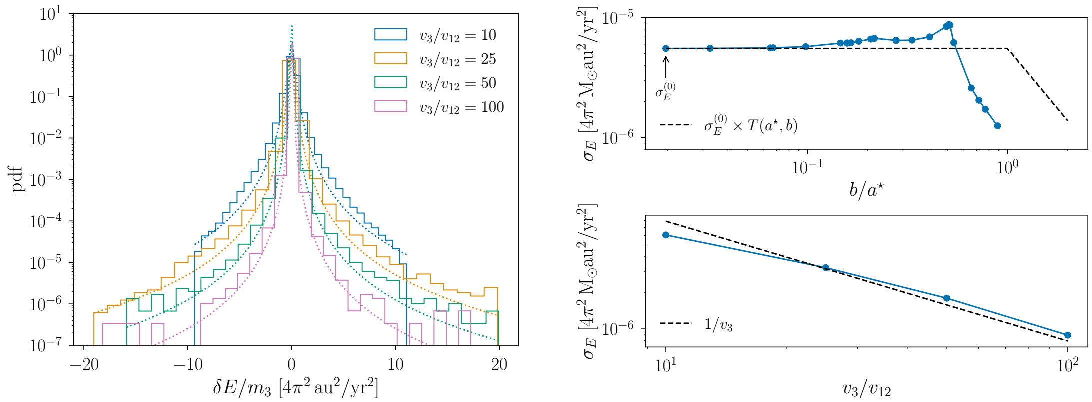

Figure 3.3: **Fits to simulation ensembles.** *Left:* Energy transfer distributions in an ensemble of simulations for several values of v_3/v_{12}. Dotted curves show the fitted t distribution (see text). *Top right:* dependence of the variance σ_E on the impact parameter of the encounter. The dashed curve shows the behavior implied by our approximation $T(a, b)$ (eq. (3.11)). *Bottom right:* dependence of σ_E on the perturber velocity. The dashed line shows a fit to the $1/v_3$ scaling assumed in eq. (3.11).

different channels. We thus define an alternative estimator $p_{\hat{\mathrm{obs}}}$ as

$$p_{\hat{\mathrm{obs}}}(m_3) \equiv \begin{cases} \min\{\max p_{\mathrm{orb}},\, \max p_{\mathrm{ann}}\} & m_3 \in [\hat{m}_{\mathrm{orb}}, \hat{m}_{\mathrm{ann}}] \\ \\ p_{\mathrm{tot}}(m_3) & \text{otherwise.} \end{cases} \tag{3.21}$$

The estimator $p_{\hat{\mathrm{obs}}}$ will be crucial to our results in later sections, and we will validate it with Monte Carlo sampling shortly.

With this formalism, we can now estimate the probability of an observable perturbation in a wide range of scenarios with only one numerical input: the standard deviation σ_E for one set of reference parameters. In the next section, we compute σ_E directly using numerical simulations.

3.2.6 Calibration with three-body simulations

To directly compute the distribution of the energy transfers between a binary system and a fast-moving perturber, we simulate an ensemble of encounters using the N-body simulation code REBOUND [182]. Our configuration consists of an equal-mass binary system with a fixed semimajor axis $a^\star$. We take the binary to be circular, i.e., we fix the eccentricity e to zero. The state of the binary is then determined by four parameters: the cosine of the inclination $\cos\theta_i \in (-1, 1)$, the longitude of the ascending node $\Omega \in (0, 2\pi)$, the argument of pericenter $\omega \in (0, 2\pi)$, and the mean anomaly $M \in (0, 2\pi)$ at some fixed time. We randomly sample these parameters while holding the initial conditions of the perturber fixed.

The perturber, with mass $m_3 \ll m_{12}$, is placed at coordinates $(x, y, z) = (b, 0, z_0)$. The squared impact parameter b^2 is sampled uniformly from the interval $(0, b_{\max}^2)$, where $b_{\max}$ is determined by eq. (3.5) with r_p randomly selected from the interval $[0, a^\star]$. The final result is not sensitive to z_0 as long as $z_0 \gg b_{\max}$. We take $z_0 = 25b_{\max}$ in our computations. The perturber is given an initial velocity $\mathbf{v}_3 = (0, 0, -v_3)$. We evolve the system using the `ias15` integrator [183], and we stop integration when the perturber both **(1)** exits a sphere with a radius twice that of z_0 and **(2)** has positive mechanical energy.

Some integrations, particularly for slower perturbers, can be computationally expensive because the perturber can be captured into metastable orbit, only exiting the system after many periods. To avoid such lengthy simulations, we impose an upper limit on the integration time. If the integration exceeds 10^4 steps, the specific simulation is discarded. The binding energy of the binary is calculated both before and after the encounter to assess the energy exchange. This process is repeated 10^5 times for each impact parameter to determine $\langle C \rangle$. Finally, this procedure is carried out for 25 randomly sampled impact parameters.

From these simulations, we extract the distribution of δE as a function of the parameters of the encounter. Empirically, we find that the distribution of δE is well approximated by Student's t distribution with a scale parameter. We denote this distribution by $\mathcal{T}(\xi, \nu)$, where ξ is the scale parameter and ν is the number of degrees of freedom. The pdf is given by

$$f_{\mathcal{T}}(t) = \frac{1}{\xi\sqrt{\nu}\ \mathrm{B}\left(\frac{1}{2}, \frac{1}{2}\nu\right)} \left(\frac{\nu}{\nu + (t/\xi)^2}\right)^{\frac{1}{2}(\nu+1)}, \tag{3.22}$$

where B denotes the beta function. The (unscaled) t distribution typically arises as the distribution of a random variable $T = \sqrt{\nu} Z / \sqrt{X}$, where $Z \sim \mathcal{N}(0, 1)$ and $X \sim \chi^2(\nu)$. While it is possible that a similar structure underlies the appearance of the t distribution in this case, the resemblance is only approximate, and it is quite possible that the similarity is purely coincidental. As such, we make no effort to derive this distribution from first principles, but treat it as an empirical fit. (However, see Ref. [184] for an extensive analytical discussion of the energy transfer distribution, with very similar properties to those found here.) When fitting to simulated data, we fit only the ν parameter, and fix the scale parameter ξ by the requirement that the variance of the fitted distribution matches the variance of the data, using the fact that

$$\mathrm{Var}(\mathcal{T}) = \frac{\nu \xi^2}{\nu - 2}. \tag{3.23}$$

Accordingly, ν is the only free parameter. We do not constrain ν to be an integer. Note that this is only self-consistent if $\nu > 2$. As $\nu \to 2^+$, the variance diverges, and our analysis assumes that the variance of δE is well-defined. For the case of an equal-mass binary with component masses $1\,\mathrm{M}_\odot$ and separation $1\,\mathrm{AU}$, we find a best-fit value $\nu = 2.29$ across the entire dataset.

The resulting fits are shown for several perturber velocities in the left panel of Fig. 3.3, demonstrating broad compatibility of the empirical data with the t distribution. Moreover, the scaling arguments of Fig. 3.2 are borne out by these numerical experiments. The right panel of Fig. 3.3 shows the dependence of the fitted σ_E on impact parameter (top) and perturber velocity (bottom), approximately matching the expectations from eq. (3.11).

3.2.7 Estimated detection probability

Now that we have determined the distribution of perturbations δE for a benchmark scenario, we can use the estimators in eqs. (3.20) and (3.21) to study the observability of perturbers under various conditions. In particular, we can now replace $\mathbb{P}(|\delta E| > E_{\min})$ with the cdf of the appropriate t distribution from the previous subsection, and we can replace σ_E with the square root of the variance computed in our simulations. This means that we can now explicitly evaluate $\hat{p}_{\mathrm{obs}}$ and the other estimators for a given set of parameters to determine the probability of an observable perturbation occurring in a given system.

First, we consider all four estimators: $p_{\rm many}$, $p_{\rm ann}$, $p_{\rm orb}$, and $\hat{p}_{\rm obs}$. Figure 3.4 shows results for each estimator for an equal-mass circular binary system with semimajor axis $a = 1\,\mathrm{AU}$ and equal component masses ($m_1 = m_2 = 1\,\mathrm{M}_\odot$), varying the perturber mass m_3. Here we set $v_3 = 230\,\mathrm{km/s}$ and $\rho_3 = 0.4\,\mathrm{GeV/cm}^3$, typical of the DM distribution in the Solar neighborhood. In effect, we consider the DM to be made entirely of compact objects of mass m_3 for each point. This means that the number density of perturbers scales inversely with m_3.

Now, observe that $p_{\rm many}$ is non-negligible only for a narrow portion of the mass range. This corresponds to the estimated probability that one would derive from the central limit theorem, with sufficiently many encounters in the observing period. There is a sharp cutoff at high mass as the mean number of encounters drops below $\lambda_{\rm min}$. On the other hand, there is also a sharp cutoff at low mass: in this regime, there is a large number of encounters whose energy transfers follow the same distribution, and the mean energy transfer falls rapidly, as predicted by eq. (3.10). Indeed, contributions from many similar encounters ($\lambda \gg 1$) are subdominant to the single-encounter contribution $p_{\rm ann}$, which dominates at both the highest masses and the lowest masses. This means that even in a regime where there are many encounters overall, the probability of a detectable perturbation is still driven by rare single encounters that impart greater energy. In the intermediate regime, where the rate of encounters with $b \lesssim a$ is $\mathcal{O}(1)$, the interior contribution $p_{\rm orb}$ dominates. Thus, as anticipated in the definition of $\hat{p}_{\rm obs}$, the estimators $p_{\rm ann}$ and $p_{\rm orb}$ have distinct peaks. The estimator $\hat{p}_{\rm obs}$, shown by the dashed black line in

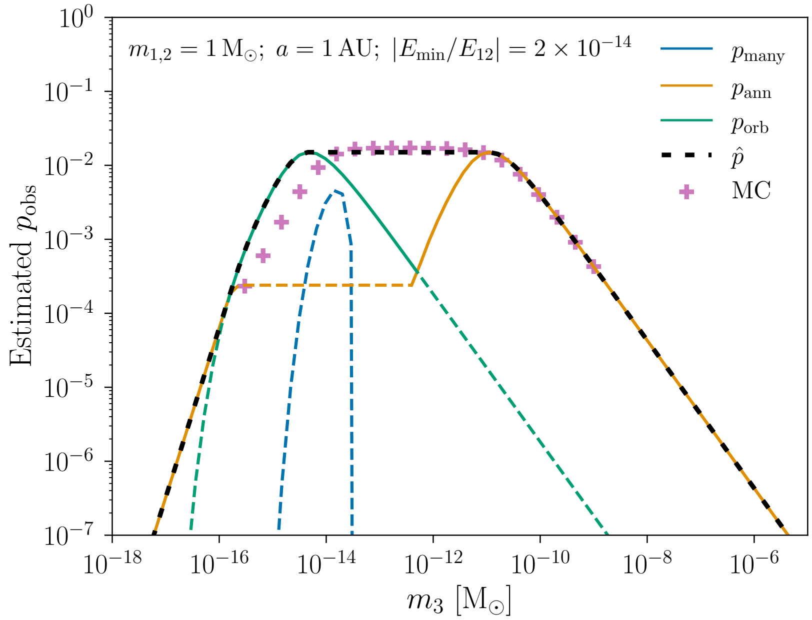

Figure 3.4: Components of eqs. (3.20) and (3.21) for an equal-mass circular binary with component masses $m_1 = m_2 = 1\,\mathrm{M}_\odot$ and semimajor axis $a = 1\,\mathrm{AU}$. An observing time of $1\,\mathrm{yr}$ is assumed, with all of the DM in the form of compact objects at mass m_3, and the minimal energy transfer for detection is taken to be a 2×10^{-14} fraction of the mechanical energy of the binary, chosen to make the curves distinct for illustrative purposes. Blue, orange, and green curves show the values of individual estimators p_{many}, p_{ann}, and p_{orb}, respectively. Each of these curves is solid where it is the greatest of the three, and dashed elsewhere. The dashed black curve shows the value of the estimator $\hat{p_{\mathrm{obs}}}$. Crosses show results from Monte Carlo sampling of the t distribution (see text).

fig. 3.4, bridges the gap between these peaks.

These estimators are meant to approximate the distribution of sums of draws from the distribution of δE. As such, to the extent that the t distribution is a good approximation of the true distribution of energy transfers, these probabilities can be accurately computed by Monte Carlo methods, i.e., by numerically sampling such multiple draws from the underlying distribution. For each perturber mass m_3, we first sample the Poisson-distributed number of encounters during the observing period. For each en-

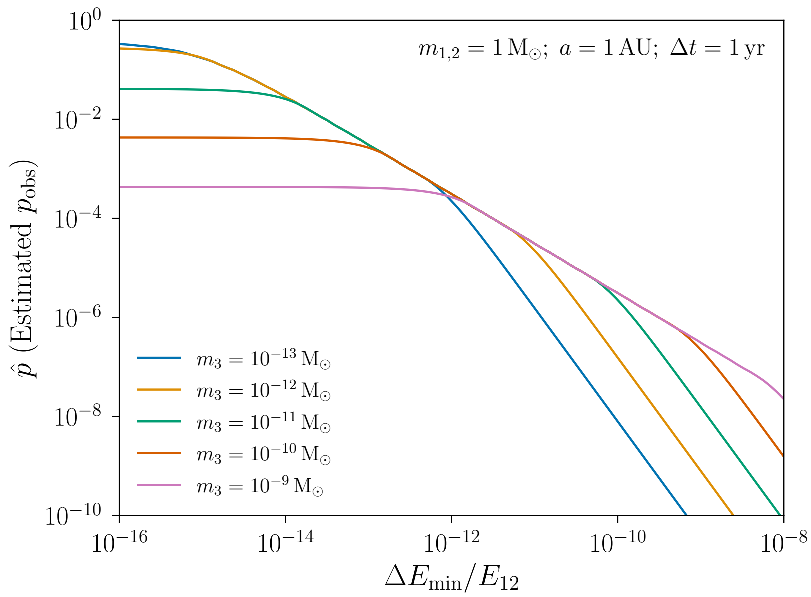

Figure 3.5: Detection probability as a function of minimum detectable energy for several perturber masses. In the limit of a low detection threshold, the detection probability is limited by the rate of encounters, and increases to 1 at low masses.

counter, we then sample δE from the distribution described in eqs. (3.22) and (3.23), and sum these samples to obtain ΔE. We repeat this process many times to obtain the distribution of ΔE at each m_3, and then compute the probability that ΔE exceeds $\Delta E_{\rm min}$. The resulting probabilities are shown by the crosses in fig. 3.4 ("MC"). Despite the many approximations we have made in this section, the detection probabilities computed by Monte Carlo are in remarkably good agreement with the analytical estimator $\hat{p}_{\rm obs}$ (dashed black).

We can now use $\hat{p}_{\rm obs}$ to understand the probability of an observable perturbation occurring in various systems. Figure 3.5 shows $\hat{p}_{\rm obs}$ as a function of the threshold energy transfer for a detection, $\Delta E_{\rm min}$, in ratio to the total energy of the binary, E_{12}. At high thresholds, larger perturber masses (m_3) result in a higher probability of an observable perturbation. But at low thresholds, the detection rate is bottlenecked by the encounter

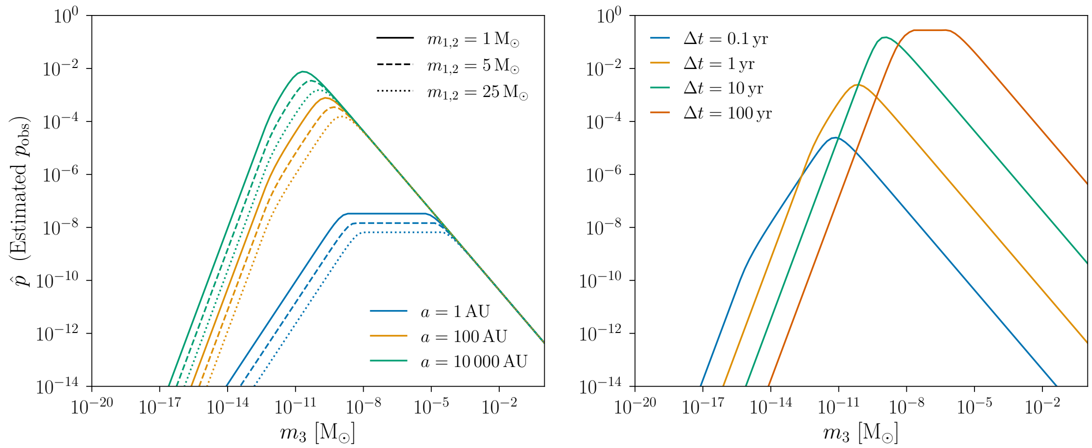

Figure 3.6: Detection probability estimator $\hat{p}_{\mathrm{obs}}$ for varying binary parameters and observation times. Both panels assume a minimum detectable energy ΔE_{min} corresponding to an average $\dot{P}_{12} = 10^{-8}$ over the observing period, where P_{12} is the period of the binary. ***Left:*** varying binary component masses (line styles) and semimajor axes (colors). The observing time is fixed to $1\,\mathrm{yr}$. ***Right:*** varying observation time. The component masses are fixed to $m_{1,2} = 1\,\mathrm{M}_\odot$, and the semimajor axis is fixed to 10^3 AU.

rate, so higher masses, corresponding to lower number densities, are disfavored. Even at very low thresholds, the estimator $\hat{p}_{\mathrm{obs}}$ only increases to 1 when m_3 is low enough to ensure a sufficiently high encounter rate. Figure 3.6 shows the behavior of $\hat{p}_{\mathrm{obs}}$ as a function of m_3 for varying binary masses, semimajor axes, and observation times. For illustration purposes, the detectable energy threshold is set to correspond to a fixed (dimensionless) time derivative of the orbital period P_{12}, enforcing that $\dot{P}_{12} \geq 10^{-8}$. It is immediately obvious from the figure that when fixing precision, wider binaries offer much greater probabilities of detectable perturbations. Binaries with lower component masses are also favored, since transferring the same amount of energy results in a larger change in the period.

The behavior with increasing observation time, shown in the right panel of fig. 3.6, is also easy to understand. We are seeking a stochastic signal, so the probability of a detectable perturbation, $\hat{p}_{\text{obs}}$, is largest when about one large perturbation can be expected, i.e., when the mean number of perturbers with the appropriate parameters is $\mathcal{O}(1)$. The mean number of perturbations, N, increases linearly with the observing time, and the size of the total perturbation follows the scaling of a random walk, proportional to $\sqrt{N}$. Thus, the energy transfer scales with $\sqrt{\Delta t}$, so the time-averaged hardening rate scales as $1/\sqrt{\Delta t}$. This means that if the precision on the average rate of hardening over the observing time is held fixed, a long observing time sufficient to observe many encounters is *disfavored.* This is visible at low masses (high number densities), where the detection probability decays with observing time. On the other hand, the probability of observing a rare encounter with a heavy perturber, with rate already suppressed by low number density, is enhanced with increased observing time. Thus, the probability curve shifts mainly to the right (higher masses) rather than up (to higher probabilities). This should not be interpreted to suggest that longer observations are inherently less powerful for probing low masses. It is strictly a consequence of fixing the precision on the average hardening *rate*.

It is also apparent from fig. 3.6 that with some of the parameter combinations exhibited here, wide binaries would plausibly probe PBH DM in the unconstrained asteroid-mass range. Motivated by this observation, we now turn to the consideration of real astrophysical systems that might exhibit the appropriate properties to serve as compact object detectors.

System	m_1 [$M_\odot$]	m_2 [$M_\odot$]	$a_{\rm proj}$ [AU]	e	θ_i [°]	$\dot{P}_{12}$	$\{\vert\Delta P_{12}\vert/P_{12}/m_3\}^\star$ [$M_\odot^{-1}$]	Ref.
J1713−0747	1.33	0.29	0.0648	7.49×10^{-5}	71.69	3.4×10^{-13}	1.2923	[185]
J1903+0327	1.67	1.03	0.211	0.4367	77.47	-3.3×10^{-11}	0.8804	[186]
J2016+1948	1	0.29	0.302	1.48×10^{-3}	58.58	–	0.8137	[187]
J1740−3052	1.4	19.5	1.52	0.5789	53	3×10^{-9}	0.1271	[188]
B1259−63	2	19.8	2.60	0.8698	154 ± 3	1.4×10^{-8}	0.0900	[189, 190]

Table 3.1: A selection of several observed wide binary pulsars with precisely measured orbital decay rate. Here $a_{\rm proj}$ denotes the projected semimajor axis; e denotes the eccentricity; θ_i denotes the inclination angle; and $\dot{P}_{12}$ gives the measured rate of change of the orbital period of the system. (To our knowledge, a value of $\dot{P}_{12}$ has not been reported in the literature for J2016+1948.) The column $\{|\Delta P_{12}|/P_{12}/m_3\}^\star$ gives the average value of $|\Delta P_{12}|/P_{12}$ measured in a set of simulated individual encounters, in ratio to the mass of the perturber. The simulations are performed with a light perturber, $m_3 \ll m_{12}$, in the regime where the size of the perturbation to the period is linear in m_3.

3.3 Realistic systems and observational prospects

Having developed a flexible estimator of the probability of an observable perturbation, we now consider the astrophysical systems that might lend themselves to a detection of compact objects as DM.

3.3.1 General features of sensitive systems

The first consideration that drives the sensitivity to perturbers is the encounter rate itself. Recall that for a given observing time, Δt, the maximum perturber distance that we consider in this work is given by $b_{\max} = v_3\,\Delta t$, which bounds the encounter rate above by

$$\Gamma \lesssim n_3 v_3 \times \pi b_{\max}^2 \;=\; 4\,\mathrm{yr}^{-1} \times \left(\frac{m_3}{10^{-13}\,\mathrm{M}_\odot}\right)^{-1}\left(\frac{\Delta t}{1\,\mathrm{yr}}\right)^{2}\left(\frac{v_3}{230\,\mathrm{km/s}}\right)^{3}. \quad (3.24)$$

The fact that this rate is $\mathcal{O}(1)$ over a typical observing time for objects in the asteroid-mass range is the very fact that enables the Solar System probes of Refs. [161, 162, 163]. While the same is true in principle here, it is important to note that, as shown in section 3.2, the width of the energy transfer distribution—i.e., the figure of merit for stochastic perturbations—declines as $(b/a)^{-2}$ for $b \gtrsim a$. Thus, the width of the distribution is greatest in a region which has a cross-section $\sim a^2$, and the purpose of detection is best served by wider binaries.

On the other hand, the other key consideration is the precision with which a perturbation can be measured. In this work, we consider just one possible signal of a perturbation: a change in the period of a binary system. If a binary is hardened or softened, the orbital period will shift slightly. For an equal-mass circular binary, the period, semimajor axis, and total energy are simply related. The period is given by $P_{12} = 2\pi\sqrt{a^3/(2Gm_1)}$, whereas the total energy is given by $E_{12} = -Gm_1^2/(2a)$. For small perturbations, therefore, we have

$$\frac{\Delta P_{12}}{P_{12}} = -\frac{3}{2}\frac{\Delta E_{12}}{E_{12}}. \tag{3.25}$$

The best observational prospects are thus found in systems where the period is long (i.e., wide binaries) and can be measured with high precision. These two desiderata are often in conflict, as we will see later on.

Note that our analysis is based largely on circular binaries. Realistically, typical binaries are somewhat eccentric. While more complex, this may in fact offer a more sensitive probe of compact objects than the semimajor axis alone. Indeed, Ref. [172] showed that the change in eccentricity induced by three-body encounters can be much more significant than the change in energy.

For the moment, however, we consider energy transfer alone, and we first consider systems where the period is known with exceptional precision. One set of such systems is provided by the Solar System itself, again providing natural motivation for the work of Refs. [161, 162, 163] focusing on Solar System objects. But the Solar System is not the only setting for precision measurements. A natural alternative is provided by binary pulsars, which are extremely well modeled. In the remainder of this section, we evaluate the prospects for compact object detection via three-body encounters with such systems.

3.3.2 Observational prospects in binary pulsars

Many binary pulsar systems have been detected and characterized at extremely high precision, especially as components of pulsar timing arrays for gravitational wave detection [191, 192, 193, 194]. The result is a large set of systems with separations comparable to Solar System orbits and, at the same time, reasonably high precision on the measurement of the period. As with the Solar System, such systems have been famously used for many tests of general relativity [195, 196, 197, 198, 199, 200, 201, 202], with extraordinary sensitivity to anomalous accelerations, and it is thus natural to consider using them as a detector for compact objects. In fact, in general terms, several authors have previously considered the possibility that perturbers might leave a mark in pulsar timing data used for gravitational wave detection [203, 204, 205, 206, 207, 208, 209]. They have even been used as settings for the study of dynamical friction [171, 210]. We now consider the possible use of pulsars for compact object detection in our framework. Note that we only assume sensitivity to changes in the average period over the entire observing window, not transient fluctuations.

The properties of a set of example binary pulsars is given in table 3.1, including the observed rate of change of the period, $\dot{P}_{12}$. For each of these systems, we conduct an ensemble of simulations of three-body encounters with a light perturber of mass $m_3^\star \ll \min\{m_1, m_2\}$, and we determine the average magnitude of the change in the period, $|\Delta P_{12}|$, resulting from each encounter. Since these simulations are in the test-particle regime, with $m_3^\star \ll m_{1,2}$, the energy imparted, and thus the change to the period, is linear in the mass of the perturber. Accordingly, $|\Delta P_{12}|$ can be predicted for perturbers

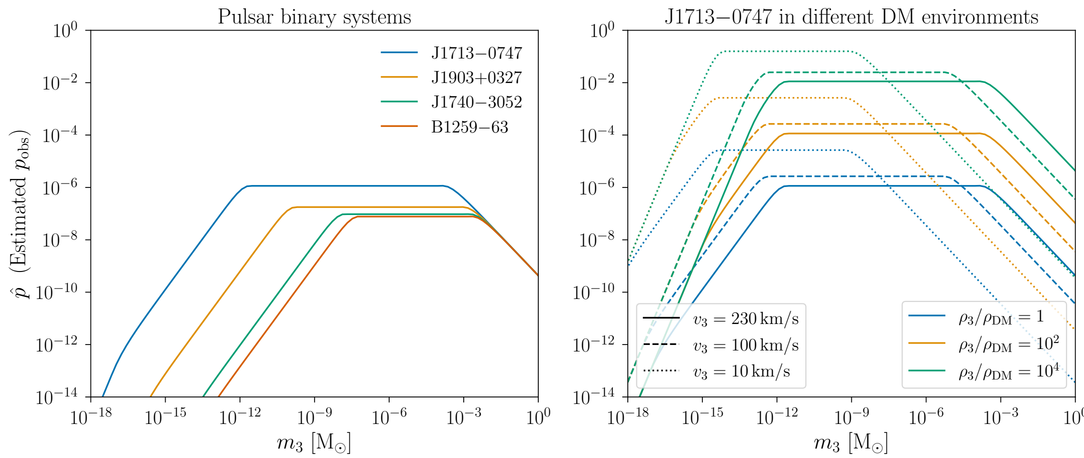

Figure 3.7: Detection probability estimator $\hat{p_{\rm obs}}$ for a variety of astrophysical systems with parameters based on those listed in table 3.1. Here, each binary is taken to be circular, with equal component masses given by the mean of m_1 and m_2. The minimum detectable perturbation to the period is conservatively taken to be equal to the measured value of ΔP_{12}, i.e., $\dot{P}_{12}$ integrated over the observing time. Since $\dot{P}_{12}$ is not available for J2016+1948, we exclude this system from consideration here.

of smaller masses by a simple rescaling. We report the results of these simulations in table 3.1 in the form $|\Delta P_{12}|/P_{12}/m_3^\star$, so the expected value of $|\Delta P_{12}|/P_{12}$ for a single encounter can be obtained by multiplying this column by the perturber mass. (Note that while we report the results in units of $\mathrm{M}_\odot^{-1}$, linearity only holds for $m_3 \ll \mathrm{M}_\odot$.)

To estimate the sensitivity of these systems to perturbers of varying masses, we evaluate our estimator $\hat{p}_{\rm obs}$ under a set of approximations. We consider a $10\,\mathrm{yr}$ observation of each of these systems, and approximate the rate of perturbations by taking each system to be an equal-mass circular binary, holding the total mass and semimajor axis fixed. We conservatively estimate the minimum detectable perturbation by taking the precision on ΔP_{12} to be equal to the measured value of ΔP_{12} implied by $\dot{P}_{12}$ over the entire observing period. (We exclude J2016+1948, since $\dot{P}_{12}$ is not available for this system.) We show the resulting estimated probability of detecting a perturbation for each of these systems in the left panel of fig. 3.7. These probabilities are generally small and are dominated by the system J1713−0747, which offers a compromise between semimajor axis and precision. In the right panel of fig. 3.7, we thus show the probabilities that would be obtained in the case of DM overdensities (i.e., large ρ_3) or cold features (i.e., small v_3). J1713−0747 has a percent-level probability of an observable perturbation in the case of a 10^4 overdensity of DM, increasing to $\mathcal{O}(10\%)$ in a cold feature with $v_3 \sim 10\,\mathrm{km/s}$.

All of these probabilities are still well below 1. This is not surprising: it is well known that no single binary pulsar system can constrain compact objects as DM. But the possibility of a stochastic effect offers the prospect for a new class of search. Rather than studying a single system, it is plausible that a combination of several or many systems with non-negligible $\hat{p}_{\mathrm{obs}}$ might yield a nontrivial constraint. Our estimator provides a quick method of estimating the sensitivity enabled by observations of various systems, or combinations thereof.

For example, note that at fixed m_3 and Δt, under the assumptions made here, there is an optimal separation for a system, beyond which sensitivity is degraded. This is immediately visible in fig. 3.8, which illustrates the relative importance of semimajor axis and observational precision. For the case shown here, with perturber mass $m_3 = 10^{-10}\,\mathrm{M}_\odot$, binary component masses $m_{1,2} = 1\,\mathrm{M}_\odot$, and an observing time of $\Delta t = 1\,\mathrm{yr}$, the optimal separation is 10–$100\,\mathrm{AU}$. This is considerably larger than the typical separations of binary pulsars. Figure 3.8 also demonstrates the tradeoff between precision and separation: the binary pulsars of table 3.1 are marked by stars, and the precision of measurement is degraded at higher separations. Thus, robust constraints

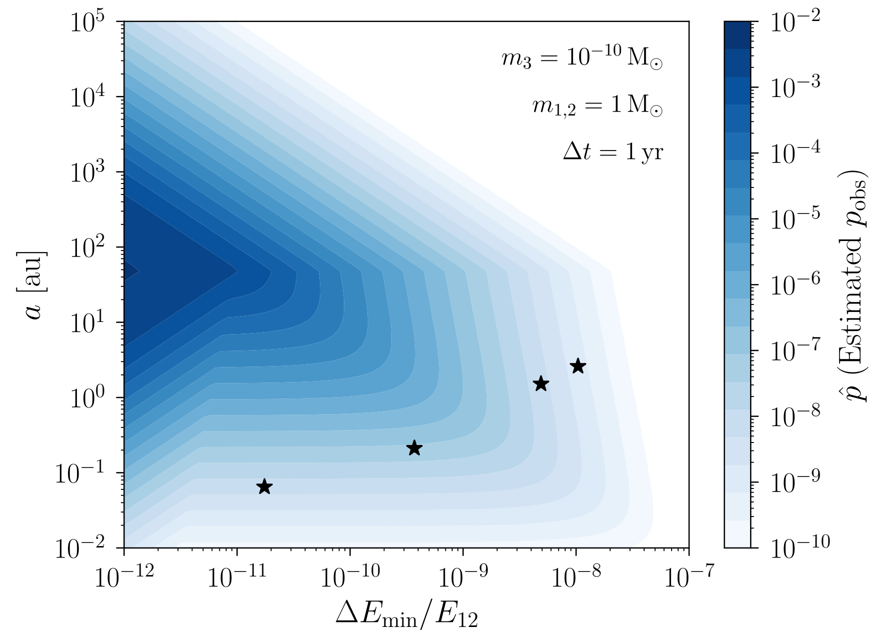

Figure 3.8: Detection probability as a function of minimum detectable energy and binary semimajor axis for a fixed perturber mass $m_3 = 10^{-10}\,\mathrm{M}_\odot$ and binary component masses $m_1 = m_2 = 1\,\mathrm{M}_\odot$, over an observing period of $1\,\mathrm{yr}$. The binary pulsar systems of table 3.1 are marked with stars.

on compact objects may need to wait for higher precision or a new set of systems. For pulsars in particular, the discovery of a vast number of new systems is anticipated at the Square Kilometer Array (SKA), which is also expected to considerably improve the precision of pulsar timing measurements [211, 212]. The associated improvement in precision on pulsar binary parameters should be significant, but a quantitative estimate is nontrivial and beyond the scope of the present work. We note that several new types of system will be accessible in the coming decades with future gravitational wave experiments, which also offer precise measurements of orbital periods. We defer detailed consideration of these systems and their potential sensitivities to future work.

3.4 Conclusions

The purpose of this work is twofold. On the one hand, we advance a novel probe of dark compact objects such as PBHs, with potential applications to a challenging mass range. On the other hand, as a purely astrophysical problem, we complete the panoply of three-body encounter outcomes shown in fig. 3.1, identifying rich structure in a portion of the parameter space often regarded as empty in the past.

Beginning with the latter component, we have shown in this work that dynamical effects from three-body encounters can in fact have a hardening or softening effect, despite astrophysical lore that their speed renders this impossible. While the regime of fast perturbers faces a suppression in energy transfers compared to slow perturbers, this is compensated for by stochasticity: in the limit of few perturbers, the net effect is potentially discernible. This provides a satisfying coda to the story originally started by the work of Refs. [172, 173, 174]: the average shrinks to zero, but the width does not, leaving a stochastic effect in this regime. Thus, the analogue of the hardening rate is the rate of detectable perturbations in either direction. Here, we have developed a semianalytical framework for computing this rate, summarized in our statistical estimator $\hat{p}_{\rm obs}$.

It is easy to understand why such effects have not been considered in the past. Generally, one is interested in the long-term evolution of systems rather than perturbations of the kind we study here. Over a long timescale, the effects we identify in this work vanish. In cases such as supermassive black hole evolution, three-body hardening is only relevant at stages where the velocity of the binary is large enough compared to the Galactic halo dispersion. At other times, dynamical friction is the correct framework, and exhibits different behavior.

Our sensitivity projection also explains the utility of objects in the Solar System as probes for dark compact objects, as discussed in detail by Refs. [161, 163]. The projections in these works assume resolution of the orbit of e.g. Mars that corresponds to a precision of $\mathcal{O}(10^{-12}$–$10^{-14})$ on the period. Under these conditions, the plateau in the detection probability is in the range $(\hat{m}_{\rm orb}, \hat{m}_{\rm ann}) \simeq (10^{-14}, 10^{-8})\mathrm{M}_{\odot}$, and within this plateau, the detection probability is $\mathcal{O}(1)$, with $\hat{p}_{\rm obs} \simeq 30\%$. Thus, our framework reproduces the statement that the Solar System can plausibly detect compact objects in the asteroid-mass window. Moreover, we can now describe Solar-System–based detection proposals in the same framework as three-body hardening (at low masses and velocities) and three-body softening (at high masses and velocities).

Pragmatically, the utility of the method we develop here is that it can be readily applied to potential targets well beyond the Solar System. The challenge is to identify systems with the optimal balance of large separation and high-precision period measurements. In this work, we have applied our computation to binary pulsars, which have their periods measured to high precision. The size of perturbations is sensitive to the velocity of the perturbers, making this technique a uniquely powerful probe of DM structures with low velocity dispersion. We verify that the currently observed wide binary pulsars cannot constrain the Galactic halo in the absence of an overdensity or cold feature, but future measurements can potentially improve the precision to enable sensitivity to the diffuse Galactic halo.

In searches involving wide binary systems, current precision measurements primarily rely on astrometric methods, such as those from Gaia observations [213], which have been used to constrain massive compact objects [124]. Due to Gaia's relatively short observation baseline, of order 10 years, it cannot directly measure orbital decay rates over multiple successive orbits for binaries with very wide separations. For example, the semimajor axis of a binary with $1\,\mathrm{M}_\odot$ components with an orbital period of 10 years is about $6\,\mathrm{AU}$, so for these masses, multiple orbits can only be observed for systems with considerably smaller separations. This does not preclude measuring orbital decay rates with sufficiently high precision on partial orbits, and the next-generation astrometry mission, Theia, is expected to enable improved measurements with its higher astrometric accuracy and longer observation time [214]. Future prospects include binaries that can be observed and monitored precisely with the Laser Interferometer Space Antenna (LISA) [215, 216]. The double white dwarf binaries expected to be measured by LISA would exhibit baseline orbital decay rates as small as $\mathcal{O}(10^{-16}\,\mathrm{s}^{-1})$ due to gravitational wave emission. However, the separations of such binaries remain below $1\,\mathrm{AU}$, facing challenges similar to those encountered with binary pulsars.

Our results also clarify the connection between the regime in which multiple three-body encounters are relevant and that in which dynamical friction is relevant. In the limit of a large number of encounters with light perturbers, the rate of hardening from three-body encounters regresses to its average value, and vanishes, leaving only dynamical friction. On the other hand, when the number of close encounters over the observing period is small, the individual perturbations are substantial and do not efficiently average to zero. (Interestingly, ultralight DM may be detectable by the same means, since stochastic fluctuations in such a field can similarly perturb binaries over short timescales [217, 218].)

Note that while pulsar binary systems that we consider in table 3.1 are sensitive to DM only in the presence of overdensities, such overdensities are also sufficient to observe the effects of particle DM via dynamical friction in the same systems, as discussed in detail by Refs. [210, 171]. Thus, systems sensitive enough to detect dynamical friction are likely also sensitive to stochastic three-body interactions. This suggests that detection of DM by these means would also readily reveal whether the DM is particle-like or compact-object–like. In some regimes, dynamical friction and stochastic perturbations appear quite differently in time series data, with the former entering as a smooth effect and the latter as a set of transient events. Even in the absence of such timeseries data, since dynamical friction and three-body perturbations scale differently with the properties of the binary, comparing the size of the effect over a long time in two or more systems can provide robust discrimination between these two scenarios.

Finally, we stress that in this work, we have focused on the stochastic effects that dominate when the perturbers are fast relative to the binary components. While this is typically the case for realistic binaries in the Galactic halo, there are exceptions, e.g. in short-period systems or in very cold DM environments. Thus, there are some scenarios where traditional time-averaged three-body hardening may apply, and constraints on light perturbers may be derived from population properties of hard binaries. We defer consideration of these systems to future work.

Our results point the way towards a powerful method to constrain the mass of individual DM constituents even in the challenging asteroid-mass window. Few-body dynamical probes of the kind we propose here may have provided the first-ever bound on the DM mass [160]. Remarkably, as we have shown in this work, there is yet further information to be extracted from these processes—and they may yet provide decisive bounds on compact objects as DM.

Chapter 4

Three-body Exchange with Primordial Black Holes

The microphysical identity of cosmological dark matter (DM) remains unknown. Given the difficulty in accounting for cosmological observables by modifications to gravity, the DM is thought to be made up of a new particle species beyond the Standard Model. Another possibility, however, is that part or all of the DM is in the form of primordial black holes (PBHs) produced at early times [8, 150, 151, 152, 10, 30, 219, 153]. Given the null results of many particle DM searches, and an abundance of new observational probes of black holes (BHs), interest in PBHs as a DM candidate has surged over the last decade.

PBHs as DM are constrained by a multitude of observables over many decades in mass [152, 10, 30]. It is generally agreed that PBHs cannot account for all of DM outside a narrow window of masses, around 10^{17}–$10^{23}\,\mathrm{g}$ [157, 220, 158, 155]. Still, PBHs may account for up to 10% of the DM abundance in other key mass ranges, such as the planetary mass scale, 10^{-7}–$10^{-3}\,\mathrm{M}_{\odot}$. As such, there has been a robust community effort to develop new observables that might further constrain or produce direct evidence of such objects.

One of the key approaches relies on the dynamics of these objects [50, 221, 222, 223, 52, 175, 224, 176, 177, 178, 169]. On large scales, PBHs are indistinguishable from a fluidlike background of particle DM. But on sufficiently small scales, the inhomogeneity of the PBH distribution relative to particle DM leads to unique phenomenology. In particular, such objects can lose their kinetic energy via interactions with stellar systems. One simple way to understand this is via thermodynamics [52]: since PBH velocities are determined by the global properties of a galactic halo, the effective temperature that characterizes the PBHs' phase space distribution scales with the PBH mass. Since stars have comparable velocities, this implies that when the PBH mass is significantly larger than the stellar masses, the PBH fluid is hotter, and tends to heat the stellar fluid.

Beyond these considerations which apply to the stellar distribution as a whole, PBHs can also participate in few-body encounters with binary systems, with behavior that is radically different from particle DM. In particular, a single three-body encounter between a PBH and a binary system can transfer enough energy to substantially widen or even unbind the binary. This means that the distribution of binary widths can be used to constrain the population of would-be perturbers such as PBHs, and this exact process has historically provided some of the most important constraints on massive PBHs with $M_{\mathrm{PBH}} \gtrsim 100\,\mathrm{M}_{\odot}$ [175, 224, 176, 177, 178, 169].

But the exchange of energy is not the only possibility in three-body encounters, which have been extensively studied in other contexts [172, 225, 174, 226]. Consider the scattering of three bodies 1, 2, and 3, where 1 and 2 are initially bound and 3 is initially free. In general, there are five possible outcomes:

1. Hardening: objects 1 and 2 remain bound, and they give up energy to object 3, causing their separation to decrease. Object 3 remains free.

2. Softening: object 3 transfers energy to the 1-2 system, causing their separation to increase, but they remain bound. Object 3 remains free.

3. Disruption: object 3 transfers so much energy to the 1-2 system that the two objects are unbound. All objects become free.

4. Capture: objects 1 and 2 remain bound, and now object 3 becomes bound as well, forming a triple system. In the process, 3 donates energy to the 1-2 system, softening the binary.

5. Exchange: object 3 transfers enough energy to object 1 to unbind it from 2, but in the process, 3 loses enough energy that it becomes bound to 2. The result is a bound 2-3 system with object 1 free.

Softening and disruption by PBHs have been considered extensively in the literature [175, 224, 176, 177, 178, 169], and PBH capture has also been treated by Ref. [164]. For reasons that we will explain in the next section, hardening processes involving PBHs are strongly suppressed in all realistic systems.

This leaves one untapped possibility: exchange processes, where a PBH ejects one component of a binary system and forms a new binary with the other component. The end result of this process is a single visible object that has dynamic characteristics of a binary component. That is, such an object appears to be dancing with an invisible partner, with potentially observable implications. Here we investigate the possibility that such a population of invisible partners exists in our Galaxy, and we survey the observational approaches that might be used to establish their presence.

Identifying a binary composed of a PBH and a visible object would require a means of ruling out an astrophysical origin for the BH component of the binary. For subsolar-mass BH components, this only requires establishing that the object is in fact a BH. However, we will see that the most promising prospects for detecting PBH exchange are in stellar binaries, at PBH masses comparable to astrophysical BH masses. Here, a primordial origin can be established by rejecting standard astrophysical formation channels. Interestingly, the *Gaia* mission [227] has detected several BH-star binary systems that pose a challenge to standard astrophysical binary formation models, with orbital periods too long and mass ratios too large to have been produced from isolated binaries that underwent a common-envelope phase. As we will demonstrate, PBH exchange is potentially viable as an origin for these systems, implying that BH components in BH-star binaries may, in fact, be identifiable as PBHs.

The remainder of this chapter is organized as follows. In section 4.1, we review the generalities of the three-body exchange process, and detail our calculation of exchange rates. In section 4.2, we systematically consider the classes of binary systems that might be amenable to the exchange process. In section 4.3, we examine the possibility that observed BH-star binaries may form via PBH exchange. We discuss our findings and conclude in section 4.4.

4.1 Three-body processes

Three-body dynamics is a notoriously complicated subject, with a paucity of fully general analytical results. Still, for the exchange processes that will be of interest to us, we can leverage approximations that have been developed in the astrophysics literature and validated against suites of numerical experiments. We now summarize these results as they apply to PBH exchanges with binaries. In this section, and in the rest of this

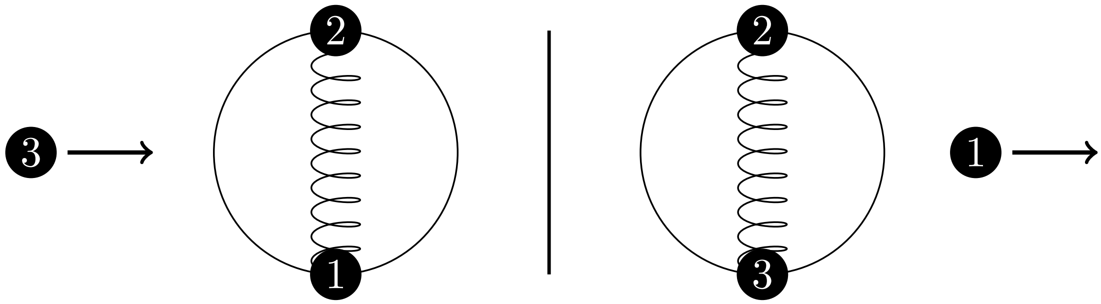

Figure 4.1: Summary of notation. In the initial state, objects 1 and 2 are bound, and object 3 is free. In the final state, objects 2 and 3 are bound, and object 1 is free.

work, we use the following notation: we take the three objects to have masses m_1, m_2, and m_3. We use the label 3 to denote the free object in the initial state, that is, the PBH. We use the label 2 to denote the binary component that forms a new binary with the PBH in the final state, and we use the label 1 to denote the object that is ejected in the encounter. This is summarized in fig. 4.1. We further define

$$m_{ij} \equiv m_i + m_j, \qquad m_{123} \equiv m_1 + m_2 + m_3, \tag{4.1}$$

and we write $\mu_1 \equiv m_1/m_{12}$ and $\mu_2 \equiv m_3/m_{123}$. We denote the semimajor axis of the initial binary by a, and denote the velocity of the incoming object at infinity by v_3, or equivalently by v_{PBH} when our discussion is specific to PBHs.

One of the major complications in the study of three-body processes is the sensitivity to initial conditions: slight variations in the parameters of the system can lead to wildly different outcomes. However, we are mainly interested in the rate of certain three-body processes on average, over a large number of systems. This is considerably simpler to analyze, since it is often possible to analytically describe the statistics of outcomes of three-body encounters. In particular, the seminal work of Heggie [172] and Hills [225] provides a simple framework for estimating the rates of various processes.

As regards energy transfer, their results can be summarized in Heggie's law, which states that in a three-body encounter, on average, hard binaries become harder (or "shrink") and soft binaries become softer (or "expand"). For these purposes, a binary system is considered hard if its binding energy U_{12} is much greater than the average kinetic energy $\frac{1}{2}m_3\langle v_3^2\rangle$ of the third object. Conversely, a binary system is classified as soft if $U_{12} \ll \frac{1}{2}m_3\langle v_3^2\rangle$ [228]. The disruption of stellar binaries as a strategy to constrain exotic objects has a long history: it has been effective in setting bounds on MACHOs [175, 224, 176, 177, 178, 169] and DM substructure [166, 124, 167]. Our goal in this work is to explore the other possible outcomes of PBH encounters.

One possibility is to consider encounters with very light PBHs, which are poorly constrained. Instead of disrupting (or "softening") the binary with a heavy perturber, $m_3 \gg m_1, m_2$, one can consider tightening (or "hardening") the binary with a light perturber, $m_3 \ll m_1, m_2$. However, the transition between the hard and soft binary regimes is not well defined, and this leads to significant complications for light DM-like perturbers. According to numerical experiments by Hills [180], perturbers with a velocity larger than the orbital speed of the binary will tend to soften the binary, while slower perturbers will tend to harden it, irrespective of their masses. This disagrees with the earlier definition for the case of a fast, low-mass perturber, which is exactly the regime of interest for hardening by low-mass PBHs. Quinlan [174] suggests that a binary in a sea of low-mass perturbers must not be considered hard unless its orbital speed exceeds the perturber velocity dispersion by a factor that is proportional to

$(1 + m_1/m_2)^{1/2}$, where $m_1 \geq m_2$. This mass dependence corresponds to that of a critical velocity $w(m_1, m_2)$ for capture. Perturbers with velocity below w can be captured by the binary, altering the statistics of the outcomes of close encounters.

The cutoff imposed by the critical velocity is fatal to the prospect of observing hardening by light PBHs, as we explain in detail in appendix B. Briefly, the rate of hardening scales as $\mathrm{d}a/\mathrm{d}t \propto a^2$, so the hardening effect is only discernible at large binary separations, $a \gtrsim 10^5\,\mathrm{AU}$. Thus, one is immediately locked into binaries with very wide separations, where data is sparse and observational prospects are already challenging. But since the orbital velocity of the binary decreases with increasing separation, only a vanishingly small fraction of PBHs would have a velocity lower than the binary's orbital speed, unless we assume very cold DM systems.

Thus, the only interesting possibility that remains is exchange. We now consider the conditions needed for exchange to take place. An exchange requires that the three objects do not all escape to infinity after the encounter, which requires that the initial velocity of the PBH is small. This translates to another maximum velocity $v_{\max}$, different from w, below which exchange is possible. In the rest of this work, we follow Ref. [229] and set $v_{\max}$ to be the velocity at which the total energy of the three-body system is zero in the rest frame of their barycenter, i.e.,

$$v_{\max} = \sqrt{\frac{G m_1 m_2 m_{123}}{m_{12} m_3 a}}. \tag{4.2}$$

Thus, when computing the exchange cross section, we require that $v_{\mathrm{PBH}} < v_{\max}$. For the purposes of exchange, this is the condition for the binary to be hard with respect to the perturber. Quantitatively, this corresponds to the condition that

$$v_3 < v_{\max} = (30\,\mathrm{km/s}) \left(\frac{a}{1\,\mathrm{AU}}\right)^{-1/2} \left(\frac{\frac{m_1 m_2}{m_3} \frac{m_{123}}{m_{12}}}{\mathrm{M}_\odot}\right)^{1/2} . \tag{4.3}$$

For the case of a hard binary, we compute the exchange cross section Σ following Ref. [229], which gives

$$\begin{aligned}\Sigma(v_3) = 13.9\,\mathrm{AU}^2 \times \left(\frac{a}{1\,\mathrm{AU}}\right) \left(\frac{v_3}{10\,\mathrm{km/s}}\right)^{-2} \left(\frac{m_3}{m_{13}}\right)^{5/2} \\ \times \frac{m_3}{m_{12}} \frac{\left(m_{12}^4 m_{23} m_{123}\right)^{1/6}}{1\,\mathrm{M}_\odot} \exp\Big\{3.70 + 7.49\mu_1 - 1.89\mu_2 \\ - 15.49\mu_1^2 - 2.93\mu_1\mu_2 - 2.92\mu_2^2 + 3.07\mu_1^3 \\ + 13.15\mu_1^2\mu_2 - 5.23\mu_1\mu_2^2 + 3.12\mu_2^3\Big\}.\end{aligned} \tag{4.4}$$

This expression is a fit to numerical experiments conducted with $v_{\mathrm{PBH}} = 0.1 v_{\max}$. We assume the validity of this expression for all velocities $v < v_{\max}$, and also define the velocity-independent quantity $\Sigma_0 \equiv \Sigma \times v_3^2$. We take all binaries to be circular throughout this work.

Typically, the rate of exchanges will be dominated by the low-velocity tail of the PBH distribution. We take the PBH speed distribution to be that of Galactic DM, such that the Probability Density Function (PDF) is given by

$$\mathcal{F}_{\mathrm{DM}}(v_{\mathrm{PBH}}) = \sqrt{\frac{2}{\pi}} \frac{v_{\mathrm{PBH}}^2}{\sigma_{\mathrm{DM}}^3} \exp\left[-\frac{v_{\mathrm{PBH}}^2}{2\sigma_{\mathrm{DM}}^2}\right] . \tag{4.5}$$

The overall exchange rate per binary is then given by

$$\Gamma = n_{\rm PBH}^{v<v_{\rm max}} \langle \Sigma(v_3) v_3 \rangle = n_{\rm PBH} \int_0^{v_{\rm max}} \mathrm{d}v_3 \, \mathcal{F}_{\rm DM}(v_3) \Sigma(v_3) v_3, \tag{4.6}$$

where $n_{\rm PBH}$ is the total number density of PBHs, $n_{\rm PBH}^{v<v_{\rm max}}$ is the number density of PBHs with $v_{\rm PBH} < v_{\rm max}$, and $\langle\cdot\rangle$ denotes the average with respect to the distribution of PBH velocities $\mathcal{F}_{\rm DM}(v_3)$ subject to the restriction $v_3 < v_{\rm max}$. For $v_{\rm max} \ll \sigma_{\rm DM}$, we expand $\mathcal{F}_{\rm DM}$ to find

$$\Gamma \simeq n_{\rm PBH} \Sigma_0 \int_0^{v_{\rm max}} \mathrm{d}v_3 \sqrt{\frac{2}{\pi}} \frac{v_3}{\sigma_{\rm DM}^3} = \frac{n_{\rm PBH} \Sigma_0 v_{\rm max}^2}{\sqrt{2\pi} \sigma_{\rm DM}^3}. \tag{4.7}$$

In particular, since $\Sigma_0 \propto a$ and $v_{\rm max} \propto a^{-1/2}$, this implies that Γ is approximately independent of a. For fixed masses, this approximation breaks down at small separations, where $v_{\rm max}/\sigma_{\rm DM}$ becomes large. However, we will see that eq. (4.7) remains valid throughout most of the parameter space of interest in this work.

We show the exchange rate for a variety of different binary systems in fig. 4.2. We assume that PBHs account for a fraction $f_{\rm PBH} \leq 1$ of the DM density with a monochromatic mass distribution, and we show results corresponding both to $f_{\rm PBH} = 1$ (solid curves) and to $f_{\rm PBH}$ saturating observational constraints at each mass (dot-dashed curves). Note that each of these observational bounds has been contested, as summarized by Refs. [240, 10, 30, 154]. In particular, we omit the nominal constraint from the OGLE experiment, which has been interpreted to show a preference for a population of Earth-mass PBHs over the null hypothesis of $f_{\rm PBH} = 0$ [156]. (However, see Refs. [241,

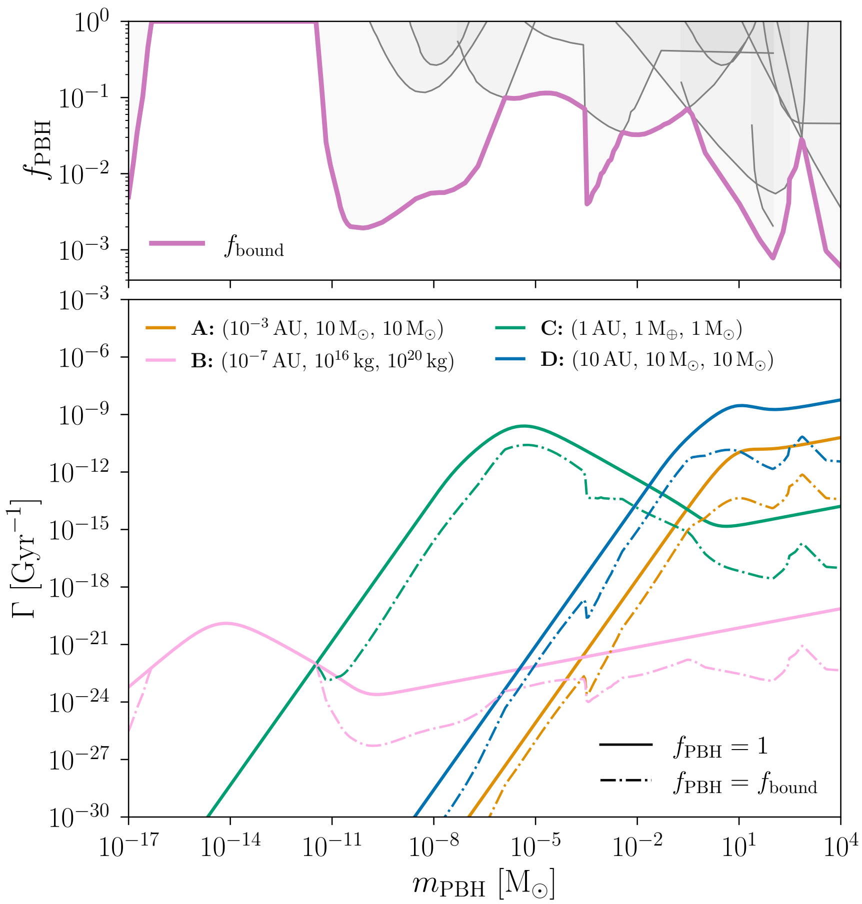

Figure 4.2: Bottom: exchange rate as a function of PBH mass for some typical binary systems. The DM dispersion is taken to be $\sigma_{\rm DM} = 220\,{\rm km/s}$, and binary parameters are given in the legend in the sequence (a, m_1, m_2). Curves A, B, C, and D are typical of close compact object binaries, asteroid binaries, exoplanetary systems, and stellar binaries, respectively. Solid curves assume that $f_{\rm PBH} = 1$, and dot-dashed lines take $f_{\rm PBH}$ to saturate observational constraints, i.e., $f_{\rm PBH} = f_{\rm bound}$. Top: observational constraints on $f_{\rm PBH}$ [230, 47, 231, 232, 233, 50, 234, 235, 156, 208, 236, 237, 238] taken from `https://github.com/bradkav/PBHbounds` [239]. The purple curve shows the maximum allowed value of $f_{\rm PBH}$ at each mass, $f_{\rm bound}$, assuming a monochromatic mass function.

242, 243].)

Figure 4.3 shows the exchange rate and its functional dependences for benchmark parameters typical of stellar binaries. As is clear from the figure, the rate generally peaks when $m_1 \simeq m_3$, i.e., when the mass of the PBH matches the mass of the object to be ejected. These curves in the left and center panels take the PBH velocity dispersion to be $\sigma_{\rm DM} = 220\,{\rm km/s}$, but per eq. (4.7), the rate is much higher in cold systems with smaller dispersions, as shown in the right panel. While one might expect the rate to decrease with m_2, the mass of the secondary, the opposite is true, as demonstrated in the center panel. Instead, increasing the mass of the secondary increases the gravitational focusing effect and enhances the effective cross-section for PBHs to scatter with the binary system.

Counterintuitively, the exchange rate also increases with the PBH mass, even while holding the PBH density constant. When $m_3 \gg m_1, m_2$, the critical velocity $v_{\rm max}$ becomes independent of m_3. Then all m_3 dependence in the cross section is confined to Σ_0, which goes as $\Sigma_0 \propto (m_3^4/m_{12})^{1/3}{\rm M}_\odot^{-1}$. Since $n_{\rm PBH} \propto m_3^{-1}$ at fixed abundance, the overall rate scales with $\Gamma \propto m_3^{1/3}$. When the PBH is much more massive than the binary, the kinetic energy of the PBH is large compared to the potential energy of the binary in the rest frame of the binary. This naively facilitates disruption. However, the typical velocity imparted to the binary components is set by $v_{\rm PBH} \ll v_{\rm max}$, and in the limit of a massive perturber, this implies that at most one object can escape to infinity. This is shown in detail in Sec. 3.1 of Ref. [229]. Thus, exchange is inevitable: after an encounter with significant energy transfer, one of the components of the original binary system is typically captured by the PBH, even if the other escapes. Thus, captures and

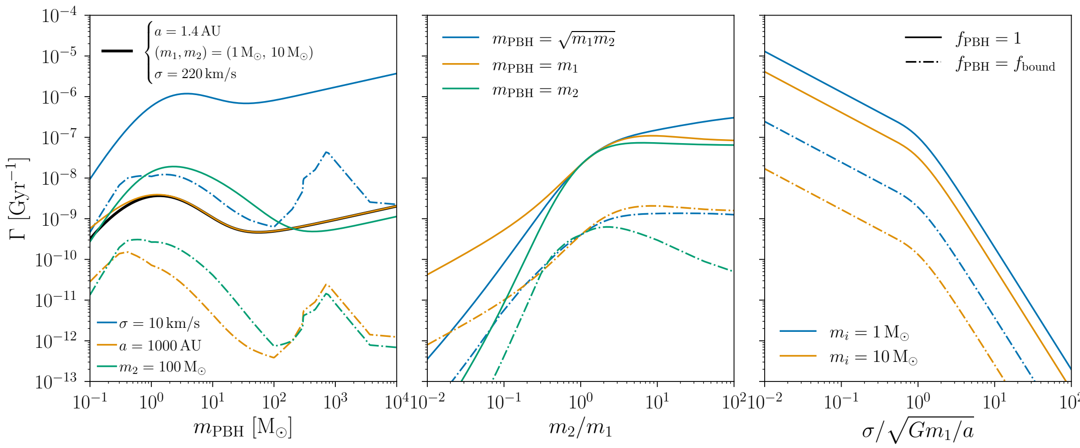

Figure 4.3: Exchange rate as a function of PBH mass for typical stellar binary systems. Solid curves assume that all of the DM is composed of PBHs, with a DM density of $0.4\,\mathrm{GeV/cm^3}$. Dot-dashed curves assume that f_{PBH} saturates observational bounds. (See fig. 4.2.) Left: exchange rate as a function of PBH mass. Center: exchange rate as a function of the mass ratio of the bound object to the ejected object. Note that the bound on the PBH abundance is dependent on the choice of m_{PBH}, meaning that the ordering of the dot-dashed curves can vary with m_2/m_1. Right: exchange rate as a function of the DM velocity dispersion in ratio to the orbital velocity scale of the binary, with all three objects taken to have equal mass.

exchanges dominate over disruption in this regime.

There is nothing nonphysical about the rate growing without bound as $m_3 \to \infty$: in this limit, the number of PBHs eventually shrinks to just one with the mass of the entire Galactic halo. Then all binaries of interest must immediately be bound to the PBH simply by virtue of being bound to the halo itself. However, at much lower masses, a more pragmatic cutoff is imposed by the radius of PBH, which exceeds $1\,\mathrm{AU}$ for $m_3 \gtrsim 5 \times 10^7\,\mathrm{M}_\odot$. When the radius of the PBH exceeds the separation of the binary system in question, it is no longer appropriate to treat the PBH as a point particle in Newtonian gravity. At any rate, since other dynamical constraints become severe at such large masses, we restrict our attention to $m_3 < 10^4\,\mathrm{M}_\odot$ in this work.

For all the binaries shown, the timescale for the exchange process is above the

Hubble time. However, given the number of binary systems in the Milky Way, it is still plausible that an exchange process has occurred in a large number of them. In the next section, we consider the specific types of binary systems that are best suited to undergo exchange with a PBH.

4.2 Candidate binary systems

The exchange process described in section 4.1 can take place across an enormously wide range of binary systems, with widely varying parameters. In particular, the separations span an enormous range: the widest observed stellar binaries have separations of order $10^5\,\mathrm{AU}$, while asteroid binaries can be as close as $10^{-8}\,\mathrm{AU}$, or just a few kilometers. The masses of binary components—and, of course, of hypothetical PBHs—span many orders of magnitude as well. In this section, we outline the classes of observable binary systems, and we briefly evaluate the extent to which each type of system might be amenable to exchanges with PBHs.

4.2.1 Compact object binaries

Compact object binaries are a very unusual class of objects for our present purposes: they inhabit unique regions of binary parameter space and also offer unique observable signatures. Binaries with at least one black hole component are most readily observed via gravitational waves from their mergers. In order to merge within a Hubble time, the binary must already be quite close, meaning that the maximum velocity $v_{\max}$ for the exchange process, given in eq. (4.3), is significantly increased. In particular, observed BH-BH binaries are thought to form from a common envelope phase, when both objects are enclosed within the radius of a single giant star, typically well below $1\,\mathrm{AU}$. This implies that there is very little suppression of the exchange rate from requiring hardness of the binary with respect to the perturber, and also renders our estimate in eq. (4.7) inadequate.

However, there are a number of inherent difficulties in studying a PBH population via exchanges in compact object binaries. Firstly, in such a system, it would likely be impossible to establish that the exchanged black hole had a primordial origin rather than an astrophysical origin. Since the exchange is maximal when the PBH mass is at least as large as the masses of the binary components, the best prospects for PBH exchange are at black hole masses that are already produced by stellar evolution. The BH spin parameter measured in gravitational waves from a merger could suggest a primordial origin, since PBHs are known to have negligible spins when formed in a radiation-dominated universe [244, 245, 246], but making such a statement robustly would require a large number of events.

Secondly, since the main observable signatures of compact object binaries arise from their mergers, it is necessary to consider the impact of the exchange process on the time to merger. Since binaries that will eventually merge must already be very hard, the other three-body processes have little impact on their evolution. But exchanges transfer a large amount of energy from the perturber to the ejected object, so the time to merger between the components of the new binary system can be significantly different from the time to merger of the original binary. As such, even given the exchange rate in these binaries, it is not trivial to estimate the observed merger rate of systems that have undergone an exchange with a PBH.

Still, the biggest challenge in using these systems to probe PBHs is that merger signatures are transient events. This means that in any given time period, the number of observable systems can be very small even if the total number of systems is large. In principle, gravitational wave observatories are sensitive to mergers at cosmological distances, encompassing a vast number of sources, but very few of these binaries will merge during the observing period.

Figure 4.2 indicates that the exchange rate per binary is at most $\mathcal{O}(10^{-20}\,\mathrm{yr}^{-1})$. Under the most optimistic circumstances, let us consider all mergers with redshifts $z < 1$ to be detectable. Certainly, some merger events are detectable at such distances—for example, the merger that produced the gravitational wave event GW190521 took place at an estimated redshift of $z \approx 0.8$ [247]. The Milky Way is estimated to contain $\mathcal{O}(10^6)$ BH binaries [248], and there are approximately 10^9 galaxies with $z < 1$ [249]. Assuming that all galaxies have as many BH binaries as the Milky Way leads to a significant overestimate of the population. If binaries merge immediately after exchanges, then the overall rate of mergers is still at most $10^{-5}\,\mathrm{yr}^{-1}$. Thus, it is extremely unlikely that the current generation of gravitational wave detectors would be capable of detecting any binaries that have undergone an exchange with a PBH. Even future facilities such as Cosmic Explorer or Einstein Telescope will not change this conclusion: the total number of galaxies in the observable Universe is no larger than $\mathcal{O}(10^{12})$ [249, 250], so the total rate of exchanges is well below $10^{-2}\,\mathrm{yr}^{-1}$.

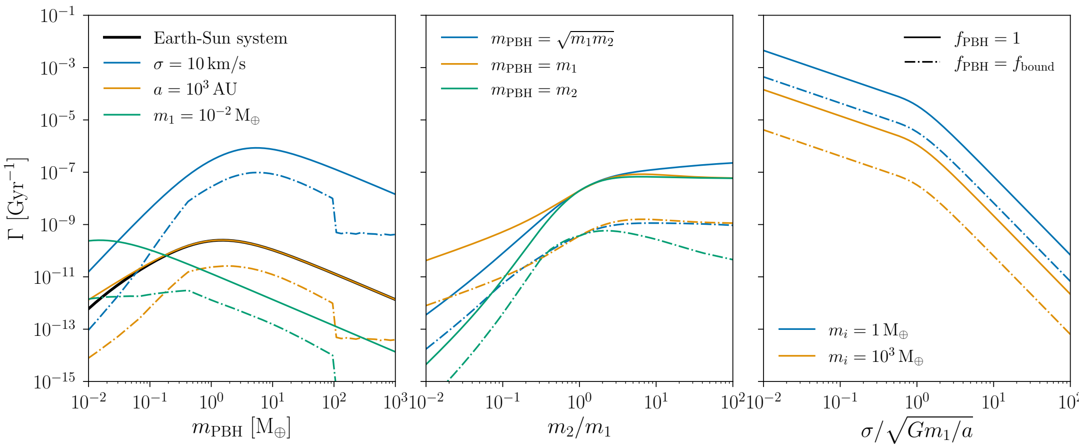

Figure 4.4: Exchange rate as a function of PBH mass for typical exoplanetary systems. Solid curves assume that all of the DM is composed of PBHs, with a DM density of $0.4\,\mathrm{GeV/cm^3}$. Dot-dashed curves assume that f_{PBH} saturates observational bounds. (See fig. 4.2.) Left: exchange rate as a function of PBH mass. Center: exchange rate as a function of the mass ratio of the bound object to the ejected object. Right: exchange rate as a function of the DM dispersion velocity in ratio to the orbital velocity scale of the binary, with all three objects taken to have equal mass.

4.2.2 Asteroid binaries

Asteroid binaries provide an interesting laboratory for dynamics on a unique set of scales, and observational measurements of their dynamics are accumulating rapidly. The list of observed asteroid binaries has expanded significantly in recent years, and now numbers 542: 98 near-Earth asteroids, 34 Mars-crossing asteroids, 262 main-belt asteroids, 8 Jupiter Trojan asteroids, and 140 trans-Neptunian objects [251, 252, 253, 254, 255]. The binary separations range from $\mathcal{O}(1)$ km to ultra-wide trans-Neptunian binaries, which can have separation $\mathcal{O}(10^5)\,\mathrm{km}$. The relative radius of the secondary component of the binary system compared to the primary component can range from 4–50% for near-Earth binaries to $\sim 100\%$ for trans-Neptunian binaries. In large asteroid binary systems, i.e., those in which one component has a radius exceeding $20\,\mathrm{km}$, the secondary-to-primary mass ratio can range from 10^{-6} to 10^{-2} [251].

The exchange rate for typical asteroid binary parameters is shown in case **B** of fig. 4.2. Here we take $m_1 = 10^{16}\,\mathrm{kg}$, $m_2 = 10^{20}\,\mathrm{kg}$, and $a = 10^{-7}\,\mathrm{AU}$ $(15\,\mathrm{km})$. The exchange rate peaks for $m_{\mathrm{PBH}} \simeq m_1$, attaining a value of $\mathcal{O}(10^{-20})\,\mathrm{Gyr}^{-1}$. Clearly, the exchange rate is much too small for such an event to have happened within the lifetime of the Solar System with any appreciable probability. That said, the rate is most enhanced for wide binaries with large mass ratios between the primary and secondary partner.

Setting aside the minuscule rate, the observability of an asteroid-PBH binary poses an interesting challenge. Advances in observational techniques, including radar, direct imaging, advanced lightcurve analysis, spacecraft imaging, and adaptive optics on large telescopes, have enabled the identification of large numbers of binary systems in recent years [256, 257, 258]. Lightcurve analysis, relevant for nonsynchronous eclipsing binaries, is likely to be ineffective, given the small radius of the PBH. Direct imaging is already difficult for binaries given the extremely small angular resolution required to distinguish partners separated by fractions of an arcsecond. For a PBH partner, this method becomes even more difficult. In principle, astrometric perturbations of the primary component due to the presence of a dark secondary may provide an avenue for detection in the future.

In the particular case of PBH exchange in the Solar System asteroid belt, Hawking radiation provides a reliable means of detection for light PBHs with $m_{\mathrm{PBH}} \simeq 10^{14.5}\,\mathrm{g}$, whose lifetimes are comparable to the age of the Universe. For a Schwarzschild BH, neglecting greybody factors, the luminosity of Hawking radiation is given by

$L_{\rm PBH} = \sigma/(16\pi^{3/2}Gm_{\rm PBH})^2$, where σ is the Stefan-Boltzmann constant. (Here we use natural units with $c = \hbar = k_{\rm B} = 1$.) Since the radiation is emitted with a blackbody spectrum, the typical energy of radiated photons is of order the temperature, $T_{\rm PBH} = (8\pi G m_{\rm PBH})^{-1}$, in the geometrical optics approximation. Accordingly, the flux of photons per unit area at a distance d is estimated by $\Phi_\gamma \simeq L/(4\pi d^2 T_{\rm PBH})$, or

$$\Phi_\gamma \simeq 20\,000\,\mathrm{m}^{-2}\,\mathrm{yr}^{-1}\left(\frac{m_{\rm PBH}}{10^{14.5}\,\mathrm{g}}\right)^{-1}\left(\frac{d}{2\,\mathrm{AU}}\right)^{-2}. \tag{4.8}$$

These photons would have a typical energy of $E_\gamma \sim T_{\rm PBH} \approx (30\,\mathrm{MeV})\times[m_{\rm PBH}/(10^{14.5}\,\mathrm{g})]^{-1}$. This estimate suggests that space-based MeV telescopes should be sensitive to the presence of such an object in the asteroid belt.

In particular, the upcoming AMEGO-X telescope [259] has an effective area of $400\,\mathrm{cm}^2$, corresponding to a signal rate of about $700\,\mathrm{yr}^{-1}$. Given the angular resolution of $2.5°$ and the energy resolution of $\mathcal{O}(10\%)$, the expected background rate at the spectral peak in each angular patch is $\mathcal{O}(10^5\,\mathrm{yr}^{-1})$. Furthermore, this signal would exhibit a strong modulation over the period of the distance between Earth and the binary, enabling strong background rejection. As such, we expect that AMEGO-X could conclusively detect any PBH in the asteroid belt with a mass of order $10^{14.5}\,\mathrm{g}$ within a few years.

A more refined estimate can be performed by including greybody factors using the `BlackHawk` code [260, 261]. For a Schwarzschild BH with a mass of $10^{14.5}\,\mathrm{g}$, the photon spectrum peaks at $190\,\mathrm{MeV}$. Considering a wide energy bin of $[140,\ 240]\,\mathrm{MeV}$, this yields a signal rate of $130\,\mathrm{yr}^{-1}$ against a background rate of $9000\,\mathrm{yr}^{-1}$. This signal can be detected with 95% confidence after two years of observation, even neglecting modulation. For PBHs with significant angular momentum [262, 263, 264], the emission rate is enhanced at high energies, where the expected background rate is reduced. For a Kerr PBH with a dimensionless spin parameter $a_* = 0.9999$ and a mass $m_{\rm PBH} = 10^{15}\,\rm g$, the photon spectrum peaks at $115\,\rm MeV$. In the bin $[80,\ 130]\,\rm MeV$, the background rate is $4 \times 10^4\,\rm yr^{-1}$, while the signal rate increases to $2000\,\rm yr^{-1}$. This high signal rate allows for the detection of PBH at the 95% confidence level with about 15 days of observation. In principle, γ-ray signals might also be observed from PBHs transiting through the Solar System or captured via three-body processes without ejection. However, in these cases, the signal is transient. A transiting PBH is only detectable when in proximity to Earth, and a PBH captured into a triple system by three-body dynamics has a metastable orbit and will eventually be ejected. (See e.g. Ref. [179].) A PBH captured into a stable orbit by ejection of a third body can remain observable for the lifetime of the Solar System, making exchanges observable now even if they occur only once in the history of the system. For a more comprehensive discussion of the observability of Hawking radiation from within the Solar System, see Ref. [265].

4.2.3 Exoplanetary systems

Exoplanetary systems are abundant, closely observed, and extremely well modeled. As such, it is interesting to consider the prospects for detecting exchanged PBHs in this context. If such a process were to occur in an exoplanetary system, the system would host a PBH "planet," possibly in addition to other ordinary planets. The case for detecting PBHs in exoplanetary systems is ultimately similar to that in our own Solar

System. Several authors have examined the possibility of PBH capture by one of our own planets [164], or by other means [266, 267]. The relative utility of exoplanetary systems over the Solar System is twofold: first, they are numerous, widening our opportunity to find such an object; and second, the parameters of planets and their orbits span a range of values different from those in our own Solar System, possibly offering better sensitivity to certain PBH masses.

Exoplanetary systems are studied by a combination of data from Doppler spectrographs (the radial velocity method), astrometric measurements, transits, and direct imaging. Different methods have complementary strengths, and combinations of methods can yield more powerful results than any single measurement. Astrometric measurements can reveal all the orbital properties of the exoplanet as well as its mass, but even with the levels of precision achieved by *Gaia*, these measurements achieve only modest signal-to-noise ratios (~ 10) and can only probe giant planets [268, 269]. On the other hand, radial velocity data can yield much larger signal-to-noise ratios for giant planets, but only gives a lower limit to the exoplanet mass. Joint fitting of Doppler data and *Gaia* astrometric data has been shown to tightly constrain the exoplanet mass [269, 270] and diagnose false positives such as brown dwarf companions [271, 272].

Currently, *Gaia* provides astrometric information for 73 confirmed exoplanets and candidates, of which nine have already been confirmed with Doppler data. Simulations indicate that analysis of astrometric wobble of host stars will enable *Gaia* to discover between 10^4 and 10^5 exoplanets in the future [273]. A different combination of methods to detect exoplanets is Doppler data with transits. The NASA Exoplanet Archive hosts a total of 5690 exoplanets, of which 4262 have been discovered by transits, 1092 by radial velocity, and 838 by a combination of these two techniques.

The astrometric signatures of a PBH "exoplanet" would be identical to those of an actual planet, but a PBH of planetary mass would have an extremely small geometric cross section, and thus would not affect the lightcurve at all during a stellar transit [274]. As such, the observable effect of the presence of PBHs in exoplanetary systems would be the presence of astrometric or Doppler signatures without corresponding transit signatures. If the orbital period and phase are accurately determined through Doppler measurements, and the inclination angle is obtained from astrometric measurements, it is possible to predict the time of transit for a specific exoplanetary system. A missed transit would then indicate the presence of a PBH exoplanet. However, due to the uncertainty in measuring the orbital inclination of known exoplanetary systems, making precise transit predictions is challenging at this time. If a large fraction of exoplanets were actually PBHs, the rate of transits would be suppressed relative to the expectation from the rate of astrometric detections, providing a statistical hint for the presence of PBH exoplanets.

Thus, such a detection would only be possible if PBH planets were abundant. However, the rate of exchanges is too small for this to be realistically observable in our case. Even under the most generous assumptions, the exchange rate per binary is of order $10^{-6}\,\mathrm{Gyr}^{-1}$, as shown in fig. 4.4. This would translate to at most $\mathcal{O}(1)$ PBH planet in the entire sample of exoplanets expected to be discovered in the foreseeable future. Interestingly, our computation does suggest that if planet-mass PBHs account for a large fraction of the DM, then there likely are systems with PBH planets in the Milky Way, even under pessimistic assumptions. However, since we will only be able to characterize a small fraction of these systems, a robust detection of PBHs by this method is likely impossible.

4.2.4 Stellar binaries

Stellar binaries are perhaps the most well-studied population of binary systems. They are abundant and readily observable. We show exchange rates for typical stellar binary systems in fig. 4.3. The overall rate is only slightly higher than that in the exoplanetary case, as can be seen clearly in fig. 4.2. However, the large number of detectable stellar binaries offers a distinct set of observational opportunities.

An analysis of *Gaia* eDR3 [275] reveals 1.2 million high-confidence binaries within $1\,\mathrm{kpc}$ of the sun with $\Pi/\sigma_\Pi > 5$ for both components, where Π and σ_Π denote the parallax and its uncertainty. Most of these are main sequence–main sequence (MS-MS) binaries with separations between a few AU and $\mathcal{O}(10^6\,\mathrm{AU})$ [276]. A larger dataset with 1.8 million candidates becomes dominated by chance alignments at large separations. The techniques used to identify binary systems include (i) analysis of light curves ($a \lesssim 0.1\,\mathrm{AU}$); (ii) single- and double-lined radial velocities from the radial velocity spectrometer ($a \lesssim$ few AU); (iii) astrometric perturbations such as excess astrometric noise, proper motion anomaly, or astrometric orbits ($a \lesssim 10\,\mathrm{AU}$); and (iv) direct spatial resolution ($a \gtrsim 100\,\mathrm{AU}$).

The identification of a BH partner in a *Gaia* binary system is a non-trivial question, and we mainly summarize the results given by Ref. [213]. The most optimistic methods rely on astrometric perturbations. Indeed, the first BHs discovered by *Gaia* have been validated in this manner [277, 278, 279]. Astrometric wobble has a non-trivial dependence on the mass and luminosity ratios of the binary components. Since the BH component is dark, the photocenter traces the luminous component. The predicted angular photocenter semimajor axis for the binary is given by $a_\phi = q\Pi(a/\mathrm{AU})$ for $q \ll 1$ and $a_\phi = \Pi(a/\mathrm{AU})$ for $q \gg 1$, where q is the mass ratio of the BH to the star. For a luminous companion, these relations are scaled by the light ratio: $a_\phi = \delta_{q\ell}\Pi(a/\mathrm{AU})$, where $\delta_{q\ell} = |q-\ell|/[(q+\ell)(\ell+1)]$ with ℓ being the secondary-to-primary light ratio. Detection of a BH component requires a_ϕ to be greater than the typical observation precision σ_ξ in the along-scan direction for a given apparent magnitude.

In the aftermath of the discovery of a dark companion, the question of whether it is an astrophysical BH or a PBH becomes relevant. Binaries comprising a Solar-mass star and a sub-Solar-mass dark companion (which could plausibly be an astrophysical compact object, planet, or PBH) are difficult to observe, as discussed in section 4.2.3. However, *Gaia* has already detected several binaries with a more massive dark companion [277, 279]. In systems such as these, the dark companion can only be identified as a PBH if the properties of the binary are sufficiently anomalous to call standard astrophysical origins into question. Properties anomalous to such an origin could pertain, for example, to the mass ratio, separation, and composition being incompatible with standard isolated binary evolution models. We take up this analysis for the *Gaia* binaries in greater detail in the following section.

4.3 Exchange scenario for *Gaia* binaries

Gaia has in fact detected several binary systems with a BH component, denoted by *Gaia* BH1, BH2, and BH3 [277, 280, 279]. Interestingly, the properties of these binaries pose a challenge to the standard astrophysical formation channels. In this section, we pose the question of whether these binaries might have been formed by exchanges with PBHs. There are two stages to this discussion. Firstly, for a given BH-stellar binary, how likely is it that its origin is from an isolated binary system, versus a dynamical mechanism such as exchange? Secondly, if dynamical exchange is favored, how likely is it that the exchange was with an astrophysical BH versus a PBH? We discuss these issues in the context of the concrete examples of *Gaia* BH1–BH3, first summarizing the relevant features of these binaries.

Gaia BH1 [277, 280] is a binary system with a G-type main sequence star with mass $M_1 = 0.93 \pm 0.05\,\mathrm{M}_\odot$ orbiting a BH of mass $M_2 = 9.62 \pm 0.18\,\mathrm{M}_\odot$, first identified astrometrically and then validated spectroscopically. The luminous component is a bright Solar-type star with $G = 13.77$ and metallicity $[\mathrm{Fe/H}] = -0.20 \pm 0.05$. The semimajor axis of the binary is $a = 1.40 \pm 0.01\,\mathrm{AU}$ with eccentricity $e = 0.451 \pm 0.005$. (We quote the central values obtained by a combination of astrometry and radial velocity.) The age of the luminous partner is at least $4\,\mathrm{Gyr}$. The luminous G star exhibits an abundance pattern typical of the thin disk: for all measured elements X, the abundance ratios $[\mathrm{X/Fe}]$ are within 2σ of the central value for stars in the Solar neighborhood [281]. This fact, combined with the fact that the luminous star is expected to have a thin convective envelope, implies that it suffered little contamination from its partner during their possible coevolution. There is also no evidence for the contamination of the photosphere by α-elements from the partner's death, or enrichment of s- and r-process elements. Thus, the luminous component of the binary evinces almost no evidence of a prior stage of interaction with its companion, even during the latter's putative death [277].

In combination, the composition of the luminous component, the mass M_2 of the BH, and the mutual separation of the components make it difficult to explain *Gaia* BH1 via the evolution of an isolated stellar binary. The reasoning is as follows. The BH mass, $M_2 \approx 10\,\mathrm{M}_\odot$, implies that the stellar progenitor had a mass 30–$50\,\mathrm{M}_\odot$, assuming Solar metallicity [282], since progenitors in that range can produce $\geq 9\,\mathrm{M}_\odot$ He cores. A progenitor of that size would have reached a radius of $\sim$$10\,\mathrm{AU}$ during its supergiant phase. Given the much smaller semimajor axis, $a \approx 1.4\,\mathrm{AU}$, this suggests that the progenitor of the BH would have interacted with the luminous G star in a common envelope phase. However, with the extreme mass ratio, the smaller star would not be expected to survive such a phase [283]. Even allowing for the survival of the G star, the final separation following a common envelope phase would have been much smaller, $\sim$$0.02\,\mathrm{AU}$. This conclusion persists for various combinations of Zero Age Main Sequence (ZAMS) properties, different models of the common envelope phase, and assumptions about the natal kick during the formation of the BH [277].

At present, therefore, the origin of *Gaia* BH1 remains uncertain, with several options on the table. One possibility is that the binary was originally much more widely separated and was significantly hardened by dynamical encounters after the formation of the BH component. Alternatively, the binary may have formed in a hierarchical triple or other three-body system. A third possibility is a dynamical exchange process of the type described in this paper: in this scenario, one of the components was not originally part of the binary and underwent an exchange with the original partner. If dynamical exchange is favored, the next question is whether the substituted partner had an astrophysical or primordial origin. This requires an examination of the trajectory of *Gaia* BH1. The orbit of *Gaia* BH1 is typical of a thin-disk star, never coming close to the Galactic Center, and limited to within $\pm 250\,\mathrm{pc}$ of the disk mid-plane. Given that exchanges with astrophysical BHs are much more probable in globular clusters, the possibility that the BH1 system formed through a dynamical process with an astrophysical BH is difficult to realize [284]. That said, simulation results from Ref. [284] conclude that BH1-like systems could have formed from repeated dynamical exchanges and collisions involving the progenitor star in young star clusters. *Gaia* BH1 is similar in orbital period and mass ratio to NGC 3201 #12560, which is located in the globular cluster NGC 3201, and for which a history of dynamical interactions (including exchange) with astrophysical BHs is much more plausible.

Gaia BH1 therefore provides a typical example where processes of the kind described in our work may be fruitfully investigated. *Gaia* BH2 furnishes a similar example. (See Ref. [285], however, for a different viewpoint.) In both systems, the binary separation is small enough, and the BH is massive enough that the binary components should have experienced a common envelope phase. However, such a phase would have resulted in much smaller separations than actually observed. Moreover, the luminous partner shows no evidence of interacting with its companion. Isolated binary evolution is disfavored, and the binary orbit poses challenges to standard dynamical processes in astrophysical BH-rich environments as well.

Gaia BH3 is an astrometric binary whose components are a $0.8\,\mathrm{M}_\odot$ star and a $33\,\mathrm{M}_\odot$ dark companion, with semimajor axis $a \approx 16.5\,\mathrm{AU}$ and eccentricity $e \approx 0.73$. It presents a similar conundrum with respect to its origin as do BH1 and BH2 [279]. Its radius during a putative supergiant phase would have reached $1800\,\mathrm{R}_\odot \approx 8.4\,\mathrm{AU}$, larger than the $4.5\,\mathrm{AU}$ separation at periastron. Indeed, *Gaia* BH3 presents a limiting separation beyond which evolution from a stellar binary without resorting to dynamical exchange processes becomes clearly feasible, since the BH-star system can avoid a common envelope. The *Gaia* Collaboration has forwarded dynamical exchange as a leading alternative hypothesis for the origin of BH3 [278]. One point of difference for *Gaia* BH3 compared to BH1 is that for the former, the metallicity is much lower than that of typical stars in the Solar neighborhood. *Gaia* BH3 is part of the ED-2 stellar stream, and dynamical formation in the cluster that formed ED-2 has been explored by several groups [286, 287].

We now turn to a discussion of the possibility that an observed star-BH binary system was formed through the dynamical exchange of a star-star binary with a PBH at some stage in its history. A careful analysis would involve the following steps: for a given set of binaries, the first set of selection criteria should, of course, be those that disfavor evolution from a single isolated binary. Separations, mass ratios, and compositions of the type shown by BH1–BH3 would furnish typical parameter ranges. The second set of selection criteria should maximize the probability that the binary underwent an exchange with a PBH at some stage of its history. A detailed analysis along these lines is left for the future. In the present work, we instead present a set of plausibility arguments that PBH exchange can form star-BH binaries at a non-negligible rate.

Our plausibility argument hinges on comparing two quantities: (i) the net formation rate $R_\star$ of binaries that form via a given channel (e.g., dynamical or isolated evolution) assuming the population of BHs is purely astrophysical, and (ii) the formation rate $R_{\rm PBH}$ due to exchanges with PBHs. In the context of dynamical formation, $R_\star$ is typically computed in stellar clusters as the number of binaries that form over the cluster's lifetime in ratio to its initial mass $M_{\rm cl}$. Given a formation rate per binary of $\Gamma_\star$, and assuming that the lifetime of the cluster is longer than that of a typical binary, $\tau_{\rm bin}$, we can estimate

$$R_\star^{\rm (ch)} \simeq \frac{\Gamma_\star^{\rm (ch)} \times \tau_{\rm bin} \times N_{\rm bin}}{M_{\rm cl}}, \tag{4.9}$$

where $N_{\rm bin}$ is the number of binaries in the cluster that can evolve to have a BH component, and (ch) denotes the formation channel in question. Since $M_{\rm cl}/N_{\rm bin}$ is on the order of the average stellar mass, $\langle M_\star \rangle$, this rate can be estimated by $R_\star^{\rm (ch)} \simeq \Gamma_\star^{\rm (ch)} \tau_{\rm bin}/\langle M_\star \rangle$. Taking $\langle M_\star \rangle \sim 1\,{\rm M}_\odot$, the equivalent rate for PBH exchange can then be roughly estimated by $R_{\rm PBH} \simeq \Gamma_{\rm PBH} \tau_{\rm bin} \times {\rm M}_\odot^{-1}$, where $\Gamma_{\rm PBH}$ is the PBH exchange rate per binary.

If these two quantities are of the same order of magnitude, then it becomes plausible that exchanges with PBHs could compare favorably with the probability of a given formation mechanism, specifically, for example, dynamical mechanisms. Of course, this does not settle the question of whether it was a PBH versus an astrophysical BH that was part of the dynamics in a given binary sample—to settle that question, a detailed study of binary orbits and stellar composition would be required to assess whether a binary passed through PBH-rich environments that were also poor in astrophysical BHs. Such an evaluation is left for future work.

Regardless of the formation mechanism, the overall rate of binary formation, R, can estimated observationally. Given the existence of *Gaia* BH1, Ref. [277] estimates that a fraction $f \sim 4 \times 10^{-7}$ of all low-mass stars should have a BH companion [277]. This figure is obtained based on *Gaia* DR3 data, after fitting orbital solutions and implementing stringent cuts: $\Pi/\sigma_\Pi > 20000/P_{\rm orb}$ and $a_\phi/\sigma_{a_\phi} > 158/\sqrt{P_{\rm orb}}$, where $P_{\rm orb}$ is expressed in days. If *Gaia* BH1 is taken as a prototypical binary that favors dynamical formation, then this value of f would serve as a proxy for the fraction of all binaries formed in that manner. Then, since stars in the cluster have masses of $\mathcal{O}(1\,{\rm M}_\odot)$, we have $f \sim R \times {\rm M}_\odot$ at the order-of-magnitude level, which in turn suggests $R \sim 10^{-7}\,{\rm M}_\odot^{-1}$. While this estimation of f from [277] is based on an analysis of observational data, a similar value, $R_\star^{\rm dyn} = 2.7 \times 10^{-7}\,{\rm M}_\odot^{-1}$, is found by Ref. [285] from simulations of cluster models utilizing the N-body integration code `NBODY7`. Moreover, Ref. [284] uses simulations of BH1-like binaries in low-mass and high-mass clusters at Solar metallicity, obtaining benchmark values of $R_\star^{\rm dyn} = 2.09 \times 10^{-7}\,{\rm M}_\odot^{-1}$ and $2.08 \times 10^{-7}\,{\rm M}_\odot^{-1}$, respectively.

Although isolated binary evolution is disfavored, values of f for *Gaia* BH-like binaries have also been obtained for such a formation channel. The authors of Ref. [285] find $R_\star^{\rm iso} \sim 10^{-10}\,{\rm M}_\odot^{-1}$ for simulations of *Gaia* BH1 and BH2-like binaries originating via isolated binary evolution using the `StarTrack` population synthesis code, although $R_\star^{\rm iso} \sim 10^{-7}\,{\rm M}_\odot^{-1}$ can be realized if the cuts were made less stringent. Similarly, isolated binary evolution of *Gaia* BH3-like binaries has been studied and the associated rate has been found to be $R_\star^{\rm iso} = 4 \times 10^{-8}\,{\rm M}_\odot^{-1}$ in old ($> 10\,{\rm Gyr}$) and metal-poor ($Z < 0.01$) populations [288]. We therefore arrive at the following estimates of R for *Gaia*-like BHs:

$$\begin{cases} R_\star^{\rm dyn} \sim 10^{-7}\,{\rm M}_\odot^{-1} & \text{(dynamical formation)}, \\ R_\star^{\rm iso} \sim 10^{-10}\text{–}10^{-8}\,{\rm M}_\odot^{-1} & \text{(isolated binary evolution)}. \end{cases} \tag{4.10}$$

We now turn to an estimate of the binary formation rate by PBH exchange, i.e., $R_{\rm PBH}$. In the left panel of fig. 4.3, we display the exchange rate as a function of the PBH mass. *Gaia* BH1 benchmarks are shown with the black solid line: binary component masses are $1\,{\rm M}_\odot$ and $10\,{\rm M}_\odot$ with separation $1.4\,{\rm AU}$, and the velocity dispersion is $\sigma_{\rm DM} = 220\,{\rm km\,s^{-1}}$. Other colors show different possible choices of separations, masses, and velocity dispersions. The exchange rate increases with increasing PBH mass, reaching a maximum for $m_{\rm PBH} = 1\,{\rm M}_\odot$. The rate then drops before increasing further with larger PBH mass. Neglecting bounds on the PBH abundance, the maximum exchange probability for BH1-like parameters is $\Gamma_{\rm PBH} \approx 4 \times 10^{-9}\,{\rm Gyr}^{-1}$. For $\tau_{\rm bin} = 4.0\,{\rm Gyr}$, we therefore obtain $R_{\rm PBH} \sim \mathcal{O}({\rm few}) \times 10^{-8}\,{\rm M}_\odot^{-1}$. When accounting for observational bounds on the PBH abundance, in their most restrictive forms, this drops to $\mathcal{O}({\rm few}) \times 10^{-10}\,{\rm M}_\odot^{-1}$. However, the constraints we quote in this mass range have been repeatedly disputed (see e.g. Refs. [159, 289, 290, 291, 292]), meaning that this additional penalty in the rate may not apply.

However, as with astrophysical formation channels, these estimates can be significantly enhanced in stellar clusters with low velocity dispersions. For example, while globular clusters have low mass-to-light ratios, their bound DM density may still dominate over the Milky Way halo density [293, 294, 295, 296]. In such systems, the dispersion is of order $10\,\mathrm{km/s}$, corresponding to the blue curve in fig. 4.3. Thus, even without accounting for any DM overdensity, the exchange rate in such systems could be as high as $\Gamma_{\mathrm{PBH}} \sim 10^{-6}\,\mathrm{Gyr}^{-1}$, corresponding to a formation rate of $R_{\mathrm{PBH}} \sim \mathcal{O}(\mathrm{few}) \times 10^{-6}\,\mathrm{M}_{\odot}^{-1}$. This rate is much larger than required to account for binaries like BH1. In fact, it is so large that PBHs could still account for BH1 even if they comprise only a small fraction of DM, as implied by the most restrictive observational constraints in this mass range. Furthermore, if PBHs account for a subcomponent of DM, they may be surrounded by a dense particle DM spike [297, 298, 299]. This has been shown to enhance the rate of stellar captures [300], and may similarly influence exchange processes.

The *Gaia* binaries BH1–BH3 themselves are not located in globular clusters, but rather likely formed in open clusters, with much lower densities. The DM density in open clusters is dynamically negligible, meaning that it must be much lower than the stellar density, but that does not preclude a bound DM component with a low velocity dispersion [301]. The low density would reduce our estimated R_{PBH}, possibly bringing it in line with observational estimates for the formation rate in open clusters. Ultimately, given the significant uncertainties in both observations and predictions, it remains plausible that BH1–BH3 and similar systems formed by dynamical exchange with PBHs, and that the BHs in these systems are primordial in origin.

4.4 Conclusions

In the preceding sections, we have considered one key question: can few-body dynamics probe a population of PBHs beyond softening and disruption? While hardening is possible in principle, the effect is negligible, as we demonstrate further in appendix B. PBH capture is also comparatively rare, since the resulting few-body systems are unstable to ejection. A survey of the possible outcomes of three-body encounters thus led us to study new observables associated with exchange processes, where a PBH replaces one component of a binary system. We now summarize the prospects for detecting or constraining such events.

One might hope that exchange would be viable at lighter masses than softening and disruption. The latter generally take place when PBHs are more massive than the components of the binary, which restricts their application to interesting parameter space at the planetary or asteroid mass scales. On the other hand, exchange can take place across a large range of masses and in an enormous variety of binary systems. We therefore evaluated the rate of exchange with PBHs in several different classes of systems, including compact-object binaries, asteroid binaries, exoplanetary systems, and stellar binaries. Each of these different types of systems most readily undergoes exchanges with a different range of PBH masses, and each presents different potential observables following an exchange.

Interestingly, our findings suggest that in some of the best-motivated PBH DM scenarios, exchange processes should give rise to a sparse but nonvanishing population of PBHs in binaries in the Milky Way, including, e.g., PBH "exoplanets." Moreover, for some classes of binaries, there are smoking-gun signatures of the presence of a PBH component. In particular, exchanges involving sub-Solar-mass PBHs in compact object binaries are in principle identifiable by their merger signatures, and exchanges of ultralight PBHs with asteroids in the Solar System would be observable via Hawking radiation. However, for most of these systems, we have shown that PBH exchange is unlikely to occur at a sufficient rate for any meaningful chance of observational detection.

There is one exception to this conclusion for the case of stellar binaries. Since so many of these objects are so well characterized, the low exchange rate is not an obstruction to the detection of bound PBHs. We argue that PBH exchanges in stellar binaries might be identified by the detection of binaries with BH components whose properties are otherwise difficult to explain by standard astrophysical mechanisms. Interestingly, this is exactly the case for the *Gaia* binaries BH1–BH3: these objects are not readily accounted for by isolated binary evolution, and a dynamical origin, quite probably including exchange, is favored. We have demonstrated that the PBH exchange rate is sufficient at the order of magnitude level to produce binaries of this type in the PBH DM scenario, particularly if constraints on PBHs in the Solar mass range are relaxed compared to their most restrictive forms.

Ultimately, in order to make any robust claim of primordial origin for a stellar companion, astrophysical formation channels must be confidently excluded, and the exchange rate must be evaluated with greater specificity. The astrophysical history of a particular binary can be understood to some extent by detailed modeling of its environment and trajectory. Likewise, for a given binary, the PBH exchange rate can be accurately calibrated with numerical experiments. Thus, it is plausible that binaries like *Gaia* BH1–BH3 will eventually furnish a detection of PBHs, not by virtue of the properties of the BHs themselves, but by virtue of the luminous objects dancing with these invisible partners.

Chapter 5

Exploring Dark Forces with Extreme Mass Ratio Inspirals

A wide range of physics scenarios beyond the Standard Model (SM) and General Relativity (GR) have as their template the following potential generated by an object of mass M:

$$U = -\frac{GM}{r}\left[1 + \tilde{\alpha}' e^{-\frac{r}{\lambda}}\right], \tag{5.1}$$

where the extra contribution to the Newtonian potential, sometimes dubbed a “fifth force” or “dark force” depending on the context, is controlled by an effective coupling strength parameter $\tilde{\alpha}'$ and a characteristic length scale λ. The Yukawa contribution can also be interpreted as the static limit of an interaction mediated by bosons of mass

$$m_V \sim \frac{1}{\lambda} . \tag{5.2}$$

This widely used framework has historically served to parametrize deviations from GR and the inverse square law [302, 303, 304], the effects of light string moduli [305, 306, 307, 308] and, in more recent times, as a template to study light mediators in dark sector models [309, 310, 311, 312, 313, 314]. Interpreted purely in terms of deviations from GR (i.e., without reference to dark sector physics), this formalism describes, for example, models of large extra dimensions (for small values of $\lambda \ll 10^{-3}$m) [315, 316] as well as braneworld [317, 318, 319], and the linearized regime of massive gravity theories (for large values of λ) [302]. In the study of dark sectors, on the other hand, $\tilde{\alpha}'$ takes on the role of the dark sector coupling and m_V the role of the dark mediator mass, while the Yukawa interaction is assumed to be sourced by the accumulation of dark charge on the central and secondary objects. Indeed, a host of interaction potentials (not just the Yukawa potential) are possible, depending on the nature of the mediator being exchanged (we refer to [320, 321] for a unified treatment of such exchange interactions, and [322, 323] for recent work along these lines). We will mainly restrict our attention to long-range Yukawa potentials in this work.

The phenomenological framework of Eq. (5.1) encapsulates a wide variety of theories. For the purposes of this work, it is useful to distinguish between (i) theories of modified gravity or fifth forces, which would apply to all bodies; and (ii) theories of dark sector physics, where Eq. (5.1) only applies to bodies with dark charge. While our main interest is in the second category, we briefly summarize the various systems that have been used to constrain fifth forces in general. The parametrization in Eq. (5.1) dictates the use of diverse experimental settings, where the characteristic scale of the probe should be $\lambda_{\rm probe} \sim \lambda$. The pursuit of probing λ through measurements at laboratory scales has a long history [324]. In the large λ (light mediator) regime, competitive bounds arise from planetary motion and the motion of stars around Sgr A* (we refer to [324] and [325] for comprehensive treatments of these two frontiers). The most stringent Solar System constraints on the $(\tilde{\alpha}', \lambda)$ plane come from modifications of Kepler's Third Law. On the other hand, broadly three avenues have been pursued with respect to constraints from Sgr A* [326]: (i) Orbital precession data by near infrared monitoring of stars that are sufficiently close to Sgr A*; (ii) high-precision timing of pulsars by existing and future radio telescopes; and (iii) space- and time-resolved probes of the accretion flow by the Event Horizon Telescope. The advent of gravitational wave (GW) astronomy has opened up new opportunities in this frontier (we refer to [202] for a recent review). It should be noted that many of the constraints on the $(\tilde{\alpha}', m_V)$ plane coming from GW data are obtained under the specific assumption that Eq. (5.1) depicts theories of massive gravitons (the constraints come from corrections to the propagation of GWs from the source binary to Earth, due to the non-zero graviton mass). For example, very strong constraints on m_V are obtained by a comparison of the times of arrival of GW and electromagnetic signals, or pure GW signals coming from sky-averaged, quasi-circular inspirals of compact objects of various masses (we refer to [327] for an early landmark paper in this area, and Table 2 of [202] for a summary of constraints). The use of GW propagation to constrain massive gravitons is *not* the focus of our work.

Compact object mergers in particular present unique opportunities: the population distributions and the GW waveforms emanating from these systems are sensitive to modifications of the type parametrized in Eq. (5.1). Different classes of compact binary systems enable different scales λ to be probed, depending on the characteristic frequency of the GW emission. The dark sector interpretation of Eq. (5.1), which is our main interest, works under the assumption that both the interacting objects accumulate dark charge. In the case of inspiraling neutron stars, such accumulation could result from dark matter capture; in the case of solar or supermassive black holes, such accumulation could result from spike formation, or from the fact that such black holes are charged under millicharged dark fermions [328]. Here, too, the recent literature is substantial, and we refer to [309, 310, 311, 312, 313] for some representative studies.

The purpose of this chapter is to explore the possibility of probing dark forces with extreme mass ratio inspiral (EMRI) systems consisting of a central object – the super-massive black hole (SMBH) – and a stellar mass black hole in a decaying orbit around the central object [329, 330]. These systems produce millions of cycles in the GW sensitivity band of LISA, enabling probes of the background geometry, as well as the detection of small changes to the radiation-reaction force. The inspiral process is driven mainly by the emission of gravitational radiation, thus providing an excellent laboratory in which to probe any altered emission due to dark forces. EMRI systems have been extensively used as laboratories of GR and modified gravity: we refer to [331, 332] for papers relevant to our study. Their use as probes of dark forces and dark sectors is somewhat more limited and recent: we refer to [331, 332] for scalar-mediated dark force studies, and [310] for somewhat related dark sector studies of SMBH binaries.

There are two main reasons why EMRIs should be studied in this context. The first is that the innermost stable circular orbit (ISCO) of the EMRI, which determines the characteristic length scale of the system and thus the characteristic wavelength of the mediator, probes a dark force range that is complementary to that probed by SMBH or neutron star binaries. Moreover, since the ISCO scales linearly with the mass of the central SMBH, different EMRI systems are sensitive to different dark force ranges corresponding to $\lambda \sim R_{\rm ISCO} \propto M_2$, where M_2 is the mass of the SMBH. In particular, we show our results for LISA [333, 334] (SMBH masses $\sim 10^6\, M_\odot$ with corresponding $\lambda \sim \mathcal{O}(10^{10})$ m and $m_V \sim \mathcal{O}(10^{-16})$ eV) and for the proposed μAres detector [335]

(SMBH masses $\sim 10^8\,M_\odot$ with corresponding $\lambda \sim \mathcal{O}(10^{12})$ m and $m_V \sim \mathcal{O}(10^{-18})$ eV).

The second reason EMRIs are interesting in this context is that mass measurements of the central SMBH, performed by methods that are independent of the primary EMRI system (a combination that we somewhat loosely call "multimessenger") can enable us to probe small values of the dark sector coupling. The main challenge in probing small couplings $\tilde{\alpha}'$ is that the correction in Eq. (5.1) is parametrically limited by the uncertainty in the binary component masses. A possible remedy that has been pursued by some authors [336] is to ascertain the masses of the binary components with post-Keplerian parameters such as advance rate of periastron and Shapiro time delay. However, this is predicated on the assumption that the dark sector contribution to the orbital decay proceeds through a dominant dipole term (while the contribution to other post-Keplerian parameters comes from corrections to the potential in Eq. (5.1)). Rephrased in terms of post-Newtonian counting, the dipole radiation correction to the orbital decay enters at -1PN order compared to GR, while the corrections to other post-Keplerian parameters enter at 0PN.

Independent mass measurements can break the degeneracy between gravity and the dark force, if the dark force is assumed to be subdominant or "switched off" between the SMBH and ordinary matter, while being operational between the SMBH and the black hole comprising the EMRI system. Stated in another way, the central SMBH is envisioned to have ordinary matter in its vicinity, which allows for the determination of the mass of the SMBH, without the confounding effect of the dark force. This knowledge of the mass of the SMBH can then be used to constrain the dark force using the EMRI between the SMBH and the stellar black hole. Although we will be somewhat agnostic to the underlying particle physics model that achieves this, we will indicate the most natural setting where our scenario may be applicable: a dark sector fermion χ with very feeble millicharge (near the weak gravity conjecture limit) interacting via an Abelian gauge boson V_μ.

Measuring the mass of SMBHs is a topic of intense research in astronomy. In quiescent galaxies, the methods typically rely on the motion of dynamical tracers – stars or gas – combined with sophisticated dynamical models. On the other hand, for active galaxies with prominent broad emission lines, the most promising method is reverberation mapping [337, 338, 339]. While measuring the motion of dynamical tracers requires high resolution and is applicable for nearer galaxies, reverberation mapping can be applied to galaxies at greater distances. We will also consider a third method that is applicable to nearby galaxies: GW signals from extremely large mass-ratio inspirals (XMRIs) formed by the central SMBH and a brown dwarf. We note that there are other emerging proposals for measuring the mass of SMBHs that we do not consider, such as X-ray flux variability of active galactic nuclei [340]. Our work motivates cross-pollination between the exciting field of SMBH mass determination and the future field of EMRI studies with future GW detectors, all within the context of dark sector physics.

The rest of the chapter is organized as follows. In Section 5.1, we discuss multimessenger measurements of the SMBH mass in different astrophysical systems. In Section 5.2, we show the dark force effect in the GW emission from EMRIs and the resulting sensitivity to the dark force with future LISA and μAres observations. We conclude in

Section 5.3.

5.1 EMRIs, Multimessenger Studies, and Ultralight Mediators

For ultralight mediators, the prospects of distinguishing the dark force from pure gravity is challenging. Compared to equal mass binaries, however, EMRIs offer certain advantages in addressing this important problem. The key point is the determination of the mass of the SMBH by a method for which the dark force can be switched off, followed by the determination of the mass of the mediator by an EMRI between the SMBH and a stellar black hole.

5.1.1 Multimessenger Studies with XMRI-EMRI Combinations

The combination of an extremely large mass-ratio inspiral (XMRI) and an EMRI with the same central SMBH but two different smaller objects (a brown dwarf for the XMRI [341, 342, 343] and a black hole for the EMRI) constitutes our first example of a multimessenger signal. XMRIs have been recently explored as interesting sources for LISA or TianQin. With mass ratios as small as $\sim 10^{-8}$, a brown dwarf would complete $\sim 10^{8}$ cycles before the merger, spending time on band for millions of years. These are expected to be abundant and loud systems: 10^4 (10^3) years before merger, the SNR is expected to be $\mathcal{O}(10^3)$ ($\mathcal{O}(10^4)$) [343]. It should be noted that the high SNR of XMRI systems implies that they can be detected in nearby galaxies as well ([343] calculates that XMRI systems with SNR $= 10$ can be detected out to 50 Mpc 200 yrs before plunge). It is instructive to consider the case of Sgr A*. XMRIs between Sgr A* and brown dwarfs can constrain the mass of Sgr A* at the level of $\mathcal{O}(10^{-2})M_\odot$ [342]. We will assume that the redshifted SMBH mass and the physical SMBH mass have the same level of uncertainty in this case. This is possible if the redshift is accurately determined, as expected for concurrent XMRI-EMRI events. For the event rate of eccentric XMRIs, [342] obtain an average of $N = 8^{+9}_{-3}$ for the case of low spin of Sgr A* ($a = 0.1$) and $N = 12^{+6}_{-4}$ for the case of high spin of Sgr A* ($a = 0.9$). The numbers quoted above signify sources that emit GWs in the LISA and TianQin detection band with SNR ~ 30. The brown dwarfs are assumed to have mass $0.05 M_\odot$ in prograde orbits and have an orbital inclination of 0.1 rad. The initial eccentricity of the XMRI system is taken to be between 0.99 and ≥ 0.999 with semimajor axis 4×10^{-4} pc $\leq\ a\ \leq 8 \times 10^{-3}$ pc. Similar numbers are reported by [343].

We now turn to a discussion of EMRI formation. Generally, the rate of EMRI formation in a galaxy is determined by two timescales. The first (the two-body relaxation timescale $T_{\rm rlx}$) is the time it takes to produce high eccentricity EMRI candidates from the dense cluster of stars and stellar remnants in the nuclear cluster surrounding the SMBH. The timescale $T_{\rm rlx}$ is determined by the number density of compact objects in the nuclear cluster, their velocity dispersion, steepness profile, and half mass radius [344]. The second timescale pertains to the time it takes for the EMRI candidate to decouple from the rest of the nuclear cluster, and is determined by the rate of GW emission. Typical estimates for the relaxation time are in the range of $\mathcal{O}(0.1 - 1)$ Gyr. Combining the estimates of these timescales, the benchmark figure for EMRI event rates from studies in the literature is $\sim 10^{-6}$ per galaxy per year. This translates to tens to hundreds of EMRI events per year at LISA, which probes the Universe out to redshift $z \sim 1$ [345]. It should be noted that the event rate for EMRIs is a subject of ongoing research, and the benchmark rate quoted above can be boosted by other mechanisms. While the $\sim 10^{-6}$ per galaxy per year is based on the "loss cone" scenario where a candidate is scattered by interactions with other bodies in the nucleus into a highly eccentric orbit around the SMBH, the presence of an accretion disk can significantly enhance this process. For example, [346] find that accretion disk-assisted EMRIs form $\sim \mathcal{O}(10^1 - 10^3)$ times faster than the "loss cone" mechanism.

The possibility of a concurrent observation of an XMRI-EMRI combination at Sgr A* is pessimistic: while the expected event rate of an XMRI is relatively high, the event rate of an EMRI is more suppressed, and the joint probability is further suppressed. Nevertheless, given that XMRI signals may be detected up to 50 Mpc, and EMRIs even further, the possibility of a coincident XMRI-EMRI signal may be significantly boosted if one considers other galaxies. Since such a concurrent multimessenger observation represents one of the best case scenarios for constraining ultralight mediators, we depict results corresponding to this benchmark scenario in our plots in Section 5.2.

5.1.2 Multimessenger Studies with Stellar Kinematics - EMRI Combinations

We now turn to another possibility: multimessenger combinations from stellar kinematics around SMBHs on the one hand, and EMRIs of stellar black holes on the other. While the precision of mass measurements using stellar orbits is far lower than that using the XMRI-EMRI combination, the event rate of such a possibility is more optimistic.

For the case of Sgr A*, the mass measurement by the GRAVITY Collaboration [347, 348, 349] relies on stellar orbits at several thousands of gravitational radii and yields a value of $M_2 = (4.297 \pm 0.012) \times 10^6\, M_\odot$. On the other hand, [350] provide six SMBH mass measurements at 3σ confidence level from SINFONI observations of nearby fast rotating early-type galaxies: NGC 584 ($M_2 = (1.3 \pm 0.5) \times 10^8\, M_\odot$), NGC 2784 ($M_2 = (1.0 \pm 0.6) \times 10^8\, M_\odot$), NGC 3640 ($M_2 = (7.7 \pm 5) \times 10^7\, M_\odot$), NGC 4570 ($M_2 = (6.8 \pm 2.0) \times 10^7\, M_\odot$), NGC 4281 ($M_2 = (5.4 \pm 0.8) \times 10^8\, M_\odot$) and NGC 7049 ($M_2 = (3.2 \pm 0.8) \times 10^8\, M_\odot$). Other SMBH mass measurements are also available: the MASSIVE Survey [351] is a volume-limited, multi-wavelength, integral-field spectroscopic and photometric survey of $\mathcal{O}(100)$ of the most massive early-type galaxies within 108 Mpc. A sample of 72 SMBHs and their host galaxies based on kinematic data and modeling efforts is provided in [352]. We note that the general level of the uncertainty in the mass measurement using stellar kinematics is $\sim \mathcal{O}(10-30)\%$. Thus, the observation of an EMRI between the SMBH and a stellar black hole in any of these galaxies would result in multimessenger combinations of stellar kinematics-EMRI.

5.1.3 Spectroscopic Reverberation Mapping and EMRIs

The third multimessenger combination scenario that we will consider is the measurement of the SMBH mass with spectroscopic reverberation mapping. In this method, the time delay in changes in the continuum emission arising from the accretion disk near the SMBH and the response of these changes on the emission from the (farther away) broad line region are measured. This time delay effectively measures the distance between the accretion disk and the broad line region (more precisely, the responsivity-weighted average radius of the broad line region). Finally, from this information, the mass of the

SMBH can be extracted following [353]:

$$M_2 = \frac{fc\tau_{\rm cent}\sigma_{\rm line}^2}{G} \ . \tag{5.3}$$

Here, $f \sim \mathcal{O}(1)$ is a parameter that is specific to the broad line region and depends on its structure, orientation, and kinematics. The parameter $\tau_{\rm cent}$ is the measured time delay (as measured from the centroid of the cross-correlation function around the emission peak), while $\sigma_{\rm line}$ denotes the root-mean-square width of emission in the variable part of the spectrum. A major source of uncertainty is the value of f. Mass measurements of SMBHs using this method can be obtained from the AGN Black Hole Mass Database [354]. Most of the measured SMBH masses lie at redshifts $z < 0.2$, although there are a few at $z \sim \mathcal{O}(2-3)$. The general level of uncertainty in the mass measurement is $\sim \mathcal{O}(10\%)$.

In this context, we take particular note of the OzDES and SDSS reverberation Mapping Programs [355, 339, 356], which have pioneered large-scale reverberation mapping campaigns [355]. These programs have observed hundreds of active galactic nuclei, probing a wide range luminosities and redshifts. The OzDES-RM program recently published data from successful campaigns for eight active galactic nuclei between $0.12 < z < 0.71$ [355]. In previous work, they measured the mass of two SMBHs at some of the highest redshifts, $z = 1.905$ and $z = 2.593$. The measured masses are $4.4^{+2.0}_{-1.9} \times 10^9 M_\odot$ for DES J0228-04 and $3.3^{+1.1}_{-1.2} \times 10^9 M_\odot$ for DES J0033-42, calculated with $f = 4.47 \pm 1.25$. The SDSS-RM Program published results for 849 broad-line quasars between $0.1 < z < 4.5$. The observation of an EMRI between the SMBH and a stellar black hole in any candidate observed by these campaigns would result in multimessenger combinations of reverberation mapping - EMRI, which constitutes our third benchmark scenario.

5.2 Results

In this section, we obtain constraints on the mediator mass versus coupling plane $(m_V, \tilde{\alpha}')$, assuming that the central SMBH and a second stellar black hole constitute an EMRI system. Our strategy will be to compute the temporal evolution of the angular frequency $\dot{\omega}$, including the correction due to the dark force in Eq. (5.1), and subsequently compute the GWs from perturbations of the Kerr metric following [357] (we refer to [358, 359] for classic papers and [360, 361] for earlier work). We will then compare our results to the case of pure gravity, where the dark force is absent. Our calculation most closely resembles that of [312], who performed an analogous calculation for regular equal-mass binary inspirals. We will assume an uncertainty of $\mathcal{O}(10)\%$ in the mass of the SMBH, corresponding to the case where the SMBH mass measurements comes from either stellar kinematics or reverberation mapping. On the other hand, for the case of an XMRI-EMRI multimessenger combination, we will assume that the mass of the SMBH is determined up to negligible fractional uncertainty $\sim \mathcal{O}(10^{-3})\%$.

We note that several prior studies of dark sectors with binary inspirals have concentrated on constraining either the strength of the dipole radiation term, or the charge of the remnant. For example, [362, 328, 363, 364, 312] consider black hole binary inspirals with massless mediators and constrain the dipole radiation term from the early pre-merger inspiral stage. The charge of the merger remnant can be constrained from the detection of the quasinormal modes. Dipole radiation in the context of EMRIs has been considered by [365, 366, 367]. Our focus, as stated before, will instead be on constraining the dark force in the limit of vanishing dipole radiation, relying instead on independent mass measurements of the SMBH.

The use of independent mass measurements to constrain dark forces works under the assumption that the dark force is only operational between the SMBH and the stellar black hole, while being switched off between the SMBH and surrounding baryonic matter, including stars, other objects such as brown dwarfs, and matter in the accretion disk. This is possible in models where the black holes are charged under a dark force acting only between particles in the dark sector, and not between the dark and visible sectors. We discuss a simple model that achieves this as a proof of principle, in Appendix C. The model consists of millicharged dark fermions with mass ~ 1 GeV and charge approximately equal to their mass, near the weak gravity conjecture limit. The dark force carrier is a vector V. The discharge time of a black hole initially charged with such dark fermions can be shown to be large under the most conservative assumptions. We remain somewhat agnostic about the question of how the black holes acquire their initial distribution of dark fermions, indicating some possibilities in Appendix C. For the case of the SMBH, the question reverts to the open question of how seeds of such black holes are formed.

5.2.1 Effect of Dark Forces

To set our notation, we consider an EMRI system consisting of two masses M_1 and M_2, with the mass ratio, $\eta \equiv M_1/M_2 \ll 1$. The heavy object ($M_2$) is an SMBH. In addition to the gravitational attraction between the two objects, we introduce a dark force operating between them. For simplicity, we consider a Yukawa force mediated by a mediator particle V

$$|\vec{F}_{\text{Yukawa}}| = \frac{\alpha' Q_1 Q_2}{r^2} e^{-m_V r}(1 + m_V r). \tag{5.4}$$

Here α' is the dark fine structure constant, m_V is the mass of the dark force mediator, r is the separation between the two objects constituting the EMRI system, and Q_i is the dark charge of the object i, with $i = 1, 2$. We will consider both the case when $\alpha' > 0$ (attractive force between charges of opposite signs) as well as $\alpha' < 0$ (repulsive force between charges of the same sign). For dark force mediated by a scalar particle, the force between two particles is always attractive. The modifications of the inverse-square law from attractive interactions mediated by a scalar mediator and a vector mediator are the same, and we will not distinguish them in the GW analysis. Although the Yukawa force is typically used to describe interactions mediator by scalar particles, we do not distinguish between scalar and vector mediators in this study when introducing dark forces in the form of Eq. (5.4). The dark force, together with the gravitational attraction, gives the total force acting on each object

$$|\vec{F}_{\text{total}}| = \frac{G M_1 M_2}{r^2}[1 + \tilde{\alpha}' e^{-m_V r}(1 + m_V r)], \tag{5.5}$$

where it is convenient to normalize the strength of the dark force to the gravitational force by introducing

$$\tilde{\alpha}' \equiv \frac{\alpha' Q_1 Q_2}{G M_1 M_2}. \tag{5.6}$$

The introduction of the dark force modifies the EMRI system in two ways. Firstly, the angular frequency $\omega(r)$ is determined by the net force on the lighter object, which is modified by the dark force, resulting in a departure from the inverse-square law as given in Eq. (5.5). Secondly, dark (dipole) radiation in the form of emission of the light force mediator will make the inspiral faster, affecting the temporal dependence of the separation $r(t)$. Both $\omega(t)$ and $r(t)$, and therefore ultimately the GW frequency $f_{\mathrm{GW}}(t)$ and strain $h_c(t)$ are modified from the pure gravity case in the presence of a dark force. In this work, we will assume that the dipole radiation is negligible.

Given a centripetal force in Eq. (5.5), the relation between the orbital frequency and the separation r in the presence of a dark force can be obtained as

$$\omega^2 = \frac{G(M_1 + M_2)}{r^3}(1 + \tilde{\alpha}' e^{-m_V r}(1 + m_V r)). \tag{5.7}$$

The GW frequency of a harmonic m is determined by the orbital angular frequency

$$f_{\mathrm{GW},m} = \frac{m}{2\pi}\,\omega. \tag{5.8}$$

Near the ISCO, GW radiation drives orbits to be circular; therefore the $m = 2$ mode dominates, and we focus on $f_{\mathrm{GW}} \equiv f_{\mathrm{GW},2}$ in the rest of the paper. We determine $r(\omega)$

numerically from Eq. (5.7). The EMRI loses energy mainly through GW radiation when dipole radiation of the mediator is turned off. The GW emission rate is

$$\frac{dE_{\rm GW}}{dt} = \frac{32}{5} G\,\mu^2\,\omega^6\,r^4. \tag{5.9}$$

Here, $\mu = M_1 M_2/(M_1 + M_2)$ is the reduced mass.

The time evolution of the orbital frequency due to GW radiation is [311]

$$\frac{d\omega}{dt} = -\frac{32}{5} G\,\mu\,\omega^5\,r^2\,g\,\mathcal{N}^{-1}. \tag{5.10}$$

The g factor is from the dark force correction to the gravitational attraction,

$$g = -\frac{3 + \tilde{\alpha}' e^{-m_V r}\left(3 + m_V r(3 + m_V r)\right)}{1 + \tilde{\alpha}' e^{-m_V r}\left(1 + m_V r(1 - m_V r)\right)}. \tag{5.11}$$

While a precise determination of the gravitational wave emission from the EMRI systems remains an ongoing effort, several sets of waveforms have been provided for data analysis. We adopt the result provided by Ref. [357], which was obtained by numerically solving the Teukolsky equation [358, 368] for quasi-circular orbit cases. The result for each physical quantity is presented as the usual equation, but with an additional factor added that captures the relativistic correction. In the case of GW frequency evolution in Eq. (5.10), we include the correction $\mathcal{N}^{-1}$ obtained from Table VIII of [357].

The strain amplitude of the GW signal can be calculated from the gravitational energy radiation rate. For the characteristic strain in the harmonic m, we follow the definition of [357],

$$h_{c,m} \equiv h_{o,m}\sqrt{2f_{\mathrm{GW},m}^2/\dot{f}_{\mathrm{GW},m}}\ , \tag{5.12}$$

with the dominant contribution coming from the harmonic $m = 2$. The $f_{\mathrm{GW}}^2/\dot{f}_{\mathrm{GW}}$ factor accounts for the time the GWs are produced at a fixed frequency for detection. The rms amplitude is defined as

$$h_{o,m} = \frac{2\sqrt{\dot{E}_{\infty m}}}{m\,\omega\,d_L}, \tag{5.13}$$

where $\dot{E}_{\infty m}$ is the total energy emission rate into the m-th harmonic to infinity. d_L is the luminosity distance from the EMRI system to Earth. The full expression for $h_{o,m}$ appears in Eq. (3.11b) of [357]. We reproduce the expression for the $m = 2$ mode here for completeness

$$h_{o,2} = \sqrt{\frac{32}{5}}\,\frac{\eta\,G\,M_2}{d_L}\,(G\,M_2\,\omega)^{2/3}\,\mathcal{H}_{o,2}. \tag{5.14}$$

The relativistic correction to the strain $\mathcal{H}_{o,2}$ can be obtained from the relativistic correction to the energy loss rate $\mathcal{H}_{o,2} = \sqrt{\dot{\mathcal{E}}_{\infty 2}}$, and we use numerical values of $\dot{\mathcal{E}}_{\infty 2}$ reported in Table IV of [357]. We will focus on the $m = 2$ harmonic of the characteristic strain amplitude $h_c \equiv h_{c,2}$, which is calculated through Eq. (5.12) with numerical results of $\dot{f}_{\mathrm{GW}}$ from Eq. (5.10) and $h_{o,2}$ from Eq. (5.14).

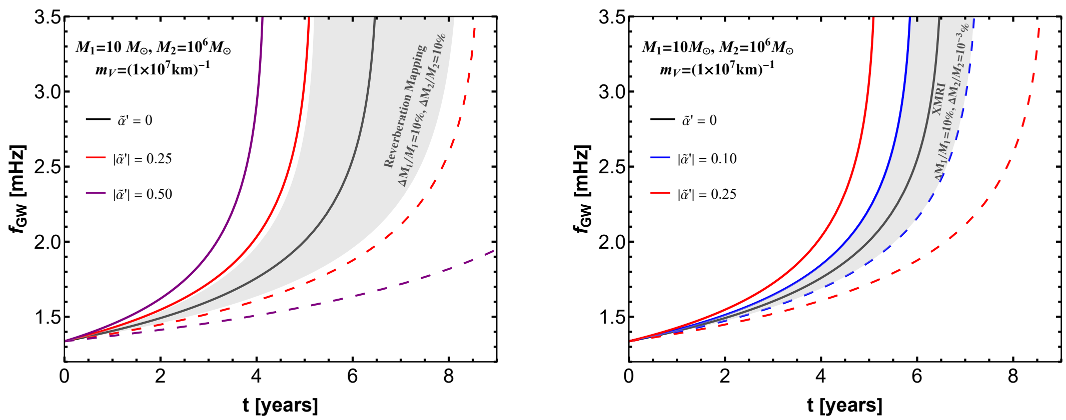

Figure 5.1: Evolution of the EMRI GW frequency $f_{\rm GW}$ of a $10M_\odot$ object inspiraling a $10^6M_\odot$ SMBH for a range of dark force strength values $\tilde{\alpha}'$ in the attractive case (solid) and repulsive case (dashed). The mediator mass is $(10^7\ {\rm km})^{-1}$. (*left*): the case of multimessenger EMRI signals with either reverberation mapping or stellar kinematics data, resulting in an uncertainty (displayed by the gray band) of 10% in determining both of the masses M_1 and M_2. (*right*): the case of multimessenger EMRI-XMRI signals, resulting in a fractional uncertainty (displayed by the gray band) of $10^{-3}\%$ in the SMBH mass M_2 and 10% in M_1.

5.2.2 Temporal Evolution of Gravitational Waves

We use formulas introduced in the last section to calculate GWs emitted by the EMRI system. Fig. 5.1 and Fig. 5.2 illustrate the evolution of the GW frequency $f_{\rm GW}$ and characteristic strain h_c for different choices of the dark force strength parameter $\tilde{\alpha}'$. The mass of the SMBH is chosen as $M_2 = 10^6M_\odot$, and the mass of the inspiralling black hole is $M_1 = 10M_\odot$. We assume, for simplicity, that both black holes are Schwarzschild black holes, though dark forces can also impact EMRIs involving rotating black holes. The mass of the mediator is $m_V = (10^7\ {\rm km})^{-1} \simeq 1.98 \times 10^{-17}{\rm eV}$, such that the force range is comparable to the ISCO radius of 8.9×10^6 km for a $10^6M_\odot$ SMBH. The associated GW frequency emitted at the ISCO is about 4.4 mHz. We evolve the EMRI system using Eq. (5.10) from the initial condition $f_{\rm GW} = 1.34$ mHz at $t = 0$, and

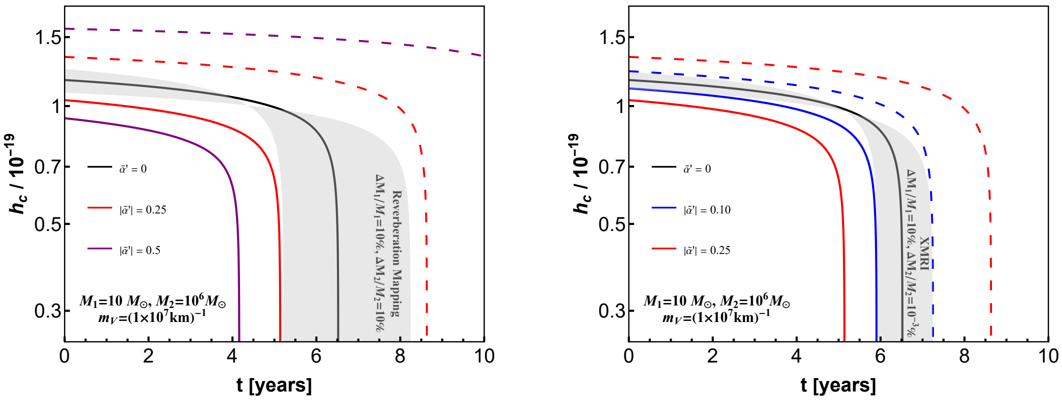

Figure 5.2: The temporal dependence of the characteristic strain h_c of the EMRI system for a range of dark force strength values in the attractive (solid) and repulsive (dashed) cases. The black hole and dark force mediator masses are chosen to be consistent with Fig. 5.1. (*left*): multimessenger measurement with reverberation mapping. The uncertainty of masses M_1 and M_2 is both 10%. (*right*): multimessenger measurement with XMRI. The uncertainty of masses M_1 and M_2 are 10% and $10^{-3}\%$ respectively.

calculate the GW emission power with Eq. (5.12). The corresponding initial EMRI components separation is about 2×10^7 km with a small difference depending on the type of interactions.

The colored curves in Fig. 5.1 show $f_{\rm GW}$ as a function of time in the cases with the absolute value of the dark force strength $|\tilde{\alpha}'| = 0.5$ (purple), 0.25 (red), and 0.1 (blue). The attractive force case ($\tilde{\alpha}' > 0$) is shown with solid curves while the repulsive force case ($\tilde{\alpha}' < 0$) is shown with dashed curves. As a comparison, we show the case in the absence of dark force with the black curve, together with a gray band representing the typical uncertainty from the determination of the black hole masses. In the left panel, we show the uncertainty of $\Delta M_2/M_2 = 10\%$ corresponding to reverberation mapping campaigns. In the right panel, the uncertainty is $\Delta M_2/M_2 = 10^{-3}\%$ corresponding to the mass determination with an XMRI measurement. In both panels, a 10% uncertainty for the mass of the inspiraling black hole $\Delta M_1/M_1 = 10\%$ is incorporated within the

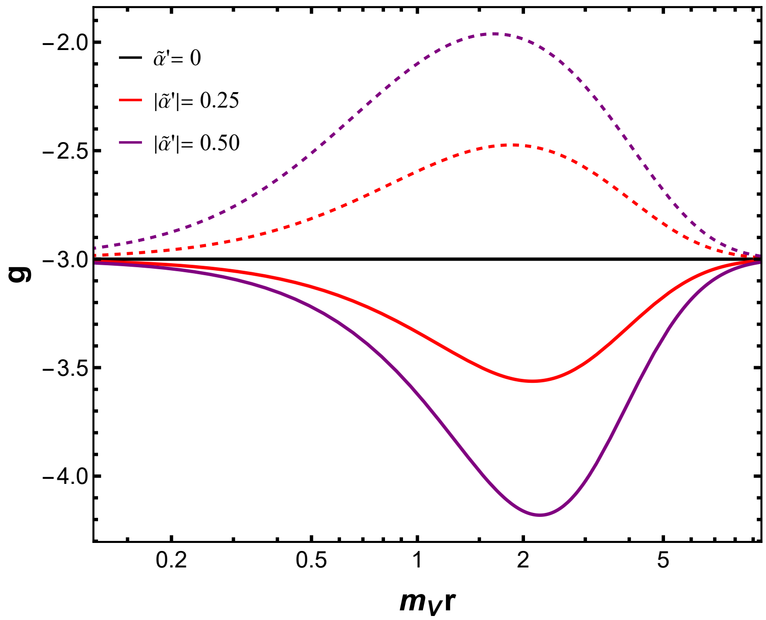

Figure 5.3: The coupling g defined in Eq. (5.11) as a function of the dimensionless force range $m_V r$ with different choices of $\tilde{\alpha}'$ for attractive dark force (solid) and repulsive dark force (dashed). The largest deviations from the gravitation-only case, $g = -3$, occur when $m_V r \sim 1$.

gray bands. Evidently, the attractive dark force accelerates the system towards ISCO, while the repulsive dark force slows down the system's evolution towards ISCO. Larger values of the effective dark force strength induce more significant deviations from the gravitation-only scenario. With a more precise multimessenger determination of M_2 in the right panel, a smaller $|\tilde{\alpha}'| = 0.1$ can be distinguished from the uncertainty band compared to the sensitivity of about $|\tilde{\alpha}'| = 0.25$ in the left panel.

In Fig. 5.2, we show the strain amplitude h_c as a function of time for the same EMRI event consisting $M_1 = 10 M_\odot$ and $M_2 = 10^6 M_\odot$ located at $d_L = 1$ Gpc, in the attractive dark force case (solid) and the repulsive dark force case (dashed). The inverse mediator mass is chosen to be 1×10^7 km. In all figures, the pure gravity case is shown with the black curve, and the benchmarks with non-zero dark force couplings are shown for $|\tilde{\alpha}'| = 0.5$ (purple), $|\tilde{\alpha}'| = 0.25$ (red), and $|\tilde{\alpha}'| = 0.1$ (blue), corresponding to the same benchmark values in Fig. 5.1. The SMBH mass uncertainty is shown with the gray band for 10% in the left panel, and for $10^{-3}\%$ in the right panel, while the mass uncertainty of the lighter component is kept to be 10% in both panels. We note that for an attractive (repulsive) dark force, the characteristic strain h_c is weaker (stronger) than the pure gravity case at a given time $t > 0$. This contrasts with the evolution of rms amplitude $h_{o,2}$ of GWs emitted toward infinity. The dependence is reversed as a result of the effect of the dark force on the GW frequency: when the EMRI system evolves faster to ISCO, it spends less time $f_{\rm GW}/\dot{f}_{\rm GW}$ in the fixed observation frequency window, such that the h_c in Eq (5.12) is suppressed. Similar to Fig. 5.1, we see that the effect of the dark force can be discerned best with a stronger dark force strength $|\tilde{\alpha}'|$.

The strain amplitude of a resolved EMRI signal is inversely proportional to the luminosity distance. Therefore, EMRI events that are closer can be measured with greater precision; indeed, as mentioned before, multimessenger studies involving EMRIs rely on stellar kinematics or reverberation mapping that are only effective at much smaller distances. Nevertheless, $d_L = 1$ Gpc represents a conservative choice.

In addition to the dark force strength, EMRIs are also sensitive to the mass of the mediator m_V, which determines the range of the dark force. The dependence on the mediator mass is from the g factor in Eq. (5.11). In the scenario where there is no dark force, as well as in the scenario where the range of the dark force is much longer or shorter than the EMRI separation, Eq. (5.11) reduces to $g = -3$. Conversely, the correction factor deviates from -3 when m_V is comparable to the inverse mutual separation of the EMRI components. We show the dependence of the g factor on the

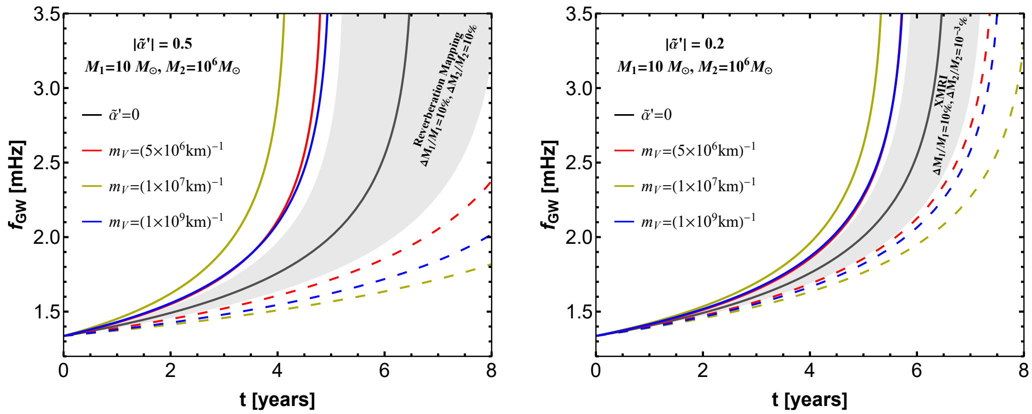

Figure 5.4: GW frequency versus time plot of a $10M_{\odot}$ object inspiraling a $10^6M_{\odot}$ SMBH for a range of the dark force mediator mass m_V. (*left*): the case of multimessenger EMRI signals with reverberation mapping data, resulting in an uncertainty of 10%in determining each of the masses M_1 and M_2. (*right*): the case of multimessenger EMRI-XMRI signals, resulting in an uncertainty of $10^{-3}\%$ in the SMBH mass M_2 and 10%in M_1.

relative values of m_V and r in Fig. 5.3, for the case of attractive (denoted by solid lines) as well as repulsive (denoted by dashed lines) dark force interactions. It is clear that significant deviations from the gravity only case occur when $m_V r \sim 1$. The deviation of the g from -3 introduces an effect on the EMRI evolution that agrees with the attractive or repulsive nature of the dark force. Specifically, the system evolves more quickly for an attractive dark force interaction when g is more negative around $m_V r \sim 1$, while it evolves more slowly for a repulsive dark force interaction when g is less negative around $m_V r \sim 1$.

The effect of the mediator mass on the EMRI is displayed in Fig. 5.4 with $f_{\rm GW}$ as a function of time for a fixed dark force strength but different mediator masses. We choose $\tilde{\alpha}' = 0.5$ in the left panel, and $\tilde{\alpha}' = 0.2$ for the right panel. The other EMRI parameters are kept to be consistent with Fig. 5.1. We also choose the initial frequency to be $f_{\rm GW} = 1.34$ mHz for all EMRIs. The corresponding initial black hole separation is about 2×10^7 km with small difference depending on the type of interactions. As a comparison, the ISCO radius is about 8.9×10^6 km for $M_2 = 10^6 M_\odot$. The mediator mass values are chosen to represent three different force range scenarios: short force range $m_V^{-1} = 5 \times 10^6$ km (red); intermediate force range comparable to the ISCO radius $m_V^{-1} = 10^7$ km $\sim R_{\rm ISCO}$ (yellow); and the very long-range force limit $m_V^{-1} = 10^9$ km (blue). As is expected from the dependence of the g factor on $m_V\, r$, the dark force effect of yellow curves exhibit more significant distinction from the gravity-only case (black), compared to the short-range and long-range force limits.

In the regime where $m_V \ll R_{\rm ISCO}^{-1}$, EMRI GWs can still discern between the gravitational attraction and an additional dark force if one advocates, as we have, for an independent mass measurement for which the dark force is switched off. This is different from the case of GW measurements from equal-mass binary systems, where the effect of the dark force becomes entirely degenerate with gravity: in that case, a rescaling of the binary component mass by a factor of $(1 + \tilde{\alpha}')^{2/5}$ mimics the presence of the dark force. The primary challenge in distinguishing the effect of the dark force stems from uncertainties in the pure gravitational contribution, which ultimately arises due to uncertainties in M_1 and M_2 (illustrated by the gray band). For instance, for a benchmark value of $\tilde{\alpha}' = 0.5$, the rescaling factor on the mass, $(1 + \tilde{\alpha}')^{2/5} \simeq 1.18$, exceeds the uncertainty in the reverberation mapping and the XMRI measurements. Consequently, the degeneracy is broken for EMRI GWs in the ultra-long-range force limit.

In the end, we show the EMRI GWs on the plane of strain versus frequency in Fig. 5.5, with the black and cyan dots indicating the remaining time from ISCO is 5 years and $1\ \mathrm{year}$ respectively. The mediator mass is set to $m_V^{-1} = 10^7\ \mathrm{km}$ to demonstrate the maximum effect. The upper panels illustrate the effects of the dark force compared to uncertainties determined by reverberation mapping, with a detailed zoom-in on the region where the dark force leads to a significant deviation from the gravity-only scenario. The lower panels show the case when uncertainties are determined by the XMRI measurement. The GW data collected over the last few years from the EMRI events in future observations will be utilized to precisely track the evolution of the strain versus the frequency, crucial for distinguishing the existence of the dark force. We will use the $h_c - f_{\mathrm{GW}}$ relation to calculate the sensitivity to the dark force in the next section.

5.2.3 Sensitivity with Multimessenger Measurements

We perform a likelihood analysis to test the future sensitivity to $\tilde{\alpha}'$ with the EMRI GWs and the additional independent measurement of the black hole masses. The likelihood analysis is based on the strain-frequency data of the GW signal. The likelihood is defined as [369]

$$\Lambda(s|\tilde{\alpha}') = \mathcal{K} \exp[(h_{\tilde{\alpha}'}|s) - \frac{1}{2}(h_{\tilde{\alpha}'}|h_{\tilde{\alpha}'}) - \frac{1}{2}(s|s)] \tag{5.15}$$

Here $\mathcal{K}$ is a normalization constant, $s(t)$ is the observed GW waveform in the time domain, and $h_{\tilde{\alpha}'}(t)$ is the waveform corresponding to a selected value of $\tilde{\alpha}'$. The scalar product between the two waveform is given by

$$(h_{\tilde{\alpha}'}|s) = 4\,\mathrm{Re}\int_{f_{\min}}^{f_{\max}} df_{\mathrm{GW}}\, \frac{\tilde{h}_{\tilde{\alpha}'}(f_{\mathrm{GW}})\,\tilde{s}(f_{\mathrm{GW}})}{S_n(f_{\mathrm{GW}})} \tag{5.16}$$

where $S_n(f_{\mathrm{GW}})$ represents the noise spectral density of the GW observatory and has a dimension of Hz^{-1}. Quantities denoted with a tilde represent the Fourier transform of the time domain data. Following the definitions in [370], we can write the scalar product as

$$(h_{\tilde{\alpha}'}|s) = \mathrm{Re}\int_{f_{\min}}^{f_{\max}} df_{\mathrm{GW}}\, \frac{h_{c,\tilde{\alpha}'}(f_{\mathrm{GW}})s_c(f_{\mathrm{GW}})}{f_{\mathrm{GW}}^2\, S_n(f_{\mathrm{GW}})} \tag{5.17}$$

The characteristic strain $h_{c,\tilde{\alpha}'}(f_{\mathrm{GW}})$ is calculated with the chosen dark force strength. The $s_c(f_{\mathrm{GW}})$ is obtained from the observed GW waveform. In the EMRI measurement, the upper limit $f_{\max}$ and the lower limit $f_{\min}$ of the integral in Eq. (5.17) is determined by the frequency range over which the waveform is observed, with the upper limit set to $f_{\mathrm{GW}}^{\mathrm{ISCO}}$ and the lower limit set to the EMRI GW frequency at 10 years before ISCO. The LISA observatory is set to observe for 4.5 years, with the possibility of extension up to 10 years [333, 334]. For the proposed μAres mission, a 10-year-long observation period is foreseen. Therefore, we use $t_{\mathrm{obs}} = 10$ years in our analysis. As long as the EMRI signal is stronger than the detector noise, the likelihood is mostly determined by the deviation of the signal spectrum in the presence of the dark force from the gravity-only spectrum (with mass uncertainties). We calculate the value of $\tilde{\alpha}'$ for a given m_V that maximizes the likelihood. This is equivalent to maximizing the log-likelihood, which we can read from Eq. (5.15) as

$$\begin{aligned}\log\,\Lambda(s|\tilde{\alpha}') &= \log\,\mathcal{K} + (h_{\tilde{\alpha}'}|s) - \frac{1}{2}(h_{\tilde{\alpha}'}|h_{\tilde{\alpha}'}) - \frac{1}{2}(s|s) \\ &= (h_{\tilde{\alpha}'}|s) - \frac{1}{2}(h_{\tilde{\alpha}'}|h_{\tilde{\alpha}'}) \end{aligned} \tag{5.18}$$

For an observed waveform $s(t)$, the term $\log\mathcal{K} - \frac{1}{2}(s|s)$ is a constant independent of the dark force effect and can be omitted from the definition of log-likelihood in the rest of the analysis.

To estimate the sensitivity to $\tilde{\alpha}'$, we assume that the observed signal corresponds to the dark force scenario. The likelihood of a gravity-only scenario is calculated with the assumed uncertainties in the masses of the EMRI components and $\tilde{\alpha}' = 0$. A scan across the parameter space of $\tilde{\alpha}'$ is performed to assess the likelihood with non-vanishing $\tilde{\alpha}'$. We further assume that the test statistic, denoted as τ, is χ^2-distributed under the null hypothesis. The two likelihoods are then compared at a 95% confidence level. The likelihood test statistics is

$$\tau = -2\left(\ln\,\Lambda(s|0) - \max_{\tilde{\alpha}\geq 0}\left[\ln\,\Lambda(s|\tilde{\alpha})\right]\right) \tag{5.19}$$

We will use the likelihood test statistics to calculate the sensitivity to the dark force strength and the force range. While the precision of GW measurements improves the sensitivity to $\tilde{\alpha}'$, the sensitivity to the dark force range depends on the mass of the SMBH involved in the EMRI event. We discuss the relation between the dark force range and the SMBH mass in the following. EMRI GWs are observed mostly when the orbits of the inspiraling object have decayed close to the ISCO radius, which can be written as $R_{\rm ISCO} = 6\,GM_2$ for Schwarzschild SMBHs. The frequency of GWs emitted when the separation is equal to the ISCO radius, $r = R_{\rm ISCO}$, is

$$f_{\rm GW}^{\rm ISCO} = \frac{1}{6\sqrt{6}\,\pi\,G\,M_2} \simeq 4.35\left(\frac{10^6 M_\odot}{M_2}\right)\ \text{mHz}. \tag{5.20}$$

This determines the observed GW frequency for EMRIs with different center SMBH masses. The frequency window of LISA is ideal to be used for observing GWs from $\sim 10^6 M_\odot$ SMBHs. On the other hand, EMRI GWs from heavier SMBHs appear at lower frequencies that are outside the LISA range. For example when $M_2 \sim 10^9 M_\odot$, the GW frequency lies in the unexplored μHz range. Future observations of μHz GWs have been proposed with space-based interferometers μAres [335], cold-atom interferometers [371], and using Solar System asteroids as test masses [372]. With a larger SMBH mass and consequently a wider ISCO radius, we can probe the dark force of a lighter mediator mass m_V, which would be indistinguishable from a rescaling of gravitational force with measurements at smaller separations. Therefore, the mediator mass of optimal sensitivity, the SMBH mass and the GW frequency can be correlated as follows,

$$m_V^{-1} \simeq 8.96 \times 10^8 \left(\frac{M_2}{10^8 M_\odot}\right)\ \text{km} \simeq 3.90 \times 10^8 \left(\frac{10^{-4}\ \text{Hz}}{f_{\rm GW}}\right)\ \text{km} \tag{5.21}$$

We present the sensitivity to $\tilde{\alpha}'$ across a range of the mediator mass m_V in Fig. 5.6. In particular, we choose two sets of representative GW event parameters: (1) $M_2 =$

$10^6 M_\odot, d_L = 10$ Mpc for lighter SMBHs; and (2) $M_2 = 10^8 M_\odot, d_L = 0.1$ Gpc for heavier SMBHs, to demonstrate their sensitivity to different mediator masses. In both benchmarks, the results are calculated by requiring $\tau = 4$ in Eq. (5.19) with different multimessenger measurements. In both cases, we will show that the optimal sensitivity is achieved when the mediator mass approximates the inverse of the EMRI separation, as can be seen from the minimum of the sensitivity curve at $m_V r \sim 1$.

In the first benchmark, the SMBH mass uncertainty can be independently constrained to within 10% by spectroscopic reverberation mapping or stellar kinematics, with which the sensitivity of EMRI GW measurement is shown with the red dotted curve in Fig. 5.6. Additionally, the SMBH mass can be measured within $10^{-3}\%$ uncertainty with XMRIs. The corresponding sensitivity is shown with the cyan dotted curve in Fig. 5.6. The EMRI GWs from $\sim 10^6 M_\odot$ SMBHs will be measured precisely with the future LISA observatory. We use noise power spectral densities reported in [329] for the LISA instrumental noise and the galactic confusion noise to obtain the sensitivity. We assume $M_1 = 10 M_\odot$ with 10% uncertainty. The results show that LISA has optimized sensitivity to $m_V \sim 10^{-17} - 10^{-16}$ eV, while it can still detect effects from longer mediator wavelengths. To illustrate sensitivities achieved through further reduction of uncertainties associated to the black hole masses, we present the sensitivity corresponding to $10^{-3}\%$ precision for both M_1 and M_2 in the black dashed curve.

In the second benchmark, we assume the sensitivity is set through GWs measured by the future μAres observation, combined with an independent SMBH mass measurement $\Delta M_2/M_2 = 10^{-3}\%$ from the XMRI. μAres is capable of detecting GWs with a sensitivity of $h_c \approx 10^{-18}$ at $f_{\rm GW} = 10^{-6}$ Hz. With such sensitivities, it will be able to observe Intermediate Mass Ratio Inspirals (IMRIs) involving $10^3 - 10^4\ M_\odot$ intermediate-mass black holes inspiralling onto $10^7 - 10^8\ M_\odot$ SMBHs out to $z \geq 6$ [335]. An IMRI system will respond to the dark force similarly to an EMRI, and the GW emission will be altered in a comparable manner. According to Eq. (5.21), an IMRI signal from a $10^8 M_\odot$ SMBH is able to probe $m_V^{-1} \gtrsim 10^9\ \mathrm{km}$. We assume $M_1 = 10^4 M_\odot$ for the intermediate-mass black hole, and use the μAres noise level reported in [335] to calculate its sensitivity. The final sensitivity is depicted by the blue dashed curve in Fig. 5.6. In the regions where the blue curve overlaps with the red and cyan curves, the dark force effect can be measured for both SMBHs of different masses, allowing the parametric dependence on $\tilde{\alpha}'$ and m_V to be disentangled.

Our study concentrates on the role of independent mass measurements; however, previous studies employing Fisher information matrix analysis demonstrated that uncertainties in EMRI parameters could potentially be reduced to an order of magnitude of $\mathcal{O}(10^{-4})$ [373], benefiting from the information in the GW waveform (see also applications to dark force effects in neutron star binaries [312]). In order to estimate the prospective sensitivity of an EMRI observation to the strength of the dark force utilizing the maximum likelihood criterion, we use the mass determination uncertainty of $10^{-3}\%$ to demonstrate the improvement of the sensitivity with both the multimessenger measurements and the dedicated waveform analysis. While a comprehensive waveform analysis that takes into account the additional dark force coupling within the model parameters is outside the scope of this study, our findings indicate that an independent measurement of the SMBH mass – one not influenced by the dark force – could resolve the degeneracy between the EMRI model parameters.

5.3 Conclusions

Our focus in this chapter has been to probe dark forces using EMRI systems. In contrast to other studies using compact object mergers, we have stressed on the importance of independent mass measurements of the central SMBH that do not depend on the interaction between the SMBH and stellar black hole partner of the EMRI system. Such independent mass measurements break the degeneracy of the effect of the dark force with a simple rescaling of the binary component masses. We have discussed two classes of such independent mass measurements, based on multimessenger studies involving other gravitationally bound systems and on photons. In the first class are XMRI systems involving the SMBH and a smaller object, such as a brown dwarf. In the second class are various existing methods of determining the SMBH mass, such as stellar kinematics and reverberation mapping campaigns. The SMBH mass determination in the first case can be very precise, with an uncertainty of $\sim 10^{-3}\%$, while a standard benchmark of the mass uncertainty using reverberation mapping is $\sim 10\%$. We have depicted both benchmarks in our results.

The question of localization of EMRIs using future GW detectors is important for our work. The LISA-TianQin or TaiJi-TianQin networks have the possibility of localizing GW events; such localization is frequency-dependent and has been estimated to be 200, 3, and 0.005 deg^2 at 1, 10, and 100 mHz, respectively [374]. A typical benchmark for the localization of EMRIs is $\lesssim 10$ deg^2 [330]. Multimessenger observations involving electromagnetic follow-ups, with the accretion disk or the broad line region, would further localize EMRIs (their potential as standard candles has been discussed by

[375]).

In this study, we have assumed that the corrections from environmental effects are negligible. SMBHs are known to exist in dense astrophysical environments, which may influence the dynamics of EMRIs [376, 377, 378]. Key processes such as gravitational pull from matter, accretion onto EMRI components, dynamical friction, and planetary migration can impact the gravitational waveform, potentially leading to biased parameter estimation and reduced detectability of EMRIs. We direct readers to [379] for information on the maximum level of corrections due to various environmental effects over a typical LISA mission. The environmental corrections are expected to be minimal for SMBHs surrounded by thick disks, but more substantial for those in thin disks, which are predominantly found in active galactic nuclei at high redshifts. Although SMBHs in thin disks contribute up to only a few percent of the EMRIs detectable by LISA with $z \lesssim 1$, potential uncertainties from environmental effects should also be considered when applying our method to these events.

Our results motivate multimessenger studies with coordination between GW detectors and reverberation mapping campaigns. In particular, SMBH mass determination by the OzDES-RM and SDSS-RM programs, and the AGN Black Hole Mass Database serve as rich targets for future EMRI studies. The upcoming SDSS-V Black Hole Mapper Reverberation Mapping Project is also important in this regard [380]. Similarly, SMBH mass determination by the SINFONI and MASSIVE Surveys using dynamical tracers also serve as possible targets for future EMRI sources. The best case scenario is the concurrent observation of an EMRI and an XMRI for a given SMBH.

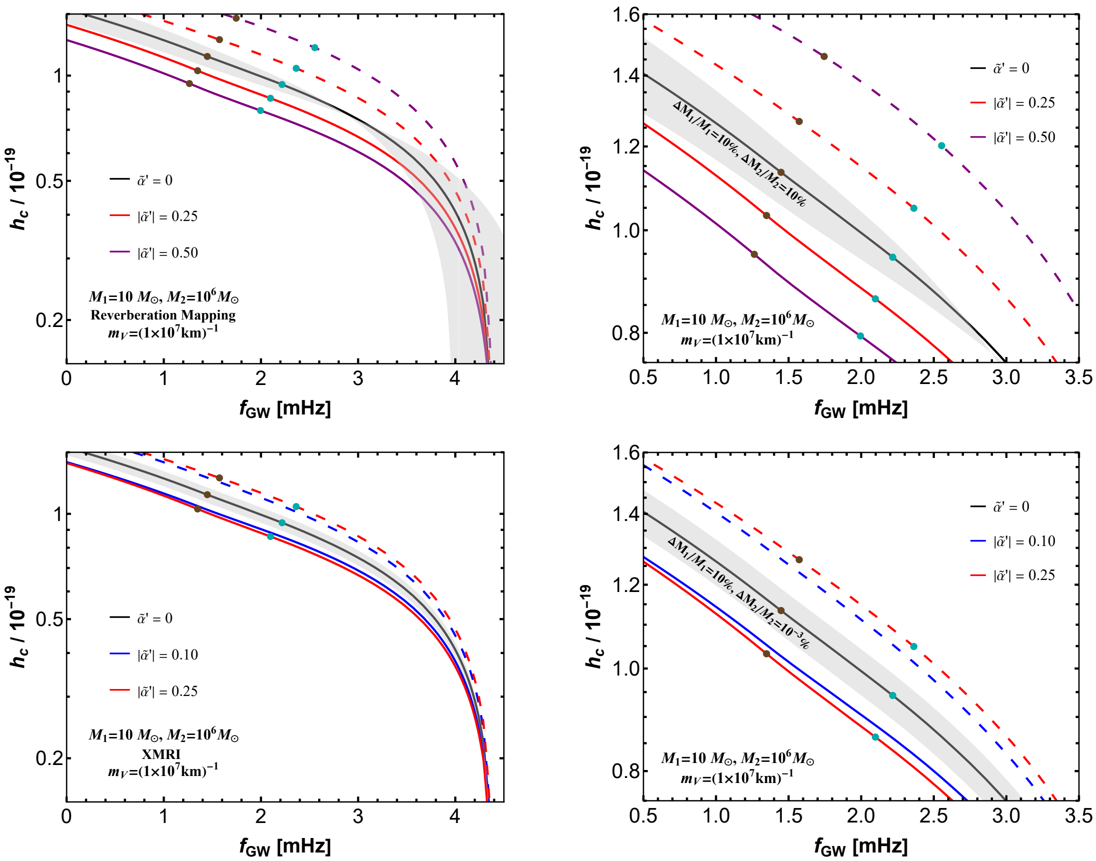

Figure 5.5: Strain h_c as a function of the GW frequency $f_{\rm GW}$ near ISCO. Color curves show the EMRI evolution with a range of dark force strengths. Black curve shows the evolution in a gravitation-only scenario. Brown dots indicate the evolution time is 5 years from ISCO while cyan dots represents 1 year left to ISCO. (*upper*): Dark force effect compared to the gravitation-only case, with mass uncertainties $\Delta M_1/M_1 = 10\%$ and $\Delta M_2/M_2 = 10\%$, depicted on the left, and zoom-in of specific regions on the right. (*lower*): Dark force effect compared to the gravitation-only case with $\Delta M_1/M_1 = 10\%$ and $\Delta M_2/M_2 = 10^{-3}\%$ on the left, and zoom-in plot on the right.

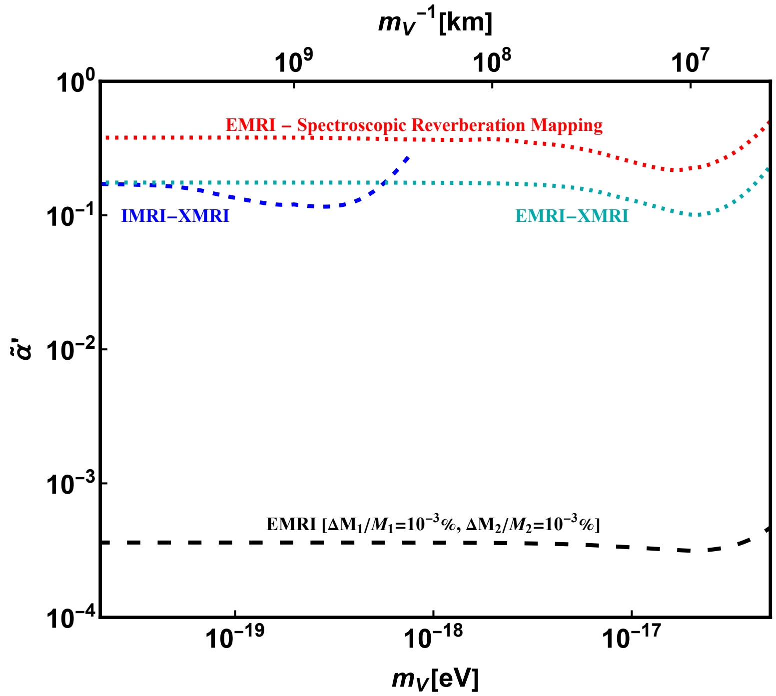

Figure 5.6: Projected 95% C.L. sensitivity of LISA and μAres to an attractive dark force on its strength $\tilde{\alpha}'$ and force mediator mass m_V. The cyan, red, and black curves assume the EMRI system consists of a stellar black hole of mass $M_1 = 10M_\odot$ and a SMBH of mass $M_2 = 10^6 M_\odot$. The cyan dotted curve corresponds to the case of EMRI-XMRI signals, resulting in an uncertainty of 10% in determining the value of M_1, and $10^{-3}\%$ in determining the value of M_2. The red dotted curve displays the sensitivity of EMRI signals complemented with spectroscopic reverberation mapping measurements, leading to a 10% uncertainty in both M_1 and M_2. The black dashed curve depicts the sensitivity of an EMRI waveform observed with an uncertainty of $10^{-3}\%$ in determining both masses. We also show the case of a heavier SMBH mass with the blue dashed curve for an IMRI-XMRI multimessenger measurement. The black hole masses are $M_1 = 10^4 M_\odot$ and $M_2 = 10^8 M_\odot$, with 10% uncertainty in M_1 and $10^{-3}\%$ uncertainty in M_2.

Chapter 6

Supernova-Boosted Dark Matter at Neutrino Detectors

Over the past few decades, the quest to unravel the fundamental nature of dark matter has stood at the forefront of modern physics, bringing together particle physicists, astrophysicists, and cosmologists in a concerted effort to explore the enigmatic constituents of the Universe [381, 382, 383]. Despite the extraordinary precision of observational cosmology, which demonstrates that dark matter accounts for a significant fraction of the total energy budget of the Universe [384, 385], its underlying properties–such as mass, spin, and interaction cross sections–remain elusive. Weakly interacting massive particles (WIMPs) [11, 386, 387] have been one of the most widely studied dark matter candidates that are probed by various direct, indirect, and collider experiments [388, 389, 390]. However, no conclusive evidence has yet emerged for the canonical WIMP model, prompting novel theoretical ideas and experimental approaches. Among these emerging ideas is the concept of *boosted dark matter* (BDM) [391, 392, 393, 394, 395, 396, 397, 398, 399, 400, 401, 402, 403, 404, 405, 406, 407, 408, 409, 410, 411, 412, 413, 414, 415, 416, 417, 418, 419, 420, 421, 422, 423, 424, 425, 426, 427, 428, 429, 430, 431, 432, 433, 434, 435, 436, 437, 438, 439, 440, 441, 442, 443, 444, 445, 446, 447, 448], wherein dark matter particles can receive a significant velocity or energy boost through various astrophysical processes in the present universe, thus leaving relativistic signatures of such dark matter in terrestrial detectors. Inspired by this novel idea, various neutrino and dark-matter direct detection experiments have conducted searches for BDM [449, 450, 451, 452, 453].

In parallel, neutrino detectors have become increasingly sophisticated and play a crucial role in multi-messenger astrophysics [454, 455, 456]. Originally developed to study neutrino oscillations and measure low-energy solar neutrinos, large-scale underground and underwater/ice-based detectors–such as Super-Kamiokande (SK) [457, 458, 459, 460], SNO [461, 462], Borexino [463, 464], KamLAND [465, 466, 467], IceCube [468, 469, 470], and JUNO [471, 472, 473]–have evolved into versatile instruments capable of detecting cosmogenic signals from a variety of physics channels, including supernova neutrinos [474], atmospheric neutrinos [475], and potential signatures of exotic physics beyond the Standard Model [476]. Down the line, near-future neutrino detectors, including DUNE [477, 478, 479, 480, 481] and Hyper-Kamiokande (HK) [482, 483, 484], are expected to advance this multi-faceted physics program with greater precision. The unique capabilities of these neutrino detectors, such as exquisite sensitivity to energy depositions as low as $\sim \mathrm{MeV}$ and extended exposure times that compensate for (relatively) low signal flux, have enabled their use as *dark matter detectors* in scenarios where BDM induces relativistic signatures in the present universe.

Recent theoretical developments emphasize that core-collapse supernovae may play a decisive role in dark matter phenomenology [485, 486, 487]. The high densities and extreme energies characteristic of supernova interiors create a fertile environment for particle production and scattering processes that can "boost" dark matter particles to energies well above their average halo velocities [488, 489]. *Dark matter from supernovae* has thus emerged as a novel avenue to explore the properties of dark matter, particularly by exploiting the synergy between BDM searches and neutrino detectors [490, 491, 492]. In this picture, a supernova event can serve as an intense source of BDM, endowing the particles with energies well beyond typical galactic dark matter velocities and yielding observable signals in detectors originally commissioned for neutrino physics. Moreover, the typical timing of supernova neutrino bursts, combined with any directionality information offered by certain detector technologies, can help discriminate potential BDM-induced events from backgrounds [491, 492].

While the prospect of detecting BDM from supernovae is theoretically compelling, addressing uncertainties in supernova modeling–particularly regarding dark matter production mechanisms and the nuclear equation of state–is crucial for a more robust understanding [493]. Variations in progenitor mass, metallicity, and rotation can alter the energy budget and particle flux. Furthermore, the strength of dark matter interactions with nucleons or leptons, along with the mass of any new mediator, significantly influences the likelihood of dark-matter production and escape [494, 488]. Advancing supernova simulations and improving nuclear physics constraints will be essential for refining flux estimates and enhancing the discovery potential of BDM in neutrino detectors.

In spite of these uncertainties, investigating supernova-induced BDM search prospects remains highly compelling, as successful detection could provide unique insights into both dark matter properties and core-collapse supernova dynamics. The potential to probe new physics in extreme astrophysical environments and complement terrestrial dark matter searches makes this avenue of exploration particularly valuable. The beginning effort in this direction was made in Ref. [495] within the context of ton-scale dark matter direct detection experiments. Diffuse fast-moving or boosted MeV-scale dark matter produced by supernova explosions carries sufficient energy to generate detectable signals through its interactions with nuclei, offering a pathway to explore previously uncharted regions of parameter space.

While nuclear scattering serves as a viable detection channel, electron scattering is expected to provide complementary insights in the search for supernova-induced BDM, as a significant fraction of the incoming BDM energy will be transferred to recoil electrons. However, typical ton-scale dark matter direct detection experiments are optimized for keV-to-sub-MeV energy deposits, whereas electron recoils from such BDM can extend well beyond the MeV range. These large energy deposits may lead to detector saturation issues, necessitating dedicated event selection strategies to enhance sensitivity to general BDM signals [404]. Nevertheless, access to the relevant parameter space is limited, and large-volume neutrino detectors play a crucial role, further benefiting from their substantial detection mass, which compensates for the low signal flux [412].

In this context, we explore the detection prospects of supernova-induced BDM signals at large-volume neutrino detectors such as DUNE [477, 478, 479, 480, 481], HK [482, 483, 484], and JUNO [471, 472, 473]. Using the conventional vector-portal dark matter scenario as a benchmark, we first analyze the prospects for detecting diffuse supernova-induced BDM signals. Additionally, we examine the sensitivity to BDM from a nearby supernova explosion occurring in the near future, taking Betelgeuse as an illustrative example. Notably, such BDM signals from local sources contribute to the emerging field of multi-messenger astrophysics, which integrates electromagnetic, neutrino, gravitational-wave, and (potential) dark-matter observations [496, 497, 498].

Due to the finite mass of dark matter, BDM signals from nearby supernovae would be detected with a characteristic delay following the arrival of the supernova neutrino burst. Moreover, the correlation between neutrino and BDM signals can serve as a valuable probe for identifying dark-matter properties, including its mass scale.

To convey our ideas efficiently, this chapter is organized as follows. In Section 6.1, we define our benchmark dark matter scenario and review the mechanisms by which dark matter in this scenario can attain large boost factors from supernova explosions. Section 6.2 discusses the detection of supernova-induced BDM at large-volume neutrino detectors, detailing the analysis strategy along with key parameters and features of our benchmark neutrino experiments. Our main results, including the detection prospects of supernova-induced BDM signals at these detectors and their implications for multi-messenger astrophysics, are presented in Section 6.3. Finally, we provide our conclusions in Section 6.4.

6.1 Boosted Dark Matter from Supernovae

To investigate the detection prospects of supernova-induced BDM at large-volume neutrino experiments, we consider a specific theoretical framework based on vector-portal dark matter models. For illustration, we assume fermionic dark matter, denoted by χ with mass m_χ, interacting with Standard Model electrons via the exchange of a dark-sector gauge boson. We adopt the commonly studied case of a dark photon, V_μ, which kinetically mixes with the Standard Model photon. The relevant interaction

Lagrangian is given by [499, 500]

$$-\mathcal{L}_{\rm int} \supset -\epsilon e \bar{\psi}_{\rm e} \gamma^\mu \psi_{\rm e} V_\mu + g_D \bar{\chi} \gamma^\mu \chi V_\mu, \tag{6.1}$$

where ϵ is the kinetic mixing parameter, e is the magnitude of the standard electromagnetic coupling, and g_D parameterizes the coupling strength between χ and the dark photon.

6.1.1 Average diffuse BDM flux from core-collapse supernova events

The fermionic dark matter produced in supernovae is emitted with a range of semi-relativistic velocities. As a result, a continuous flux of high-energy dark matter or supernova-induced BDM, arising from the overlapping emissions of different supernovae, is expected to reach Earth at any given time. To calculate the diffuse flux of supernova-induced BDM, we follow the approach outlined in Ref. [495], adopting the spatial supernova distribution model introduced in Ref. [501], which characterizes the rate of core-collapse supernovae (i.e., $\dot{n}_{\rm SN}(\vec{r})$) through a double-exponential function:

$$\dot{n}_{\rm SN}(\vec{r}) = A\, e^{-r/R_d}\, e^{-|z|/H}, \tag{6.2}$$

where A is a normalization parameter, r represents the radial distance from the galactic center, that is, the radial component in the cylindrical coordinate system, and z denotes the vertical offset from the midplane of the galaxy. For Type II supernovae, the two scale parameters, R_d and H are set to be 2.9 kpc and 95 pc, respectively, as specified in

Ref. [501]. Assuming an estimated galactic supernova rate of one event every 50 years, the normalization constant is determined to be $A = 0.00208\,\mathrm{kpc}^{-3}\,\mathrm{yr}^{-1}$. Earth's radial distance from the galactic center R_E and vertical offset z_E are taken to be 8.7 kpc and 24 pc, respectively.

The BDM flux contribution from a single supernova event diminishes with the square of its distance from Earth. To calculate the total diffuse BDM flux, we integrate over the distribution of supernovae in Eq. (6.2), weighting each contribution by $1/(\vec{r} - \vec{R}_E)^2$, where $\vec{r}$ and $\vec{R}_E$ denote the three-dimensional positions of a given supernova and Earth in galactic coordinates, respectively. The resulting total flux Φ_χ is

$$\Phi_\chi = N_\chi \int_{-z_{\max}}^{z_{\max}} dz \int_0^{2\pi} d\theta \int_0^{R_{\max}} r\, dr\, \frac{\dot{n}_{\mathrm{SN}}(\vec{r})}{4\pi|\vec{r} - \vec{R}_E|^2}, \tag{6.3}$$

where the quantity N_χ represents the total number of BDM particles produced by a single supernova, specifically those escaping the protoneutron star. We adopt the values calculated in Ref. [495] based on Monte Carlo simulations. The value of N_χ depends on the dark-matter mass m_χ and its relevant coupling, which is characterized by an effective coupling parameter y, defined as

$$y = \epsilon^2 \alpha_D \left(\frac{m_\chi}{m_V}\right)^4, \tag{6.4}$$

where $\alpha_D = g_D^2/(4\pi)$. Evaluating the integral in Eq. (6.3) at $R_{\max} = 20$ kpc and $z_{\max} = 1$ kpc gives the expected BDM flux at Earth from the galactic supernova population:

$$\Phi_\chi = N_\chi(m_\chi, y) \times 2.11 \times 10^{-55}\,\mathrm{cm}^{-2}\,\mathrm{s}^{-1}. \tag{6.5}$$

Finally, the BDM energy spectrum can be well approximated by a Fermi-Dirac distribution at the temperature T corresponding to its thermal decoupling from the protoneutron star, leading to the following differential flux at the production point:

$$\left.\frac{dN_\chi}{dE}\right|_{\mathrm{SN}} = N_\chi(m_\chi, y)\left(\frac{E^2 - m_\chi^2}{\exp(E/T)+1}\right)\left(\int_{m_\chi}^{\infty} dE\,\frac{E^2 - m_\chi^2}{\exp(E/T)+1}\right)^{-1}. \tag{6.6}$$

Assuming that the produced BDM particles do not significantly interact with the galactic medium during their propagation to Earth, the differential BDM flux at Earth is given by

$$\left.\frac{d\Phi_\chi}{dE}\right|_{E} = \Phi_\chi\left(\frac{E^2 - m_\chi^2}{\exp(E/T)+1}\right)\left(\int_{m_\chi}^{\infty} dE\,\frac{E^2 - m_\chi^2}{\exp(E/T)+1}\right)^{-1}. \tag{6.7}$$

It is instructive to examine the strength of BDM production from a single core-collapse supernova to build intuition about its detection prospects. Treating the protoneutron star as a blackbody, the rate at which dark matter particles escape from the supernova is determined by the radius at which the dark matter number-changing process freezes out. In our dark photon model, this process corresponds to dark matter annihilating into electron-positron pairs whose cross-section depends on the mass of the dark matter particle m_χ, and the coupling parameter y. As a result, the flux of dark matter particles escaping the supernova is highly sensitive to these two parameters. In addition, the energy of the escaping dark matter particles is set by the radius at which the dark matter thermally decouples from the SM bath. The key interaction that keeps the dark matter in thermal equilibrium is the dark matter-electron scattering. Consequently, the energy of dark matter particles depends on the values of m_χ and y as well. We follow the analysis of Ref. [495], and utilize their semi-analytic profile for the protoneutron star to calculate the flux and the energy spectrum of the escaping BDM particles.

6.1.2 BDM flux from a single core-collapse supernova event

The BDM flux from a single core-collapse supernova event, i.e., a point-like source, can be estimated by the formalism discussed in the previous section. First of all, the spatial supernova distribution is simply given by a Dirac delta function,

$$dN_{\mathrm{SN,src}} = \delta^{(3)}(\vec{r} - \vec{r}_{\mathrm{src}})\, d^3r. \tag{6.8}$$

where $\vec{r}_{\mathrm{src}}$ is the location of the source supernova. Taking $\dot{N}_\chi$ to be the total number of dark matter particles escaping the supernova per unit time, the BDM flux at Earth is

$$\Phi_{\chi,\mathrm{src}} = \frac{\dot{N}_\chi(m_\chi, y)}{4\pi|\vec{r}_{\mathrm{src}} - \vec{R}_E|^2}, \tag{6.9}$$

and the differential BDM flux at Earth,

$$\left.\frac{d\Phi_{\chi,\mathrm{src}}}{dE}\right|_E = \frac{\dot{N}_\chi(m_\chi, y)}{4\pi|\vec{r}_{\mathrm{src}} - \vec{R}_E|^2}\left(\frac{E^2 - m_\chi^2}{\exp(E/T)+1}\right)\left(\int_{m_\chi}^{\infty} dE\, \frac{E^2 - m_\chi^2}{\exp(E/T)+1}\right)^{-1}. \tag{6.10}$$

Note that, not surprisingly, the flux depends only on the distance between Earth and the source supernova of interest. Since we consider Betelgeuse as an illustrative example for this scenario, as mentioned earlier, we have $|\vec{r}_{\mathrm{src}} - \vec{R}_E|^2 = (197\ \mathrm{pc})^2$.

6.2 Detection of Boosted Dark Matter at Neutrino Detectors

We are now in the position to discuss how the supernova-induced BDM can be detected in our benchmark large-volume neutrino detectors. We begin by outlining the key features of the detectors that are relevant for estimating signal sensitivity. This is followed by a discussion of the direct detection mechanism and the expected rate of signal events, based on the model described in the previous section.

6.2.1 Benchmark neutrino detectors

As discussed in the previous section, BDM produced by supernova bursts can be as energetic as the sub-GeV scale, imparting tens of MeV to GeV-scale recoil energies to target particles in a detector. Many large-volume neutrino detectors operate within this ideal energy range to register BDM-induced scattering events. Additionally, their extensive operational lifetimes and high-duty cycles maximize exposure, providing an advantageous route for rare event detection.

Various large-volume neutrino experiments are currently operational or planned for the near future. In this study, we select three benchmark experiments with target volumes ranging from sub-kiloton to sub-megaton scales: DUNE, HK, and JUNO. For reference in subsequent sections, we outline some of the key detector specifications for these benchmark experiments.

DUNE [477, 478, 479, 480, 481]: The far detector of the Deep Underground Neutrino Experiment (DUNE) was originally planned to comprise four Liquid Argon Time Projection Chamber (LArTPC) modules and will be situated approximately 1,500 meters underground ($\approx 4,300$ meters water equivalent) at the Sanford Underground Research Facility in South Dakota, USA. At this depth, the expected cosmic-ray rate is $\sim 0.6\ \mathrm{m}^{-2}\mathrm{hr}^{-1}$. The first two far-detector modules, both LArTPC-based, are expected to be operational by late 2029, while the remaining two modules, including one LArTPC-based and another designated as a module of opportunity [502], are scheduled to begin scientific operations in early 2031. Each module will contain a total liquid argon (LAr) mass of about 17.5 kilotons (or 17.5 kt LAr-equivalent), with a fiducial mass of at least 10 kilotons (or 10 kt LAr-equivalent). These detectors are designed to provide excellent angular resolution, strong particle identification capabilities, and a relatively low energy threshold. For this study, we assume that all four modules are LArTPC-based, as any variation does not significantly affect our conclusions, provided the total detector mass remains at 4×17.5 kt LAr-equivalent.

Hyper-Kamiokande [482, 483, 484]: HK is a next-generation underground water Cherenkov experiment, building on the highly successful operation of Super-Kamiokande. The T2HK/T2HKK long-baseline neutrino experiment will use HK as its far detector for the upgraded J-PARC beam. The experiment will consist of two detectors, each featuring a cylindrical water tank, surrounded by about 40,000 photomultiplier tubes (PMTs). Each tank is 60 meters tall (with a fiducial height of 51.8 meters) and 74 meters in diameter (67.8 meters fiducial). They hold a total of 258 kilotons of water, of which 187 kilotons are the fiducial volume. The first detector will be located at the Tochibora mine, near the current Super-Kamiokande site in Japan, at a depth of 650 meters $\approx 1,750$ meters water equivalent), where the expected cosmic-ray rate is $\sim 27\ \mathrm{m}^{-2}\mathrm{hr}^{-1}$. The second detector is currently under consideration for construction beneath Mt. Bisul or Mt. Bohyun in Korea, with an overburden of about 1,000 meters ($\approx 2,700$ meters water equivalent), resulting in a reduced cosmic-ray rate of $\sim 5.7\ \mathrm{m}^{-2}\mathrm{hr}^{-1}$. The first detector in Japan is expected to begin operations in 2027. For electron detection, HK will achieve a relatively low energy threshold of ~ 5 MeV, although a significantly higher energy threshold is required to attain good angular resolution. For this study, we consider the first detector only.

JUNO [471, 472, 473]: The Jiangmen Underground Neutrino Observatory (JUNO) in Kaiping, Jiangmen, China is an advanced neutrino experiment utilizing liquid scintillator and is expected to begin operations in 2025. The JUNO central detector consists of a 35.4-meter-diameter acrylic sphere filled with 20 kilotons of linear alkylbenzene-based liquid scintillator, making it the largest liquid scintillator detector ever constructed. This sphere is surrounded by approximately 17,600 20-inch PMTs and 25,600 3-inch PMTs, providing an unprecedented light collection efficiency, an energy threshold as low as 0.1 MeV, and an excellent %-level energy resolution. The detector is located 700 meters underground (approximately 1,800 meters water equivalent) to reduce cosmic-ray backgrounds. JUNO's primary physics goals include precision measurements of neutrino oscillation parameters, supernova neutrino detection, and searches for new physics. The experiment is expected to achieve a low energy threshold, making it highly sensitive to a wide range of astrophysical and exotic neutrino sources. For this study, we assume JUNO's full fiducial mass of 20 kilotons and its nominal detector performance, as any small variations in operational parameters are not expected to significantly impact our conclusions.

As briefly discussed earlier, while direct detection experiments are sensitive to nuclear recoils, the above benchmark neutrino experiments can search for supernova-induced BDM signals through electron scattering, benefiting from their large target volumes and low thresholds for electron recoils. This provides complementary information in the broader search for supernova-induced BDM. The number of target electrons (henceforth denoted by N_T) varies across neutrino experiments based on their distinct designs. The massive HK detector has the largest count, with approximately 6.27×10^{34} electrons. DUNE follows with a significant, yet smaller, total of about 1.084×10^{34} electrons. JUNO has a comparatively lower count of roughly 6.95×10^{33} electrons, reflecting how the target scale is optimized for specific scientific objectives. DUNE's minimum detectable energy threshold for supernova-induced neutrinos is expected to be around 5 MeV, set by practical considerations of spallation backgrounds [503, 504]. HK adopts a similar threshold of approximately 5 MeV for supernova-induced neutrino detection to suppress backgrounds [505], although lower thresholds ($3.5 - 4.5$ MeV) are considered for solar neutrino measurements. JUNO, optimized for reactor antineutrinos,

Experiment	Material	N_T (Electrons)	Energy Thresholds
HK	Water (H_2O)	6.27×10^{34}	$\sim$ $5\,\mathrm{MeV}$ (supernova) [505]; $3.5–4.5\,\mathrm{MeV}$ (solar)
DUNE	Liquid Argon (Ar)	1.084×10^{34}	$\sim 5\,\mathrm{MeV}$ (supernova) [503, 504]
JUNO	Liquid Scintillator (C_9H_{12})	6.95×10^{33}	$\sim 0.1\,\mathrm{MeV}$ (reactor); $\sim 2\,\mathrm{MeV}$ (solar) [506, 507]

Table 6.1: The number of target electrons N_T and energy thresholds for our benchmark neutrino experiments. Thresholds vary depending on the neutrino sources and background suppression capabilities.

operates with a threshold near 0.1 MeV [506, 507], and aims for a higher threshold of about 2 MeV for solar neutrinos, depending on the level of radioactive contaminants. These numbers are summarized in Table 6.1. Based on these considerations, we adopt a threshold of 5 MeV for DUNE and HK, and 0.1 MeV for JUNO to assess their maximum detection potentials. More conservative thresholds are also explored later in our analysis.

6.2.2 Scattering between BDM and electron

Given the interaction Lagrangian in Eq. (6.1), an incoming BDM particle can manifest itself as an electron recoil via a t-channel exchange of the dark photon V. A detailed computation of the differential cross section is presented in Appendix D. Here, we summarize the key equations relevant for the discussion. The matrix element describing the scattering process $\chi e^- \to \chi e^-$ is written as

$$i\mathcal{M} = \frac{i\epsilon e g_D}{t - m_V^2} \bar{u}(p')\gamma^\mu u(p)\bar{u}(k')\gamma_\mu u(k), \tag{6.11}$$

where t is the Mandelstam variable defined as $t = (p - p')^2$. The initial and final momenta of BDM particles and electrons in the laboratory frame are given by

$$p^\mu = \begin{bmatrix} E_\chi \\ \\ \vec{p} \end{bmatrix}, \quad k^\mu = \begin{bmatrix} m_e \\ \\ \vec{0} \end{bmatrix}, \quad p'^\mu = \begin{bmatrix} E'_\chi \\ \\ \vec{p}' \end{bmatrix}, \quad k'^\mu = \begin{bmatrix} E_{r,e} \\ \\ \vec{k}' \end{bmatrix}, \tag{6.12}$$

where E_χ represents the energy of the incoming dark-matter particle, while $E_{r,e}$ denotes the energy of the recoiled electron. The squared amplitude of BDM and electrons can be written in spin-averaged form

$$\begin{aligned}\overline{|\mathcal{M}|^2} = \frac{8\,\epsilon^2 e^2 g_D^2 m_e}{(2m_e\{m_e - E_{r,e}\} - m_V^2)^2} \times \\ [m_e\{E_\chi^2 + (m_e + E_\chi - E_{r,e})^2\} \\ + (m_e^2 + m_\chi^2)(m_e - E_{r,e})]. \end{aligned} \tag{6.13}$$

The differential cross section in the laboratory frame can be expressed as [499, 500]

$$\begin{aligned}\frac{d\sigma}{dE_{r,e}} &= \frac{m_e}{8\pi\lambda(s, m_e^2, m_\chi^2)}\overline{|\mathcal{M}|^2} \\ &= \frac{\epsilon^2 e^2 g_D^2 m_e^2}{\pi\lambda(s, m_e^2, m_\chi^2)(2m_e[m_e - E_{r,e}] - m_V^2)^2} \times \\ &\quad [m_e\left\{E_\chi^2 + (m_e + E_\chi - E_{r,e})^2\right\} + (m_e^2 + m_\chi^2)(m_e - E_{r,e})], \end{aligned} \tag{6.14}$$

where $\lambda(x, y, z) = (x - y - z)^2 - 4yz$ and $s = m_e^2 + 2E_\chi m_e + m_\chi^2$. The kinematically allowed values of the electron recoil energy are determined by energy-momentum conservation. The maximum (minimum) allowed recoil energy E_e^+ (E_e^-) is [401]

$$E_e^{\pm} = \frac{(s + m_e^2 - m_\chi^2)(E_\chi + m_e) \pm \sqrt{\lambda(s, m_e^2, m_\chi^2)}\, p_\chi}{2s}\,, \tag{6.15}$$

where p_χ is the momentum of the BDM particle, given by $p_\chi = \sqrt{E_\chi^2 - m_\chi^2}$.

In summary, the outlined framework offers a consistent and comprehensive description of elastic BDM scattering off electrons. The underlying interaction is governed by a Lagrangian in which the dark-matter particle couples to a dark-sector mediator that kinetically mixes with the Standard Model photon. The scattering kinematics are fully specified by the Mandelstam variable s, the Källén function λ, and the explicit expression for the additional kinematic factor $\mathcal{K}(E_\chi, m_e, m_\chi, E_r)$, which encapsulates the energy and mass dependence of the process. Importantly, the formulation retains the full momentum-transfer dependence of the mediator propagator, ensuring precise modeling of the recoil spectra. This level of detail is essential for making reliable predictions in the context of BDM detection at electron-sensitive experiments.

6.2.3 Background considerations

Since our benchmark detectors are, or will be, located deep underground, one expects that the background contamination from cosmic rays (primarily from cosmic muons) would be insignificant. Nevertheless, the annual flux is not negligible, necessitating a more careful estimate.

The total muon fluxes expected at DUNE, HK, and JUNO detector locations are approximately 4×10^{-5} $\mathrm{m}^{-2}\mathrm{sr}^{-1}\mathrm{s}^{-1}$, 4×10^{-4} $\mathrm{m}^{-2}\mathrm{sr}^{-1}\mathrm{s}^{-1}$, and 2×10^{-3} $\mathrm{m}^{-2}\mathrm{sr}^{-1}\mathrm{s}^{-1}$, respectively [508]. Based on these flux values, we estimate that about 10^7 muons, 4.7×10^8 muons, and 2.5×10^8 muons pass annually through the DUNE-40kt, HK-187kt, and JUNO-20kt detector volumes, respectively. The outer detector of HK is used to detect the background cosmic muons and prevent them from affecting the data. The tagging efficiency–and therefore the muon rejection efficiency–is expected to exceed 99.9% [482, 483]. JUNO's central detector is immersed in a water pool equipped with a Cherenkov detection system, which is expected to identify cosmic muons with an efficiency of 99.8% [507]. In addition, the top tracker module provides further cosmic muon rejection capability [507]. In contrast, the DUNE far detectors do not include dedicated muon tagger modules. However, the photon detection system, combined with the excellent tracking capabilities of the LArTPC, enables muon tagging with an efficiency approaching 100%. In order for a muon to mimic a signal event, it must evade detection at the muon tagger modules or the active volume, sneak into the detector fiducial volume, and radiatively emit a photon that subsequently converts into an e^-e^+ pair [405, 413]. However, such emission becomes significant only above 100 GeV [509], where the related muon flux is highly suppressed underground and the resulting electron energy deposits are much larger than those typically expected from supernova-induced BDM. Based on all these considerations, the cosmic-muon-initiated backgrounds are expected to be insignificant or even negligible.

The primary irreducible background arises from atmospheric neutrinos. Quasi-elastic scattering of electron-flavor neutrinos, where the outgoing nucleons escape detection, can potentially mimic the signal events. The neutral-current contributions are typically subdominant, generally measured to be about $10 - 50\%$ of the corresponding charged-current contributions, depending on the interaction channel, neutrino energy, and target material [510]. Therefore, we will focus on the $\nu_e/\bar{\nu}_e$ charged-current events for illustrative background estimates.

To estimate the event rate, we combine the differential atmospheric $\nu_e/\bar{\nu}_e$ flux at the SK site, as calculated in Ref. [511], with the neutrino scattering cross sections from Ref. [510]. Using these inputs, the number of events for the relevant channels can be calculated as a function of the incident neutrino energy, as reported in Ref. [413]. Since our benchmark detector sites are located at similar latitudes and depths as the SK site, this serves as a reasonable approximation. Based on the data in Ref. [413], we estimate that approximately 37 events are expected per kt·yr, ignoring energy thresholds. However, typical supernova-induced BDM is not energetic enough to deposit more than $50 - 100$ MeV, depending on the mass of BDM. Figure 6.1 shows the kinematically allowed maximum recoil energy as a function of BDM mass. To determine this value, we identify the most probable BDM energy for each mass and substitute it into Eq. (6.15). The maximum recoil energy remains below 50 MeV across the BDM mass range, as expected just before. Notably, it decreases with increasing BDM mass due to the relatively low decoupling temperature of around 30 MeV in the proto-neutron star, which limits the boost of heavier BDM particles. Additionally, heavier BDM species are produced less abundantly, further reducing detection prospects. These observations suggest that an upper energy cut will further reduce the background events induced by atmospheric neutrinos. For example, less than 5% of quasi-elastic scattering events are produced from $\nu_e/\bar{\nu}_e$ neutrinos that have energies below 100 MeV.

When it comes to the BDM signals from a single supernova burst, signal isolation

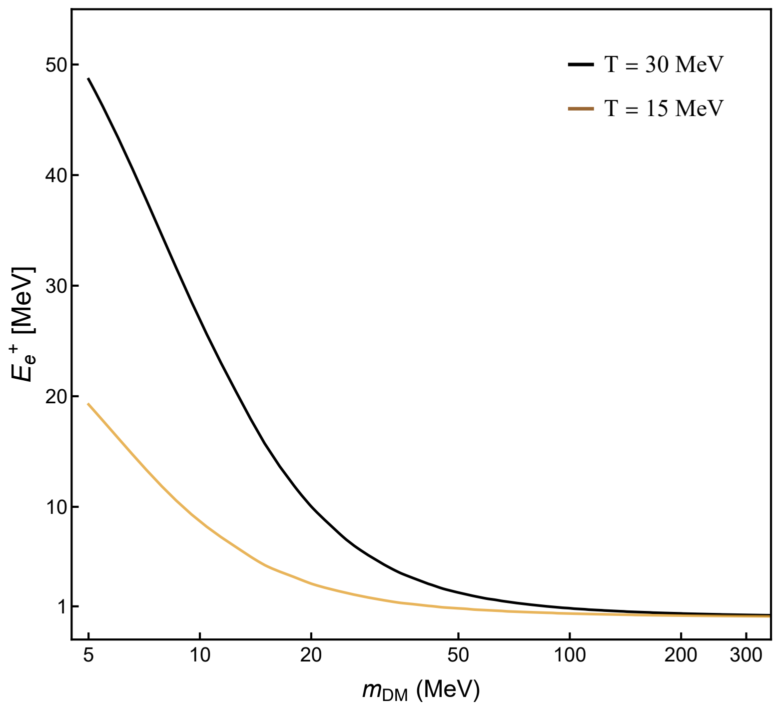

Figure 6.1: Maximum electron recoil energy corresponding to the most probable BDM energy for each mass, shown as a function of the BDM mass for two different temperatures at the time of thermal decoupling.

can be enhanced by utilizing timing and directionality information to further distinguish signal events from potential backgrounds. As we will discuss in Section 6.3.1, following a nearby supernova explosion, neutrinos and photons arrive at the detector first,[1] with BDM signals arriving later due to the finite mass of the BDM particles. Since photon and neutrino signals can be used to locate the supernova, the source direction of the BDM can be reconstructed by tracking recoil electrons with high angular resolution. For example, DUNE achieves an angular resolution of $\sim 1^\circ$ [477, 478, 479, 480, 481], while SK achieves between 25° and 3° for electrons in the $10 - 100$ MeV range [457, 458, 459, 460]. HK is expected to improve upon SK's performance with enhanced angular resolution. On the other hand, the JUNO detector uses a liquid scintillator that has a limited capacity to trace the path of recoil electrons. However, a recent study based on various machine learning techniques has demonstrated the potential of reconstructing electron recoil tracks with an angular resolution of $\sim 20^\circ - 30^\circ$ [512], although this performance was shown for GeV-scale ν_e-induced electron recoils.

All the considerations above clearly indicate that more precise background estimates will require dedicated studies that incorporate detailed detector response modeling, which lies beyond the scope of this work. Additionally, subdominant backgrounds not discussed above may become considerable or even significant in certain parameter regions, while evolving detector capabilities may help address these challenges. Rather than proposing detailed signal detection strategies optimized for various scenarios and experimental environments, in our sensitivity study, we present contours corresponding to 2.3 [i.e., the number of signal events corresponding to a 90% confidence level

[1] Though photons reach Earth slightly later due to their electromagnetic interaction nature.

(C.L.), assuming negligible background], 10, and 100 signal events. We anticipate that these illustrate the detection potential of supernova-induced BDM signals at varying strengths, while leaving detailed detector response studies–particularly those related to directionality–to the experimental collaborations.

6.3 Results

In this section, we discuss the expected event rates of supernova-induced BDM at our benchmark neutrino detectors. For the dark-matter model under consideration, a BDM particle reaching a detector can interact with either electrons or nuclei/nucleons in the detector material. If BDM interacts with the nucleus, it can manifest itself as a nuclear recoil, which existing WIMP detectors are well-equipped to observe [495]. However, as discussed in the introductory section, in large-volume neutrino detectors, typical supernova-induced BDM is not energetic enough to surpass the threshold for nucleon recoils but can produce observable electron recoils above the MeV scale. For a neutrino detector, the total expected number of BDM events during the observation time T_{obs} is given by

$$N_{\text{sig}} = N_e \, T_{\text{obs}} \int_{E_{\text{min}}}^{E_{\text{max}}} dE_{\text{r,e}} \int_{m_\chi}^{\infty} dE \frac{d\sigma}{dE_{\text{r,e}}} \frac{d\Phi_\chi}{dE} \,, \tag{6.16}$$

where N_e is the total number of target electrons within the detector fiducial volume, $d\sigma/dE_{\text{r,e}}$ is the differential BDM-electron cross section described in Section 6.2.2, and $d\Phi_\chi/dE$ is the differential flux of BDM particles discussed in Section 6.1. The relevant

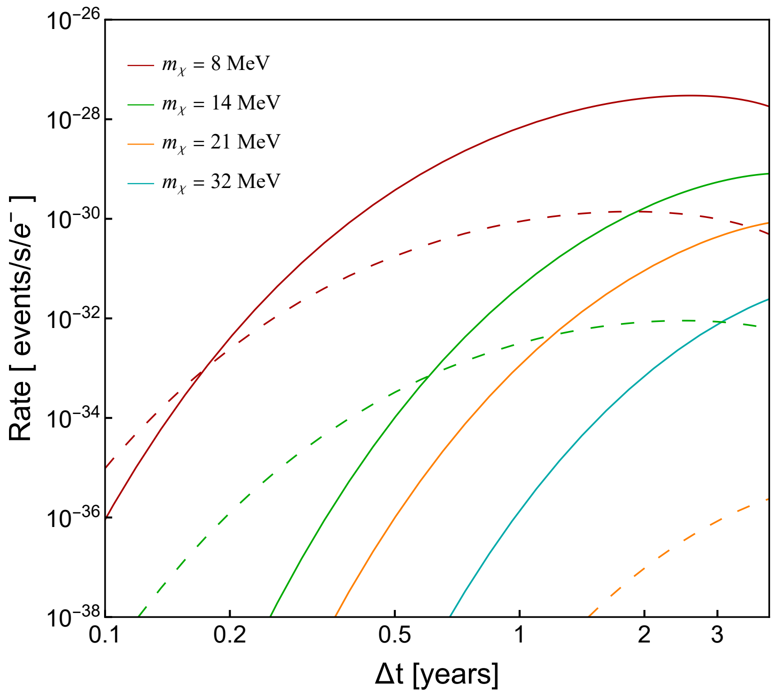

Figure 6.2: The event rate of BDM particles from Betelgeuse per unit time per target electron. The solid lines correspond to $y = 10^{-18}$, while the dashed lines correspond to $y = 10^{-20}$. The detector threshold is considered to be 30 MeV in our estimation.

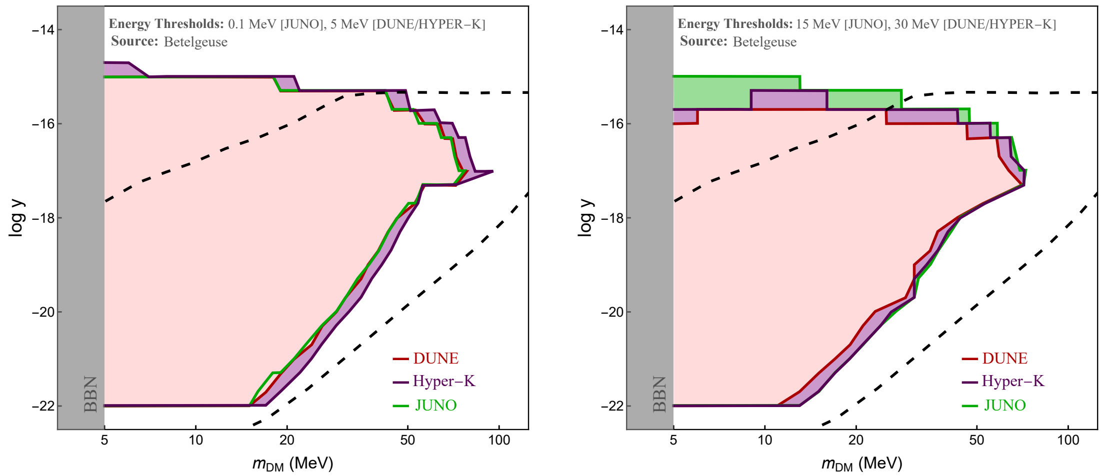

Figure 6.3: The 90% C.L. sensitivity regions for DUNE (in red), JUNO (in green), and HK (in purple) for a 10-year observation period. **Left:** The detector threshold for electron recoil is set to 5 MeV for DUNE and HK [503, 504, 505], while for JUNO, it is set at 0.1 MeV [506, 507] as mentioned in Table 6.1. **Right:** The threshold for electron recoil is set to 30 MeV for DUNE and HK, and to 15 MeV for JUNO. The region bounded by the dashed curve is excluded by the cooling argument. The dark-matter mass below 5 MeV is excluded by BBN [513].

electron recoil energy range is determined by $E_{\rm min}$ and $E_{\rm max}$:

$$E_{\rm min} = \max[E_{\rm th},\ E_e^-], \tag{6.17}$$

$$E_{\rm max} = E_e^+, \tag{6.18}$$

where $E_e^\pm$ is defined in Eq. (6.15), and $E_{\rm th}$ denote the detector's energy threshold.

In the following subsection, we present our sensitivity estimates obtained for the diffuse galactic flux, originating from the combined emission of numerous galactic supernovae, and BDM signals from a nearby isolated supernova, using Betelgeuse as an example. The sensitivity regions for both scenarios are illustrated in Figures 6.3, 6.4, and 6.5, respectively.

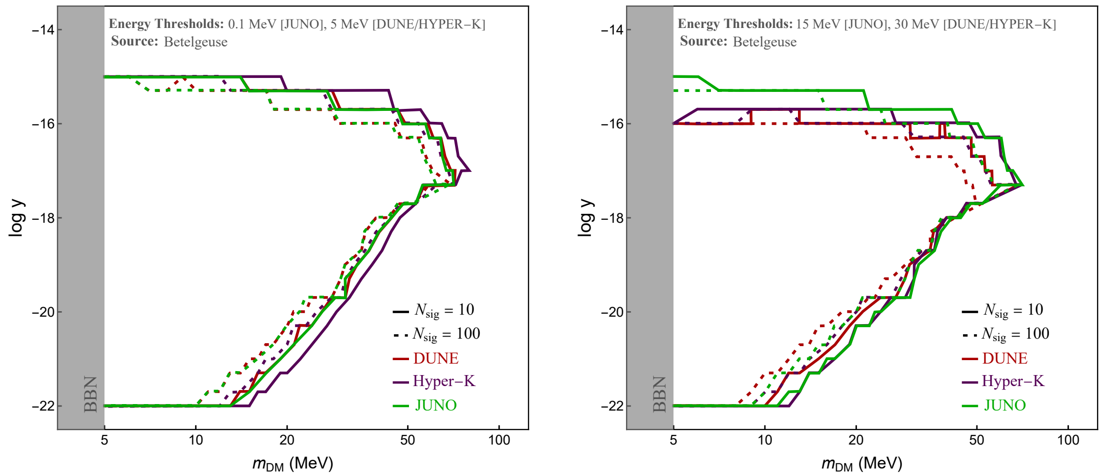

Figure 6.4: Event counts for supernova-induced BDM at DUNE, JUNO, and HK over a 10-year observation period. **Left:** the detector threshold for electron recoil is set to 5 MeV for DUNE and HK, while for JUNO, it is set at 0.1 MeV. **Right:** The threshold for electron recoil is set to 30 MeV for DUNE and HK, and 15 MeV for JUNO. The dark-matter mass below 5 MeV is excluded by BBN [513].

6.3.1 Multi-messenger signals from a single supernova event

A red supergiant located in the Orion constellation, Betelgeuse, is getting close to the end of its life cycle and is located nearly 642.5 light-years (or 197 parsecs) away from Earth [514, 515]. Its eventual supernova explosion offers a rare opportunity to detect BDM from a well-localized, point-like astrophysical source. In this context, both neutrinos and dark matter particles are expected to be emitted from a compact region, allowing the resulting BDM flux to be described as in Eq. (6.10).

Supernova-produced BDM particles, due to the (semi-relativistic velocities at which they are emitted), will arrive at Earth sometime after the photons and neutrinos. If the supernova is relatively close to Earth, the time difference between the arrival of the BDM and neutrinos can be quite small. Therefore, a single nearby supernova event offers an excellent opportunity for multi-messenger studies involving dark matter and neutrinos. Letting Δt represent the time difference of arrival between the photons and the dark matter particles, we have

$$\Delta t = \frac{D_S}{v_\chi} - \frac{D_S}{c}, \tag{6.19}$$

where D_S is the distance of the source from Earth, v_χ is the velocity of the BDM particle, and c is the speed of light. Hereafter, we set the value of c to 1. The velocity of BDM particles depends on the mass parameter and the energy at which they are produced. For a dark-matter particle of mass m_χ and energy E_χ, its velocity is given by

$$v_\chi^2 = 1 - \frac{m_\chi^2}{E_\chi^2}. \tag{6.20}$$

At any given time, a dark matter particle of a specific mass arriving at the detector carries a fixed amount of energy. As a result, the number of observed events per unit time can be written as

$$\frac{dN_{\rm sig}}{dt} = N_e\, \Phi_\chi(t) \int_{E_{\rm min}}^{E_{\rm max}} dE_{\rm r,e} \int_{-\infty}^{\infty} dE\, \frac{d\sigma}{dE_{\rm r,e}}\, \delta(E - E_\chi(t))\,. \tag{6.21}$$

In Figure 6.2, we show the event rate of BDM at neutrino detectors as a function of time following neutrino detection, considering a range of masses and coupling strengths. Since the core temperature in a SN is approximately 30 MeV, dark matter particles with masses below this temperature are produced with significant boosts and arrive soon after the neutrinos. In contrast, heavier dark matter particles are less boosted and may take several years to come after the neutrinos. Therefore, unlike the diffuse galactic flux, which remains approximately constant over time, the dark matter flux from a nearby single source, such as Betelgeuse, can vary significantly. Hence, the total number of events expected for a neutrino detector during the observation period T_{obs} is calculated by time-integrating the flux.

$$N_{\text{sig}} = N_e \int_0^{T_{\text{obs}}} dt\, \Phi_\chi(t) \int_{E_{\min}}^{E_{\max}} dE_{\text{r,e}} \int_{-\infty}^{\infty} dE\, \frac{d\sigma}{dE_{\text{r,e}}}\, \delta(E - E_\chi(t))\,. \tag{6.22}$$

The corresponding sensitivity at 90% C.L. for a 10-year exposure, assuming negligible background, is shown in Figure 6.3. As anticipated, the sensitivity decreases for relatively heavier dark matter particles, as they are less boosted and may require longer than the observation time to reach Earth. As computed in Ref. [495], we also show the region of the parameter space constrained by cooling; given SN1987A observations, the light dark matter particles cannot carry energy out of the protoneutron star at a rate larger than that of neutrinos. In Figure 6.4 we display the contours corresponding to different background assumptions, i.e., 10 and 100 signal events over a 10-year exposure.

6.3.2 Diffuse galactic flux of supernova-induced BDM

Dark matter particles produced in a supernova possess a semi-relativistic velocity with an $\mathcal{O}(1)$ spread, causing them to arrive at Earth significantly later than photons and neutrinos. However, this also means that BDM particles originating from different supernovae can arrive at Earth concurrently. The resulting flux was quantitatively analyzed in Section 6.1.1. The flux depends on the dark matter mass m_χ and the effective

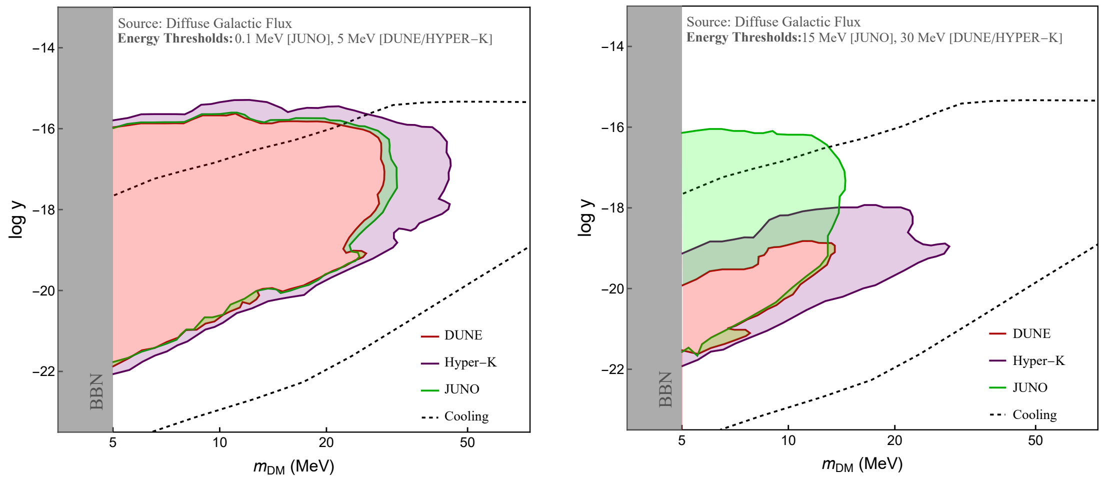

Figure 6.5: The 90% C.L. sensitivity regions for DUNE (in red), JUNO (in green), and HK (in purple) for a 10-year observation period. **Left:** The detector threshold for electron recoil is set to 5 MeV for DUNE and HK [503, 504, 505], while for JUNO, it is set at 0.1 MeV [506, 507] as mentioned in Table 6.1. **Right:** The threshold for electron recoil is set to 30 MeV for DUNE and HK, and to 15 MeV for JUNO. The region bounded by the dashed curve is excluded by the cooling argument. The dark-matter mass below 5 MeV is excluded by BBN [513].

coupling y through the dark gauge boson. For large couplings, BDM becomes trapped within the proto-neutron star [495], causing the flux to be exponentially suppressed. Conversely, if the coupling is too small, dark-matter production itself is inefficient, also leading to a suppressed flux.

To generate a detectable signal in a neutrino detector, the BDM must deposit enough energy to ensure that the electron recoil energy exceeds the detector's threshold, while remaining below the maximum energy probed by the instrument. Since most electron recoils from supernova-induced BDM are expected to lie near the detector's threshold, the threshold energy $E_{\rm th}$ plays a key role in determining the event rate.

Figure 6.5 presents the estimated 90% C.L. sensitivity to supernova-induced BDM signals at our benchmark neutrino detectors. Assuming negligible background levels, the energy thresholds could be lowered to 5 MeV for DUNE and HK, and to 0.1 MeV for JUNO, enabling us to estimate the maximum achievable sensitivity at each experiment. The results for this optimistic scenario are displayed in the left panel. In contrast, the right panel presents a more conservative sensitivity estimate, based on an energy threshold of 30 MeV for DUNE and HK, and 15 MeV for JUNO, again assuming a negligible background. In both cases, we assume a 10-year time exposure. As the BDM mass increases, both the BDM-electron scattering cross section and the diffuse galactic flux decrease, resulting in a reduced event rate. Consequently, the sensitivity of neutrino detectors declines for heavier BDM. For larger values of couplings, the radius at which the dark matter particle thermally decouples from the SM bath of the protoneutron star is large. This is because dark matter can scatter with electrons at lower densities when the interaction cross-section is significant. However, as we move away from the core, the temperature of the protoneutron star decreases. Consequently, dark matter particles that have strong couplings to SM particles are produced with lower boosts. As a result, the neutrino detector with the smallest threshold is most sensitive to large values of couplings, as seen in Figure 6.5. An increase in the detection volume can compensate for the higher detector threshold for some masses, as seen for HK in Figure 6.5. Finally, as previously announced, we present in the Figure 6.6 the contours corresponding to 10 and 100 signal events for a 10-year exposure, reflecting different background assumptions.

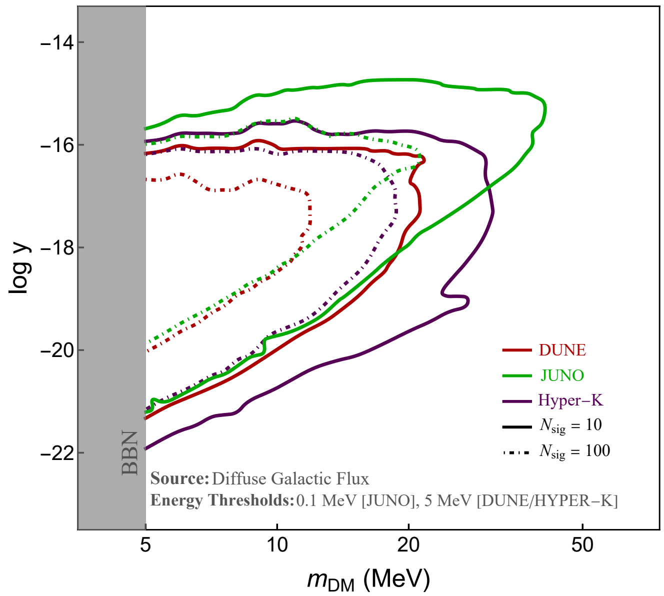

Figure 6.6: Event counts for diffuse galactic flux of supernova-induced BDM at DUNE, JUNO, and HK over a 10-year observation period. The detector threshold for electron recoil is set to 5 MeV for DUNE and HK, while for JUNO, it is set at 0.1 MeV.

6.4 Conclusions

We studied fermionic dark matter produced and boosted at supernovae that can be probed in next-generation neutrino detectors. The BDM of this sort, interacting via dark gauge bosons (e.g., dark photons), can be produced and accelerated in core-collapse supernovae. It can give a relatively large flux that might be observable at Earth. By considering the modeling of diffuse galactic supernovae and nearby sources like Betelgeuse, we predict event rates at DUNE, HK, and JUNO. Moreover, we investigated a multi-messenger approach that represents a sensitivity to unexplored dark-matter parameter space, especially in the MeV to sub-GeV mass range with feeble couplings.

Supernovae as natural sources for energetic particles can produce BDM efficiently via dark gauge boson interactions due to the extreme conditions. We have considered both diffuse flux as a background from past supernova events and bursts from nearby events, motivated by the simulation in Ref. [495]. Producing energetic dark matter at supernovae can be observable in near-future sensitive dark matter and neutrino detectors. BDM from nearby supernova events could present an excellent detection possibility due to larger flux and closer distance to Earth.

We have also looked into a possible multi-messenger approach for BDM emission and its detection prospect at Earth. The time delay between neutrinos and BDM is related to the dark-matter mass and speed, providing a means to distinguish potential signals from either diffuse or point-like sources. Correlations with other messengers, such as gravitational waves, can further enhance the multi-messenger approach.

Furthermore, we have found that a wide range of dark-matter masses and interaction strengths coupled to the Standard Model can be explored through a dark gauge boson. We have shown our main sensitivity prospects in Figures 6.5 and 6.4 for diffuse sources and in Figure 6.3 for a point-like source at the location of Betelgeuse. Using the characteristic features of current and future neutrino detectors, we have obtained projected sensitivity curves covering a range of dark-matter masses and effective couplings. A possible supernova event could either produce a BDM signal, potentially leading to the first non-gravitational detection of dark matter originating from the extreme environment of a supernova or further improve existing constraints. Depending on the number of observed events, our sensitivity curves span dark-matter masses from ~ 5 MeV to ~ 100 MeV, with effective coupling values y ranging from $\sim 10^{-14}$ to $\sim 10^{-22}$, as shown in the figures. We have also compared our results with the sensitivity curves for dark-matter direct detection experiments presented in Ref. [495].

The high energy resolution and huge fiducial volume of DUNE, the continuous operation of JUNO, and the vast size of HK can improve complementary capabilities for probing BDM originating from various sources, including supernovae. These experiments can serve as effective tools for dark matter detection, complementing dedicated dark matter detectors. In the occurrence of the next nearby supernova (possibly Betelgeuse), its high flux would offer an exciting opportunity to constrain the dark-matter parameter space and study multi-messenger astrophysics.

In the future, efforts can focus on refining models of dark-matter production from supernovae by improving simulations of BDM production and emission. Enhancements in background reduction will also be crucial for increasing the sensitivity of neutrino detectors to rare events, potentially including BDM signals. In addition to supernovae, other astrophysical sources such as active galactic nuclei, neutron star mergers, and cosmic rays can also serve as additional sources of BDM. All in all, neutrino detectors provide a promising avenue for testing various dark-matter models, particularly those involving low-mass dark matter and small couplings to Standard Model particles, making them attractive targets for further study and detection prospects.

Appendix A

Dynamical Friction in a Gaseous Medium

Dynamical friction (DF) refers to the deceleration experienced by a massive object moving through a background medium of lighter particles. In a collisional medium, such as baryons, the motion of the massive object gravitationally perturbs the surrounding gas, inducing an overdense region known as a wake. The gravitational attraction between the wake and the moving object exerts a drag force that slows down the object. Following Ref. [55], we can define the DF force of a perturber of mass M moving through the baryon fluid as

$$F_{\mathrm{DF}} = \frac{4\pi G^2 M^2 \rho_{\mathrm{B}}}{v_{\mathrm{rel}}^2} \mathcal{I}(\mathcal{M}, \Lambda), \tag{A.1}$$

where v_{rel} is the relative velocity of the perturber with respect to the rest frame of the gas, and ρ_{B} is the mass density of the gas. $\mathcal{I}$ is the result of integrating the gravitational force decelerating the wake over the entire wake, and is a function of the Mach number $\mathcal{M} \equiv v_{\mathrm{rel}}/c_s$ with c_s being the sound speed of the baryons, and the Coulomb logarithm $\log \Lambda$, defined simply as

$$\ln \Lambda \equiv \ln \left(\frac{b_{\mathrm{max}}}{b_{\mathrm{min}}} \right) . \tag{A.2}$$

This function introduces two regulators that regulate the gravitational force between the perturber and the gas at small and large impact parameters b_{min} and b_{max}, respectively, where the approximation of an isolated, point-like perturber breaks down. The force of DF will be effective as long as $b_{\rm max}$ is greater than $b_{\rm min}$ and the assumption of a point-like perturber holds true. While there is some arbitrariness to any choice of these impact parameters, our results are only logarithmically sensitive to them.

Under the assumption that the density perturbations generated by the perturber are small, and that the equations of motion can be expanded to linear order, the full expression for $\mathcal{I}(\mathcal{M},\Lambda)$ is

$$\mathcal{I}(\mathcal{M},\Lambda) = \begin{cases} \frac{1}{2}\ln\left(\frac{1+\mathcal{M}}{1-\mathcal{M}}\right) - \mathcal{M}, & \mathcal{M} < 1 - x_{\rm min}, \\ \frac{1}{4}x_{\rm min} - \frac{\mathcal{M}}{2} - \frac{1-\mathcal{M}^2}{4x_{\rm min}} + \frac{1}{2}\ln\left(\frac{1+\mathcal{M}}{x_{\rm min}}\right), & 1 - x_{\rm min} < \mathcal{M} < \sqrt{1+x_{\rm min}^2}, \\ -\frac{1}{4x_{\rm min}} + \frac{(\mathcal{M}-x_{\rm min})^2}{4x_{\rm min}} + \frac{1}{2}\ln\left(\frac{1+\mathcal{M}}{x_{\rm min}}\right), & \sqrt{1+x_{\rm min}^2} < \mathcal{M} < 1 + x_{\rm min}, \\ \frac{1}{2}\ln\left(\frac{\mathcal{M}+1}{\mathcal{M}-1}\right) + \ln\left(\frac{\mathcal{M}-1}{x_{\rm min}}\right), & \mathcal{M} > 1 + x_{\rm min}\,, \end{cases} \tag{A.3}$$

where $x_{\rm min} \equiv (1+\mathcal{M})/\Lambda$. Note that in Ref. [55], only the $\mathcal{M} \ll 1$ and $\mathcal{M} \gg 1$ limits were obtained; however, both of these expressions diverge as $M \to 1$, which is slightly unsatisfactory, although in practice this is usually not a problem since typically $\Lambda \gg 1$, and the range of $\mathcal{M}$ for which $1 - x_{\rm min} < \mathcal{M} < 1 + x_{\rm min}$ is very small. By carefully carrying out the integration over the wake, one recovers the expressions above, which are continuous for all $\mathcal{M}$.

In the subsonic limit with $\mathcal{M} \ll 1$, $\mathcal{I}(\mathcal{M},\Lambda) \approx \mathcal{M}^3/3$, and the DF force is suppressed. In the linear theory approximation, this can be understood from the fact that the gas density perturbations generated by the perturber are almost spherically symmetric. However, in the supersonic case, the perturbed density distribution lags behind the perturber in the shape of a cone. This asymmetrical distribution of gas around the perturber generates a significant drag force, peaking at $\mathcal{M} = 1$. When the motion is supersonic, the force of dynamical friction, and consequently the heating rate, depends on the Coulomb logarithm; thus, $b_{\rm min}$ and $b_{\rm max}$ must be chosen carefully in Eq. (A.2). Our choices are detailed in the main body of the paper, but to facilitate the discussion here, we will restate them. For MACHOs, we set $b_{\rm min}$ to be the Bondi–Hoyle–Lyttleton radius, *i.e.*

$$b_{\rm min,\,M} = \frac{GM}{c_s^2 + v_{\rm rel}^2}\,, \tag{A.4}$$

motivated by the fact that gas within this radius get ultimately accretes onto the object, leading to no net DF momentum transfer [97].

For extended objects, the minimum impact parameter is given by $0.35\mathcal{M}^{0.6}$ times the characteristic scale of the object, following Ref. [98], which found that this choice led to good agreement of their simulations with the linear result in the subsonic regime. For axion minihalos, we set this scale to be the virial radius, *i.e.*

$$b_{\rm min,\,a} = 0.35\mathcal{M}^{0.6} r_{\rm vir}\,. \tag{A.5}$$

Note that our choice of $b_{\rm min,\,M}$ is appropriate for MACHOs that are smaller than their Bondi-Hoyle-Lyttleton radius: for other compact objects with some known finite extent, it would be better to make the same choice as with axion minihalos instead. The maximum impact parameter is $b_{\rm max} = \mathcal{M} R_J$ [96], where R_J is the Jean's length given by $R_J = c_S\sqrt{\pi/G\,\rho_m} \sim c_s H^{-1}$, with H being the Hubble parameter. $b_{\rm max}$ is roughly the distance traveled by the perturber within the lifetime of the Universe, and so is an appropriate estimate of the size of the wake behind the perturber. This choice is also consistent with what was used in the simulations presented in Refs. [95, 96].

Note that Eq. (A.1), with the definition of $\mathcal{I}$ in Eq. (A.3), was obtained by assuming that density perturbations caused by the perturber are small, and by expanding the fluid equations up to linear order in density. However, the solution for the density perturbations obtained under this assumption is not self-consistent, as the perturbations exceed 1 near the Mach cone for supersonic perturbers. In fact, the density perturbations always diverge on the cone itself. Simulations are therefore necessary to understand if the linear approximation is suitable. Ref. [98] conducted such simulations and made detailed comparisons between simulation results and the linear approximation. They found that in the supersonic regime, the DF force only depended on the quantity $\eta \equiv \mathcal{A}/(\mathcal{M}^2 - 1)$, where $\mathcal{A} \equiv GM/(c_s^2 r_s)$, and r_s is the size of the perturber (taken to be a Plummer sphere in their simulations). For $\eta \leq 2$, the DF force in the linear approximation $F_{\rm lin}$ was found to be in good agreement with the force obtained in the simulation, $F_{\rm sim}$, while for $2 < \eta \leq 100$, they found that the ratio $F_{\rm sim}/F_{\rm lin}$ was well-approximated by a power law,

$$\frac{F_{\rm sim}}{F_{\rm lin}} = \left(\frac{\eta}{2}\right)^{-0.45} . \tag{A.6}$$

For MACHOs, with $r_s = b_{\mathrm{min,\,M}}$, we have $\mathcal{A} = \mathcal{M}^2 + 1$, and

$$\eta_{\mathrm{M}} = \frac{\mathcal{M}^2 + 1}{\mathcal{M}^2 - 1} \,. \tag{A.7}$$

We therefore only expect the difference between F_{sim} and F_{lin} to exceed 50% only when the Mach number lies between $1 < \mathcal{M} \leq 1.1$, corresponding to a very narrow range of redshifts, which we judge to be an acceptable approximation.

For axion minihalos, we have a distribution of halo masses M_h as a function of $M_{h,c}$, with $\mathcal{A} = GM_h/(c^2 r_{\mathrm{vir}})$. We find numerically that for $M_h = 10^6\,\mathrm{M}_\odot$, the ratio $F_{\mathrm{sim}}/F_{\mathrm{lin}}$ can be between 0.25–1 over a range of redshifts $\Delta z/z \sim 1$ around the transition from supersonic to subsonic. Although this is a somewhat large ratio, we compensate for this approximately by only considering the DF force to be acting on halos with a mass below $10^6\,\mathrm{M}_\odot$. Furthermore, by overestimating the drag force, we actually underestimate the heating effect, since such massive halos transition from supersonic to subsonic earlier, typically toward an epoch where baryons were in stronger thermal contact with the CMB, leading to less efficient heating.

We expect that a proper simulation of a population of halos that are constantly decelerating through a baryonic fluid with a time-varying sound speed will produce significantly different results compared to those reported in Ref. [98]. In addition, the deceleration of these objects will significantly alter how baryons fall into potential wells and the formation of the first structures, which again must be simulated. We leave a proper determination of these effects from simulations to future work.

Appendix B

Hardening of Binaries by Primordial Black Holes

A general gravitational interaction between a stellar binary system and a perturber results in the transfer of energy that causes changes in the mutual separation of the binary components. Generally, binaries fall into two broad categories: hard and soft. The nature of energy transfer depends on the type of binary under consideration, as discussed in Section 4.1. On average, soft binaries gain energy from the perturber, and their final orbits widen, with the system becoming less bound (softening further). On the other hand, when the binary system is hard with respect to the perturber, it typically loses energy and becomes more tightly bound. Substantial or repeated softening (for example, by MACHOs) can lead to complete disruption of binaries, and thus, the mere existence of binaries with certain parameters can be used to place constraints on the population of perturbers. The effects of hardening, on the other hand, are more challenging to observe, as we now explain.

The degree of hardening experienced by a binary system is characterized by the hardening rate H, defined by the relation

$$\frac{\mathrm{d}}{\mathrm{d}t}\left(\frac{1}{a}\right) = \frac{G\rho_{\mathrm{obj}}}{\sigma_{\mathrm{obj}}}\, H, \tag{B.1}$$

where ρ_{obj} is the density of the field of perturbing objects and σ_{obj} is their velocity dispersion. We now derive H for a typical binary system in the presence of light PBHs with dispersion σ_{DM} and average density ρ_{PBH} over the binary's trajectory through the Galactic halo. The total energy of the binary is

$$E_{12} = \frac{1}{2}\mu v_{\mathrm{orb}}^2 - \frac{Gm_1 m_2}{r} = -\frac{Gm_1 m_2}{2a}, \tag{B.2}$$

where μ is the reduced mass of the binary system, m_1 and m_2 are the component masses, v_{orb} is the relative velocity of the objects in the binary, and σ_{DM} is the velocity dispersion of the perturbing PBHs.

Now, let us assume that the binary is hard, i.e., with $v_3 \ll w(m_1, m_2)$ for w the critical velocity for hardening as defined by Ref. [174]. We also take the components to have equal mass $m_{\mathrm{c}} \equiv \frac{1}{2}m_{12}$. The energy transfer in an encounter with a PBH of mass m_3 and velocity equal to σ_{DM} is given by

$$\langle \Delta E_{12} \rangle = -\xi \frac{m_3}{2m_{\mathrm{c}}} \frac{Gm_{\mathrm{c}}^2}{2a} = -\xi \frac{m_3}{2m_{\mathrm{c}}} |E_{12}|, \tag{B.3}$$

where ξ is an $\mathcal{O}(1)$ factor determined from N-body simulations [516]. The value of ξ depends upon the initial eccentricity of the binary, the mass ratio of the binary components, and the impact parameter of the perturber. For the case of an equal-mass binary with a circular orbit, $\xi \approx 2$. From eq. (B.3), we can determine the rate at which the binary loses energy over many encounters. Since the number density of PBHs is $n_{\mathrm{PBH}} = \rho_{\mathrm{PBH}}/m_3$, we have

$$\frac{\mathrm{d}E_{12}}{\mathrm{d}t} = \langle \Delta E_{12} \rangle \frac{\mathrm{d}N}{\mathrm{d}t} = -\pi\xi(Gm_{\mathrm{c}})^2 \frac{\rho_{\mathrm{PBH}}}{\sigma_{\mathrm{DM}}}. \tag{B.4}$$

Here, the encounter rate is given by $\mathrm{d}N/\mathrm{d}t = n_{\mathrm{PBH}}\sigma_{\mathrm{DM}}\Sigma_3$, where Σ_3 is the cross section for three-body encounters. This cross section is estimated using gravitational focusing and is given by

$$\Sigma_3 = \frac{2\pi G m_{123} a}{\sigma_{\mathrm{DM}}^2}. \tag{B.5}$$

We can rewrite eq. (B.4) in terms of a as

$$\frac{\mathrm{d}}{\mathrm{d}t}\left(\frac{1}{a}\right) = \frac{G\rho_{\mathrm{PBH}}}{\sigma_{\mathrm{DM}}} H_0, \tag{B.6}$$

so $H_0 = 2\pi\xi$ is the hardening rate induced by slow PBHs with velocity dispersion $\sigma_{\mathrm{DM}} \ll w$. This is not appropriate for a realistic PBH distribution: $w \simeq 0.6 \times v_{\mathrm{orb}}$ for an equal-mass binary, typically well below σ_{DM}. At higher velocities, eq. (B.6) needs to be modified. Following Ref. [174], we define the velocity-dependent hardening rate as

$$H_1\left(v_3\right) = \frac{H_0}{\left[1 + (v_3/w)^4\right]^{1/2}}. \tag{B.7}$$

As the velocity of the PBH increases, the hardening rate decreases and goes as H_0/v_3^2 for $v_3 \gg w$. For a Maxwellian velocity distribution, we finally obtain

$$H = \int_0^\infty \mathrm{d}v_3\, \mathcal{F}_{\mathrm{DM}}(v_3) \frac{\sigma_{\mathrm{DM}}}{v_3}\, H_1(v_3), \tag{B.8}$$

where $\mathcal{F}_{\mathrm{DM}}(v_3)$ is defined in eq. (4.5).

Equation (B.8) gives the appropriate hardening rate for a binary system in a homogeneous environment of low-mass PBHs with a velocity dispersion typical of DM.

However, the hardening rate is dominated by perturbers with v_3 not much greater than w, for which H_1 is approximately independent of a. In this case, eq. (B.6) gives $\mathrm{d}a/\mathrm{d}t \propto a^2$, and the semimajor axis thus evolves at a characteristic rate

$$\left|\frac{1}{a}\frac{\mathrm{d}a}{\mathrm{d}t}\right| \simeq \frac{2\pi\xi G\rho_{\mathrm{PBH}}a}{\sigma_{\mathrm{DM}}} \approx 0.01\,\mathrm{Gyr}^{-1}\left(\frac{a}{10^6\,\mathrm{AU}}\right), \tag{B.9}$$

where we take fiducial values $\xi = 2$, $\sigma_{\mathrm{DM}} = 220\,\mathrm{km/s}$, and $\rho_{\mathrm{PBH}} = 0.4\,\mathrm{GeV/cm^3}$. This estimate already indicates that hardening due to PBHs is potentially observable only for the widest binaries.

Furthermore, while these light PBHs harden a given binary, that same binary is subject to softening due to encounters with ordinary stellar objects when it transits through the Galactic disk. The change in energy of the binary per unit time due to multiple encounters with stellar objects is [228]

$$\frac{\mathrm{d}E_{12}}{\mathrm{d}t} = 8\sqrt{\frac{\pi}{3}}\frac{G^2 m_{\mathrm{c}} m_\star \rho_\star}{\sigma_\star}\log\Lambda, \tag{B.10}$$

where $m_\star$ is the mass of each stellar object, $\rho_\star$ is their average density, and $\sigma_\star$ is their velocity dispersion. Here $\log\Lambda = \log(b_{\mathrm{max}}/b_{\mathrm{min}})$ is the Coulomb logarithm, with b_{min} and b_{max} denoting the minimal and maximal impact parameters, respectively. We fix $b_{\mathrm{min}} = G(m_{\mathrm{c}} + m_\star)/\langle v_\star^2\rangle$, where $v_\star$ is the relative velocity between stars and the center of mass of the binary, and we approximate $\langle v_\star^2\rangle = (2.1\sigma_\star)^2$ [344]. To ensure eq. (B.10) is valid, the impact parameter should be much smaller than the binary star separation, such that the change of velocity of the distant binary component is negligible. Therefore, we set $b_{\max} = a/2$, and include a factor of 2 to account for interactions with either of the binary components.

The softening rate S due to stellar encounters is defined similarly to the hardening rate:

$$\frac{\mathrm{d}}{\mathrm{d}t}\left(\frac{1}{a}\right) = -\frac{G\rho_\star}{\sigma_\star}S. \tag{B.11}$$

From eq. (B.11), we identify the softening rate as $S = 16\sqrt{\pi/3}\log\Lambda$, with $\Lambda = 2.2a\sigma_\star^2/[G(m_\mathrm{c}+m_\star)]$. For simplicity, we now assume that all stars have the same mass as the binary components, $m_\star = m_\mathrm{c}$. To minimize the softening, we also assume that the trajectory of the binary is such that it is outside of the Galactic disk for much of its orbit, spending a fractional time x in a star-rich environment. Neglecting the weak dependence of softening on a, and given some initial separation a_0, the separation of a typical binary after a time t will be determined by a combination of softening and hardening effects:

$$a(t) = \left[a_0^{-1} + \frac{G\rho_\mathrm{PBH}}{\sigma_\mathrm{DM}}Ht - \frac{G\rho_\star}{\sigma_\star}Sxt\right]^{-1}. \tag{B.12}$$

The impact of hardening by low-mass PBHs is only non-negligible if the hardening term in eq. (B.12) is at least as large as the softening term. For a binary with a semimajor axis of 10^5 AU, we find that in order for the hardening term to exceed the softening term, we must have

$$H \gtrsim 900 \left(\frac{\sigma_{\rm DM}}{220\,{\rm km/s}}\right) \left(\frac{\rho_{\rm PBH}}{0.4\,{\rm GeV/cm^3}}\right)^{-1} \left(\frac{x}{0.1}\right) \left(\frac{\rho_\star}{2.2\,{\rm GeV/cm^3}}\right) \left(\frac{\sigma_\star}{25\,{\rm km/s}}\right)^{-1}, \tag{B.13}$$

where we take the stellar density from Ref. [517, 518] and the stellar velocity dispersion from Ref. [519]. However, for the same parameter values, eq. (B.8) implies a much smaller value of $H = 1.1 \times 10^{-5}$. Therefore, in the Milky Way, softening always dominates over hardening due to the high velocity dispersion of DM, making hardening from low-mass PBHs extremely difficult to study.

Appendix C

Dark Charged Black Holes

In this appendix, we discuss the existence of black holes with dark charge. Several mechanisms of endowing black holes with long-lived charge content are mentioned by the authors of [520, 310] - one interesting possibility is to introduce millicharged fermions in the dark sector [328]. Denoting the mass of the SMBH by M_2 and its charge by Q_2, one can obtain $Q_2/M_2 \sim 1$ by choosing the charge-to-mass ratio of dark fermions to be ~ 1 (close to the limit imposed by the weak gravity conjecture). In this case, one could consider a SMBH-brown dwarf XMRI system (where the brown dwarf is the uncharged Object A alluded to above) which determines the mass of the SMBH; concurrently, a SMBH-black hole EMRI system (where the stellar black hole is the dark-charged Object B) constrains the light mediator mass. We outline the model below.

Our model will consist of a millicharged dark fermion χ with charge q_χ and mass m_χ, interacting by the exchange of a vector mediator V_μ. The Lagrangian is

$$\mathcal{L} = -\frac{1}{4}V_{\mu\nu}V^{\mu\nu} + \frac{1}{2}m_V^2 V_\mu V^\mu + \bar{\chi}(i\gamma_\mu D^\mu - m_\chi)\chi \ . \tag{C.1}$$

Here, the covariant derivative is given by $D_\mu = \nabla_\mu + iq_\chi V_\mu$, and we normalize the dark fine structure constant $\alpha' = 1$. For comparison, [311] sets $q_\chi = 1$. The total charge of the SMBH can then be written as

$$Q_2 \;=\; N_2 q_\chi \;, \tag{C.2}$$

where N_2 gives the number of fermions of opposite charge it needs to accrete to become neutral. We now discuss in turn estimates of the discharge time for a dark charged black hole, and then how it could acquire dark charge in the first place. These issues all hinge on the possibility that a charge q_χ with mass m_χ is able to be absorbed by a black hole with charge Q and mass M. A simple (classical) comparison of the associated gravitational attraction and possible dark repulsion yields the condition

$$q_\chi Q \;\sim\; m_\chi M \quad \Rightarrow \quad \frac{Q}{M} \sim \frac{m_\chi}{q_\chi} \;. \tag{C.3}$$

In the Standard Model, this condition is badly violated unless $Q \sim 0$. However, for a dark sector with

$$m_\chi \;\sim\; m_p, \quad \text{and} \quad q_\chi \;\sim\; 10^{-18}\, e \tag{C.4}$$

where e is the charge of the electron and m_p is the mass of a proton, one can obtain $Q \sim M$.

Assuming that the SMBH is in an environment with density ρ of oppositely charged dark fermions moving with velocity v, and that the accretion follows the Bondi rate for collisionless fluid, [328] estimates the discharge time to be

$$\tau_{\rm discharge} \;\sim\; \left(\frac{v}{220\,{\rm km/s}}\right)^3 \left(\frac{0.4\,{\rm GeV/cm^3}}{\rho}\right) \left(\frac{10 M_\odot}{M_2}\right) \left(\frac{m_\chi}{m_p}\right) \left(\frac{e}{q_\chi}\right)\; {\rm yr}\;. \tag{C.5}$$

With the choice of dark sector parameters given in Eq. (C.4), this results in a large discharge time. Another choice of the mass and charge could be $m_\chi \sim 10^{-3} m_p$ and $q_\chi \sim 10^{-21}\, e$, which leaves the discharge time unchanged. If the black hole is located in an environment where $\rho \sim 0$, the discharge time can be even longer. We note that the above estimate for the discharge time assumes an accretion rate given by

$$\frac{dM_2}{dt} \sim M_2^2 Q_\rho \,, \tag{C.6}$$

where $Q_\rho \sim \rho/v^3$ is the dark fermion phase space density [521]. Moreover, it assumes that the entire density ρ is constituted by oppositely charged dark fermions, which is the most conservative assumption.

The question of how a SMBH can acquire dark charge in the first place is a difficult one and is tied to the formation mechanism of SMBHs, which is unknown. It may be easier to answer this question for the case of stellar black holes first. Classic calculations [522] indicate that the charge of a typical star at birth may be given by

$$\left(\frac{Q}{M}\right)_{\rm birth} \sim \frac{m_\chi}{q_\chi} \tag{C.7}$$

under the assumption that the black hole is formed by the collapse of dark charged particles. For the Standard Model, the charge obtained from Eq. (C.7) is minuscule and is promptly discharged as well. For dark sectors with $\frac{m_\chi}{q_\chi} \sim 1$, however, one can obtain $\left(\frac{Q}{M}\right)_{\rm birth} \sim 1$, and the discharge time can also be large.

For an SMBH, the situation is less clear. The proliferation of SMBH observations with $z > 5$ raises the question about their origin, which is a mystery (we refer to [523] for a review). One possibility is the existence of intermediate mass black hole seeds with $M_2 \sim 10^{3-5} M_\odot$ at $z \sim 20$, along with a population of stellar black holes. If these SMBH seeds are formed from the collapse of a dark matter halo, calculations similar to the one sketched above may apply to their initial charge. The subsequent accretion history of the seed is expected to follow mean Eddington rates with episodes of super-Eddington accretion [524, 525, 526, 527]:

$$M_2(t) \sim M_{\rm seed} \times e^{t/\tau_{\rm Edd}} , \tag{C.8}$$

where $\tau_{\rm Edd} = 45$ Myr is the Eddington timescale. Accretion under these circumstances can grow $\sim \mathcal{O}(10 - 100) M_\odot$ seeds into black holes with mass $\sim 10^3 M_\odot$ by $z = 18$ and $\sim 10^8 M_\odot$ by $z = 7$.

Assuming that the growth of the black hole mass between $z \sim 30$ to $z \sim 7$ proceeds by the accretion of equal numbers of positively and negatively charged dark particles, the final charge of the SMBH would be equal to the initial charge, while the mass is enhanced by orders of magnitude. This would yield, for example, $(Q/M)_{\rm final} \sim 10^{-5}$, assuming that $(Q/M)_{\rm birth} \sim 1$. On the other hand, preferential accretion of one charge over the other could produce $(Q/M)_{\rm final} \sim 1$.

Appendix D

Dark Matter–Electron Scattering

In this section, we derive the differential scattering cross-section for a dark matter particle χ scattering elastically from an electron,

$$\chi(p) + e(k) \to \chi(p') + e(k'). \tag{D.1}$$

We assume that the interaction is mediated by a vector boson V exchanged in the t channel, as shown in Fig. D.1. The vector mediator couples to the dark sector with coupling g_{12} and to the electromagnetic current through kinetic mixing, with an effective coupling ϵe. Throughout this section, we use natural units, $\hbar = c = 1$. The matrix element is

$$\begin{aligned} i\mathcal{M} &= \bar{u}^{s'}(p')(-ig_{12}\gamma^{\mu})u^{s}(p)\left(\frac{-ig_{\mu\nu}}{t - m_V^2}\right)\bar{u}^{r'}(k')(-i\epsilon e\gamma^{\nu})u^{r}(k), \\ &= \frac{i\epsilon e g_{12}}{t - m_V^2}\left[\bar{u}^{s'}(p')\gamma^{\mu}u^{s}(p)\right]\left[\bar{u}^{r'}(k')\gamma_{\mu}u^{r}(k)\right], \end{aligned} \tag{D.2}$$

where m_V is the mediator mass and

$$t = (p - p')^2 = (k' - k)^2 \tag{D.3}$$

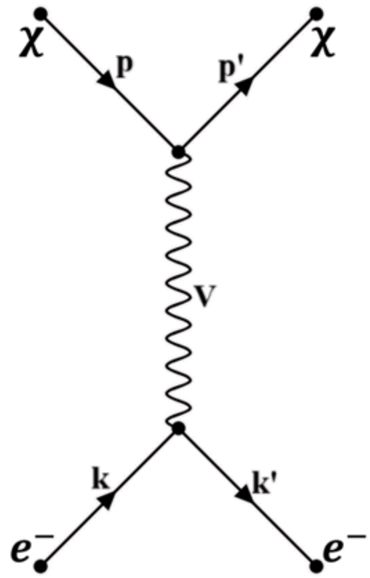

Figure D.1: Feynman diagram for Dark matter–electron scattering through the t-channel exchange of a vector mediator V.

is the Mandelstam variable. The squared matrix element is therefore

$$|\mathcal{M}|^2 = \frac{\epsilon^2 e^2 g_{12}^2}{(t-m_V^2)^2}\left[\bar{u}(p')\gamma^\mu u(p)\bar{u}(p)\gamma^\nu u(p')\right]\left[\bar{u}(k')\gamma_\mu u(k)\bar{u}(k)\gamma_\nu u(k')\right]. \tag{D.4}$$

For unpolarized scattering, we average over the two initial spins of the dark matter particle and the electron, giving

$$\overline{|\mathcal{M}|^2} = \frac{1}{4}\frac{\epsilon^2 e^2 g_{12}^2}{(t-m_V^2)^2}\sum_{s,s',r,r'}\left[\bar{u}^{s'}(p')\gamma^\mu u^s(p)\bar{u}^s(p)\gamma^\nu u^{s'}(p')\right]\left[\bar{u}^{r'}(k')\gamma_\mu u^r(k)\bar{u}^r(k)\gamma_\nu u^{r'}(k')\right]. \tag{D.5}$$

The spin sums are performed using the completeness relations

$$\sum_s u^s(p)\bar{u}^s(p) = \not{p} + m, \tag{D.6}$$

$$\sum_s v^s(p)\bar{v}^s(p) = \not{p} - m, \tag{D.7}$$

where $\not{p} = \gamma^\mu p_\mu$. Applying these identities to the dark matter current gives

$$\sum_{s,s'} \bar{u}^{s'}(p')\gamma^\mu u^s(p)\bar{u}^s(p)\gamma^\nu u^{s'}(p') = \mathrm{Tr}\left[(\not{p}' + m_\chi)\gamma^\mu(\not{p} + m_\chi)\gamma^\nu\right]. \tag{D.8}$$

Similarly, for the electron current,

$$\sum_{r,r'} \bar{u}^{r'}(k')\gamma_\mu u^r(k)\bar{u}^r(k)\gamma_\nu u^{r'}(k') = \mathrm{Tr}\left[(\not{k}' + m_e)\gamma_\mu(\not{k} + m_e)\gamma_\nu\right]. \tag{D.9}$$

Thus,

$$\overline{|\mathcal{M}|^2} = \frac{1}{4}\frac{\epsilon^2 e^2 g_{12}^2}{(t - m_V^2)^2}\,\mathrm{Tr}\left[(\not{p}' + m_\chi)\gamma^\mu(\not{p} + m_\chi)\gamma^\nu\right]\mathrm{Tr}\left[(\not{k}' + m_e)\gamma_\mu(\not{k} + m_e)\gamma_\nu\right]. \tag{D.10}$$

Using the fact that traces with an odd number of gamma matrices vanish, the dark matter trace becomes

$$\mathrm{Tr}\left[(\not{p}' + m_\chi)\gamma^\mu(\not{p} + m_\chi)\gamma^\nu\right] = \mathrm{Tr}\left[\not{p}'\gamma^\mu\not{p}\gamma^\nu\right] + m_\chi^2\,\mathrm{Tr}\left[\gamma^\mu\gamma^\nu\right]. \tag{D.11}$$

The required trace identities are

$$\mathrm{Tr}\left[\gamma^\mu\gamma^\nu\right] = 4g^{\mu\nu}, \tag{D.12}$$

$$\mathrm{Tr}\left[\gamma^\mu\gamma^\nu\gamma^\rho\gamma^\sigma\right] = 4\left(g^{\mu\nu}g^{\rho\sigma} - g^{\mu\rho}g^{\nu\sigma} + g^{\mu\sigma}g^{\nu\rho}\right). \tag{D.13}$$

Therefore,

$$\mathrm{Tr}\left[(\not{p}' + m_\chi)\gamma^\mu(\not{p} + m_\chi)\gamma^\nu\right] = 4\left[p'^\mu p^\nu + p'^\nu p^\mu - g^{\mu\nu}(p'\cdot p - m_\chi^2)\right]. \tag{D.14}$$

Similarly,

$$\mathrm{Tr}\left[(\not{k}' + m_e)\gamma_\mu(\not{k} + m_e)\gamma_\nu\right] = 4\left[k'_\mu k_\nu + k'_\nu k_\mu - g_{\mu\nu}(k'\cdot k - m_e^2)\right]. \tag{D.15}$$

Substituting Eqs. (D.14) and (D.15) into Eq. (D.10), we find

$$\overline{|\mathcal{M}|^2} = 4\frac{\epsilon^2 e^2 g_{12}^2}{(t - m_V^2)^2}\left[p'^\mu p^\nu + p'^\nu p^\mu - g^{\mu\nu}(p'\cdot p - m_\chi^2)\right]\left[k'_\mu k_\nu + k'_\nu k_\mu - g_{\mu\nu}(k'\cdot k - m_e^2)\right]. \tag{D.16}$$

Contracting the Lorentz indices gives

$$\begin{aligned}\overline{|\mathcal{M}|^2} = 8\frac{\epsilon^2 e^2 g_{12}^2}{(t - m_V^2)^2}\Big[&(p'\cdot k')(p\cdot k) + (p'\cdot k)(p\cdot k') - (p\cdot p')(k\cdot k' - m_e^2)\\ &- (k'\cdot k)(p'\cdot p - m_\chi^2) + 2(p'\cdot p - m_\chi^2)(k'\cdot k - m_e^2)\Big].\end{aligned} \tag{D.17}$$

In the laboratory frame, where the initial electron is at rest, the four-momenta are

$$p^\mu = \begin{pmatrix} E_\chi \\ \\ \vec{p} \end{pmatrix}, \qquad k^\mu = \begin{pmatrix} m_e \\ \\ \vec{0} \end{pmatrix}, \qquad p'^\mu = \begin{pmatrix} E'_\chi \\ \\ \vec{p}\,' \end{pmatrix}, \qquad k'^\mu = \begin{pmatrix} E'_e \\ \\ \vec{k}\,' \end{pmatrix}. \quad \text{(D.18)}$$

Here E_χ and E'_χ are the initial and final dark matter energies, while E'_e is the total energy of the recoiling electron. The electron recoil kinetic energy is

$$E_{R,e} = E'_e - m_e. \quad \text{(D.19)}$$

The Mandelstam variable t can be written as

$$\begin{aligned} t &= (p - p')^2 = (k' - k)^2 \\ &= k'^2 + k^2 - 2k' \cdot k = 2m_e^2 - 2m_e E'_e \\ &= -2m_e E_{R,e}. \end{aligned} \quad \text{(D.20)}$$

Four-momentum conservation gives

$$p + k = p' + k'. \quad \text{(D.21)}$$

Squaring both sides of Eq. (D.21), we obtain

$$p \cdot k = p' \cdot k'. \quad \text{(D.22)}$$

Similarly, rewriting Eq. (D.21) as $p - k' = p' - k$ gives

$$p \cdot k' = p' \cdot k. \tag{D.23}$$

In the laboratory frame,

$$p \cdot k = m_e E_\chi, \qquad p' \cdot k = m_e E'_\chi. \tag{D.24}$$

Energy conservation implies

$$E_\chi + m_e = E'_\chi + E'_e, \qquad E'_\chi = E_\chi - E_{R,e}. \tag{D.25}$$

We also need the scalar product $p \cdot p'$. Using $p - p' = k' - k$, we find

$$\begin{aligned} p^2 + p'^2 - 2p \cdot p' &= k'^2 + k^2 - 2k' \cdot k, \\ p \cdot p' - m_\chi^2 &= k' \cdot k - m_e^2. \end{aligned} \tag{D.26}$$

Since $k' \cdot k = m_e E'_e$, this becomes

$$p \cdot p' - m_\chi^2 = m_e E_{R,e}. \tag{D.27}$$

Substituting the laboratory-frame identities into Eq. (D.17), the spin-averaged squared amplitude can be written as

$$\overline{|\mathcal{M}|^2} = 8\frac{\epsilon^2 e^2 g_{12}^2 m_e}{\left(2m_e[m_e - E_e'] - m_V^2\right)^2}\left[m_e\left\{E_\chi^2 + (m_e + E_\chi - E_e')^2\right\} + (m_e^2 + m_\chi^2)(m_e - E_e')\right]. \tag{D.28}$$

Equivalently, in terms of the electron recoil kinetic energy $E_{R,e}$,

$$\overline{|\mathcal{M}|^2} = 8\frac{\epsilon^2 e^2 g_{12}^2 m_e}{\left(2m_e E_{R,e} + m_V^2\right)^2}\left[m_e\left\{E_\chi^2 + (E_\chi - E_{R,e})^2\right\} - (m_e^2 + m_\chi^2)E_{R,e}\right]. \tag{D.29}$$

Finally, the differential cross-section in the laboratory frame is

$$\frac{d\sigma}{dE_{R,e}} = \frac{m_e}{8\pi\lambda(s, m_e^2, m_\chi^2)}\overline{|\mathcal{M}|^2}, \tag{D.30}$$

where

$$\lambda(a,b,c) = a^2 + b^2 + c^2 - 2ab - 2ac - 2bc \tag{D.31}$$

is the Källén function. Therefore,

$$\frac{d\sigma}{dE_{R,e}} = \frac{\epsilon^2 e^2 g_{12}^2 m_e^2}{\pi\lambda(s, m_e^2, m_\chi^2)\left(2m_e E_{R,e} + m_V^2\right)^2}\left[m_e\left\{E_\chi^2 + (E_\chi - E_{R,e})^2\right\} - (m_e^2 + m_\chi^2)E_{R,e}\right]. \tag{D.32}$$

Bibliography

[1] G. Bertone and D. Hooper, *Rev. Mod. Phys.* 90 (2018).

[2] M. Cirelli, A. Strumia, et al., arXiv: `2406.01705 [hep-ph]` (2024).

[3] T.-T. Yu, arXiv: `2506.05234 [hep-ph]` (2025).

[4] J. Cooley et al., arXiv: `2209.07426 [hep-ph]` (2022).

[5] F. Zwicky, *General Relativity and Gravitation* 41 (2009).

[6] V. C. Rubin and W. K. Ford Jr., ApJ 159 (1970).

[7] J. P. Ostriker and P. J. E. Peebles, ApJ 186 (1973).

[8] I. D. Zel'dovich Ya.B.; Novikov, *Soviet Astron. AJ (Engl. Transl.),* 10 (1967).

[9] S. Hawking, MNRAS 152 (1971).

[10] B. Carr and F. Kuhnel, *Ann. Rev. Nucl. Part. Sci.* 70 (2020).

[11] G. Jungman, M. Kamionkowski, et al., *Phys. Rept.* 267 (1996).

[12] D. S. Akerib et al., *Nucl. Instrum. Meth. A* 953 (2020).

[13] E. Aprile et al., *Eur. Phys. J. C* 84 (2024).

[14] A. Abdukerim et al., *Sci. China Phys. Mech. Astron.* 68 (2025).

[15] D. S. Akerib et al., arXiv: `2203.08084 [hep-ex]` (2022).

[16] A. Mitridate, T. Trickle, et al., *Phys. Dark Univ.* 40 (2023).

[17] R. Essig et al., arXiv: `2203.08297 [hep-ph]` (2022).

[18] D. Carney et al., *SciPost Phys. Core* 6 (2023).

[19] S. Weinberg, *Phys. Rev. Lett.* 40 (1978).

[20] F. Wilczek, *Phys. Rev. Lett.* 40 (1978).

[21] Ciaran O'Hare (2024).

[22] P. Svrcek and E. Witten, *JHEP* 06 (2006).

[23] A. Ringwald, *J. Phys. Conf. Ser.* 3162 (2025).

[24] C. B. Adams et al., arXiv: `2203.14923 [hep-ex]` (2022).

[25] B. Bhalla, B. V. Lehmann, et al., *Phys. Rev. D* 113 (2026).

[26] B. Bhalla, B. V. Lehmann, et al., *Phys. Rev. D* 111 (2025).

[27] B. Bhalla, A. Ireland, et al., arXiv: `2512.00169 [astro-ph.CO]` (2025).

[28] B. Bhalla, F. Hajkarim, et al., arXiv: `2506.15765 [hep-ph]` (2025).

[29] B. Bhalla, K. Sinha, et al., *JCAP* 09 (2024).

[30] A. M. Green and B. J. Kavanagh, *J. Phys. G* 48 (2021).

[31] R. Ruffini and S. Bonazzola, *Phys. Rev.* 187 (1969).

[32] S. L. Liebling and C. Palenzuela, *Living Rev. Rel.* 26 (2023).

[33] J. H. Chang, P. J. Fox, et al., *JCAP* 08 (2024).

[34] E. Witten, *Phys. Rev. D* 30 (1984).

[35] Y. Bai, A. J. Long, et al., *Phys. Rev. D* 99 (2019).

[36] A. Kusenko and M. E. Shaposhnikov, *Phys. Lett. B* 418 (1998).

[37] J.-P. Hong, S. Jung, et al., *Phys. Rev. D* 102 (2020).

[38] M. Escudero, C. K. Pooni, et al., arXiv: `2302.10206 [hep-ph]` (2023).

[39] P. J. Fox, N. Weiner, et al., *Phys. Rev. D* 108 (2023).

[40] P. J. Fox, N. Weiner, et al., arXiv: `2508.08371 [hep-ph]` (2025).

[41] M. Ricotti, J. P. Ostriker, et al., *Astrophys. J.* 680 (2008).

[42] Y. Ali-Haïmoud and M. Kamionkowski, *Phys. Rev. D* 95 (2017).

[43] P. Lu, V. Takhistov, et al., *Astrophys. J. Lett.* 908 (2021).

[44] V. Takhistov, P. Lu, et al., *JCAP* 03 (2022).

[45] T. Kim, P. Lu, et al., arXiv: `2508.18344 [hep-ph]` (2025).

[46] C. Alcock et al., *Astrophys. J.* 542 (2000).

[47] P. Tisserand et al., *Astron. Astrophys.* 469 (2007).

[48] A. Udalski, M. K. Szymański, et al., *Acta Astron.* 65 (2015).

[49] T. Blaineau et al., *Astron. Astrophys.* 664 (2022).

[50] T. D. Brandt, *Astrophys. J. Lett.* 824 (2016).

[51] D. Wadekar and Z. Wang, *Phys. Rev. D* 107 (2023).

[52] P. W. Graham and H. Ramani, arXiv: `2311.07654 [hep-ph]` (2023).

[53] P. W. Graham and H. Ramani, *Phys. Rev. D* 110 (2024).

[54] P. W. Graham, H. Ramani, et al., arXiv: `2510.01310 [hep-ph]` (2025).

[55] E. C. Ostriker, *The Astrophysical Journal* 513 (1999).

[56] D. Tseliakhovich and C. Hirata, *Phys. Rev. D* 82 (2010).

[57] J. B. Muñoz, E. D. Kovetz, et al., *Phys. Rev. D* 92 (2015).

[58] J. B. Muñoz and A. Loeb, *JCAP* 11 (2017).

[59] A. Fialkov, R. Barkana, et al., *Phys. Rev. Lett.* 121 (2018).

[60] R. Barkana, *Nature* 555 (2018).

[61] J. B. Muñoz and A. Loeb, *Nature* 557 (2018).

[62] R. Barkana, N. J. Outmezguine, et al., *Phys. Rev. D* 98 (2018).

[63] J. B. Muñoz, C. Dvorkin, et al., *Phys. Rev. Lett.* 121 (2018).

[64] H. Liu, N. J. Outmezguine, et al., *Phys. Rev. D* 100 (2019).

[65] R. Barkana, A. Fialkov, et al., *Phys. Rev. D* 108 (2023).

[66] C. Dvorkin, K. Blum, et al., *Phys. Rev. D* 89 (2014).

[67] K. K. Boddy, V. Gluscevic, et al., *Phys. Rev. D* 98 (2018).

[68] T. R. Slatyer and C.-L. Wu, *Phys. Rev. D* 98 (2018).

[69] W. L. Xu, C. Dvorkin, et al., *Phys. Rev. D* 97 (2018).

[70] E. O. Nadler et al., *Phys. Rev. Lett.* 126 (2021).

[71] M. A. Buen-Abad, R. Essig, et al., *Phys. Rept.* 961 (2022).

[72] D. V. Nguyen, D. Sarnaaik, et al., *Phys. Rev. D* 104 (2021).

[73] N. Dalal, U.-L. Pen, et al., *JCAP* 11 (2010).

[74] Y. Ali-Haımoud, P. D. Meerburg, et al., *Phys. Rev. D* 89 (2014).

[75] J. B. Muñoz, *Phys. Rev. D* 100 (2019).

[76] C. Evoli, A. Mesinger, et al., *JCAP* 11 (2014).

[77] L. Lopez-Honorez, O. Mena, et al., *JCAP* 08 (2016).

[78] G. Facchinetti, L. Lopez-Honorez, et al., *JCAP* 01 (2024).

[79] Y. Sun, J. W. Foster, et al., *Phys. Rev. D* 111 (2025).

[80] Y. Sun, J. W. Foster, et al., arXiv: `2509.22772 [hep-ph]` (2025).

[81] D. Agius, R. Essig, et al., arXiv: `2510.14877 [astro-ph.CO]` (2025).

[82] T. C. Voytek, A. Natarajan, et al., *Astrophys. J. Lett.* 782 (2014).

[83] L. Philip et al., *Journal of Astronomical Instrumentation* 8 (2019).

[84] E. de Lera Acedo et al., *Nature Astron.* 6 (2022).

[85] L. M. Berkhout et al., *PASP* 136 (2024).

[86] A. Weltman et al., *Publ. Astron. Soc. Austral.* 37 (2020).

[87] M. G. Labate, M. Waterson, et al., *Journal of Astronomical Telescopes* 8 (2022).

[88] V. M. Mehta, M. Demirtas, et al., arXiv: `2011.08693 [hep-th]` (2020).

[89] M. Baryakhtar, M. Galanis, et al., *Phys. Rev. D* 103 (2021).

[90] C. Ünal, F. Pacucci, et al., *JCAP* 05 (2021).

[91] S. Hoof, D. J. E. Marsh, et al., *Mon. Not. Roy. Astron. Soc.* (2025).

[92] S. J. Witte and A. Mummery, *Phys. Rev. D* 111 (2025).

[93] A. Just, W. H. Kegel, et al., *A&A* 164 (1986).

[94] A. Just and W. H. Kegel, *A&A* 232 (1990).

[95] M. McQuinn and R. M. O'Leary, *ApJ* 760 (2012).

[96] R. M. O'Leary and M. McQuinn, *ApJ* 760 (2012).

[97] T. Suzuguchi, K. Sugimura, et al., *Astrophys. J.* 966 (2024).

[98] H. Kim and W.-T. Kim, *The Astrophysical Journal* 703 (2009).

[99] C. Conroy and J. P. Ostriker, *The Astrophysical Journal* 681 (2008).

[100] W.-T. Kim, A. A. El-Zant, et al., *The Astrophysical Journal* 632 (2005).

[101] P. J. E. Peebles, *ApJ* 153 (1968).

[102] Y. B. Zeldovich, V. G. Kurt, et al. (1968).

[103] H. Liu, G. W. Ridgway, et al., *Phys. Rev. D* 101 (2020).

[104] I. Reis, A. Fialkov, et al., *Mon. Not. Roy. Astron. Soc.* 506 (2021).

[105] X.-L. Chen and J. Miralda-Escude, *Astrophys. J.* 602 (2004).

[106] L. Chuzhoy and P. R. Shapiro, *Astrophys. J.* 651 (2006).

[107] S. Furlanetto and J. R. Pritchard, *Mon. Not. Roy. Astron. Soc.* 372 (2006).

[108] T. Venumadhav, L. Dai, et al., *Phys. Rev. D* 98 (2018).

[109] C. J. Hogan and M. J. Rees, *Phys. Lett. B* 205 (1988).

[110] E. W. Kolb and I. I. Tkachev, *Phys. Rev. Lett.* 71 (1993).

[111] E. W. Kolb and I. I. Tkachev, *Astrophys. J. Lett.* 460 (1996).

[112] E. Hardy, *JHEP* 02 (2017).

[113] H. Fukunaga, N. Kitajima, et al., *JCAP* 02 (2021).

[114] A. Arvanitaki, S. Dimopoulos, et al., *Phys. Rev. D* 101 (2020).

[115] R. T. Co, L. J. Hall, et al., *Phys. Rev. Lett.* 124 (2020).

[116] C. Eröncel, R. Sato, et al., *JCAP* 10 (2022).

[117] C. Eröncel and G. Servant, arXiv: `2207.10111 [hep-ph]` (2022).

[118] W. H. Press and P. Schechter, *ApJ* 187 (1974).

[119] J. Enander, A. Pargner, et al., *JCAP* 12 (2017).

[120] B. Eggemeier, J. Redondo, et al., *Phys. Rev. Lett.* 125 (2020).

[121] D. Ellis, D. J. E. Marsh, et al., *Phys. Rev. D* 103 (2021).

[122] H. Xiao, I. Williams, et al., *Phys. Rev. D* 104 (2021).

[123] S. Murray, C. Power, et al., *Astron. Comput.* 3-4 (2013).

[124] E. D. Ramirez and M. R. Buckley, *Mon. Not. Roy. Astron. Soc.* 525 (2023).

[125] H. Zhou, Y. Lian, et al., *Mon. Not. Roy. Astron. Soc.* 513 (2022).

[126] M. Oguri, J. M. Diego, et al., *Phys. Rev. D* 97 (2018).

[127] J. S. Reynés, J. H. Matthews, et al., *Mon. Not. Roy. Astron. Soc.* 510 (2021).

[128] O. Ning and B. R. Safdi, *Phys. Rev. Lett.* 134 (2025).

[129] M. C. D. Marsh, H. R. Russell, et al., *JCAP* 12 (2017).

[130] E. Müller, F. Calore, et al., *JCAP* 07 (2023).

[131] M. Ajello et al., *Phys. Rev. Lett.* 116 (2016).

[132] C. S. Reynolds, M. C. D. Marsh, et al., *Astrophys. J.* 890 (2020).

[133] K. Harigaya, W. Hu, et al., *Phys. Rev. D* 112 (2025).

[134] R. Murgia, G. Scelfo, et al., *Phys. Rev. Lett.* 123 (2019).

[135] C. O'Hare (2020).

[136] R. Barkana, *Phys. Rept.* 645 (2016).

[137] J. B. Muñoz, *Mon. Not. Roy. Astron. Soc.* 523 (2023).

[138] B. Zygelman, *ApJ* 622 (2005).

[139] S. Furlanetto and M. Furlanetto, *Mon. Not. Roy. Astron. Soc.* 374 (2007).

[140] S. Furlanetto and M. Furlanetto, *Mon. Not. Roy. Astron. Soc.* 379 (2007).

[141] J. Burns et al., arXiv: `2103.05085 [astro-ph.CO]` (2021).

[142] C. D. Brinkerink et al., *arXiv e-prints* (2025).

[143] J. de Swart, G. Bertone, et al., *Nature Astron.* 1 (2017).

[144] H. Baer, V. Barger, et al., *Eur. Phys. J. ST* 229 (2020).

[145] G. Arcadi, M. Dutra, et al., *Eur. Phys. J. C* 78 (2018).

[146] G. Arcadi, D. Cabo-Almeida, et al., *Eur. Phys. J. C* 85 (2025).

[147] M. Baryakhtar et al., arXiv: `2203.07984 [hep-ph]` (2022).

[148] S. R. Coleman, *Nucl. Phys. B* 262 (1985).

[149] P. Jetzer, *Phys. Rept.* 220 (1992).

[150] S. Hawking, *Mon. Not. Roy. Astron. Soc.* 152 (1971).

[151] B. J. Carr and S. W. Hawking, *Mon. Not. Roy. Astron. Soc.* 168 (1974).

[152] B. Carr, F. Kuhnel, et al., *Phys. Rev. D* 94 (2016).

[153] A. M. Green, *Nucl. Phys. B* 1003 (2024).

[154] B. Carr, S. Clesse, et al., *Phys. Rept.* 1054 (2024).

[155] M. Gorton and A. M. Green, arXiv: `2403.03839 [astro-ph.CO]` (2024).

[156] H. Niikura et al., *Nature Astron.* 3 (2019).

[157] S. Sugiyama, T. Kurita, et al., *Mon. Not. Roy. Astron. Soc.* 493 (2020).

[158] N. Smyth, S. Profumo, et al., *Phys. Rev. D* 101 (2020).

[159] S. Clesse and J. García-Bellido, *Phys. Dark Univ.* 22 (2018).

[160] S. Van den Bergh, Nature 224 (1969).

[161] T. X. Tran, S. R. Geller, et al., *Phys. Rev. D* 110 (2024).

[162] B. Bertrand, M. Cuadrat-Grzybowski, et al., arXiv: `2312.14520` (2023).

[163] V. Thoss and A. Burkert, *Astrophys. J.* 980 (2025).

[164] B. V. Lehmann, A. Webber, et al., *JCAP* 08 (2022).

[165] V. A. De Lorenci, D. I. Kaiser, et al., arXiv: `2504.07517 [gr-qc]` (2025).

[166] J. Peñarrubia, S. E. Koposov, et al., arXiv: `1005.5388 [astro-ph.GA]` (2010).

[167] J. Peñarrubia, A. D. Ludlow, et al., *Mon. Not. Roy. Astron. Soc.* 461 (2016).

[168] D. P. Quinn, M. I. Wilkinson, et al., MNRAS 396 (2009).

[169] E. Tyler, A. M. Green, et al., *Mon. Not. Roy. Astron. Soc.* 524 (2023).

[170] S. Chandrasekhar, *Astrophys. J.* 97 (1943).

[171] A. Caputo, J. Zavala, et al., *Phys. Dark Univ.* 19 (2018).

[172] D. C. Heggie, *Mon. Not. Roy. Astron. Soc.* 173 (1975).

[173] A. Gould, *Astrophys. J.* 379 (1991).

[174] G. D. Quinlan, *New Astron.* 1 (1996).

[175] J. N. Bahcall, P. Hut, et al., ApJ 290 (1985).

[176] D. P. Quinn, M. I. Wilkinson, et al., *Mon. Not. Roy. Astron. Soc.* 396 (2009).

[177] C. Allen and M. A. Monroy-Rodríguez, *Astrophys. J.* 790 (2014).

[178] M. A. Monroy-Rodríguez and C. Allen, *Astrophys. J.* 790 (2014).

[179] B. V. Lehmann, O. G. Ross, et al., *Mon. Not. Roy. Astron. Soc.* 505 (2021).

[180] J. G. Hills, AJ 99 (1990).

[181] Y. B. Ginat and H. B. Perets, MNRAS 508 (2021).

[182] H. Rein and S.-F. Liu, *Astron. Astrophys.* 537 (2012).

[183] H. Rein and D. S. Spiegel, *Mon. Not. Roy. Astron. Soc.* 446 (2014).

[184] Y. B. Ginat and H. B. Perets, *Physical Review X* 11 (2021).

[185] W. W. Zhu et al., *Mon. Not. Roy. Astron. Soc.* 482 (2019).

[186] P. C. C. Freire et al., *Mon. Not. Roy. Astron. Soc.* 412 (2011).

[187] M. E. Gonzalez et al., *Astrophys. J.* 743 (2011).

[188] E. C. Madsen, I. H. Stairs, et al., *Mon. Not. Roy. Astron. Soc.* 425 (2012).

[189] J. C. A. Miller-Jones et al., *Mon. Not. Roy. Astron. Soc.* 479 (2018).

[190] R. M. Shannon, S. Johnston, et al., *Mon. Not. Roy. Astron. Soc.* 437 (2014).

[191] G. Hobbs et al., *Class. Quant. Grav.* 27 (2010).

[192] R. N. Manchester et al., *Publ. Astron. Soc. Austral.* 30 (2013).

[193] M. A. McLaughlin, *Class. Quant. Grav.* 30 (2013).

[194] M. Kramer and D. J. Champion, *Class. Quant. Grav.* 30 (2013).

[195] J. H. Taylor and J. M. Weisberg, *Astrophys. J.* 253 (1982).

[196] D. C. Backer and R. W. Hellings, ARA&A 24 (1986).

[197] J. H. Taylor, *Phil. Trans. A. Math. Phys. Eng. Sci.* 341 (1992).

[198] J. H. Taylor, *Rev. Mod. Phys.* 66 (1994).

[199] I. H. Stairs, *Living Rev. Rel.* 6 (2003).

[200] M. Kramer et al., *Science* 314 (2006).

[201] J. M. Weisberg, D. J. Nice, et al., *Astrophys. J.* 722 (2010).

[202] N. Yunes and X. Siemens, *Living Rev. Rel.* 16 (2013).

[203] E. R. Siegel, M. P. Hertzberg, et al., *Mon. Not. Roy. Astron. Soc.* 382 (2007).

[204] N. Seto and A. Cooray, *Astrophys. J. Lett.* 659 (2007).

[205] H. A. Clark, G. F. Lewis, et al., *Mon. Not. Roy. Astron. Soc.* 456 (2016).

[206] K. Kashiyama and M. Oguri, arXiv: `1801.07847 [astro-ph.CO]` (2018).

[207] R. J. Jennings, J. M. Cordes, et al., arXiv: `1910.08608 [astro-ph.HE]` (2019).

[208] J. A. Dror, H. Ramani, et al., *Phys. Rev. D* 100 (2019).

[209] H. Ramani, T. Trickle, et al., arXiv: `2005.03030 [astro-ph.CO]` (2020).

[210] P. Pani, *Phys. Rev. D* 92 (2015).

[211] E. F. Keane et al., *PoS* AASKA14 (2015).

[212] L. Shao et al., *PoS* AASKA14 (2015).

[213] K. El-Badry, *New Astron. Rev.* 98 (2024).

[214] C. Boehm et al., arXiv: `1707.01348 [astro-ph.IM]` (2017).

[215] T. Kupfer, V. Korol, et al., *Mon. Not. Roy. Astron. Soc.* 480 (2018).

[216] A. Lamberts, S. Blunt, et al., *Mon. Not. Roy. Astron. Soc.* 490 (2019).

[217] J. W. Foster, D. Blas, et al., arXiv: `2504.16988 [gr-qc]` (2025).

[218] J. W. Foster, D. Blas, et al., arXiv: `2504.15334 [astro-ph.CO]` (2025).

[219] B. J. Carr and A. M. Green, arXiv: `2406.05736 [astro-ph.CO]` (2024).

[220] P. Montero-Camacho, X. Fang, et al., *JCAP* 08 (2019).

[221] S. M. Koushiappas and A. Loeb, *Phys. Rev. Lett.* 119 (2017).

[222] Q. Zhu, E. Vasiliev, et al., *Mon. Not. Roy. Astron. Soc.* 476 (2018).

[223] J. Stegmann, P. R. Capelo, et al., *Mon. Not. Roy. Astron. Soc.* 492 (2020).

[224] J. Yoo, J. Chaname, et al., *Astrophys. J.* 601 (2004).

[225] J. G. Hills, AJ 80 (1975).

[226] M. Valtonen and H. Karttunen. *The Three-Body Problem*. 2006.

[227] T. Prusti et al., *Astron. Astrophys.* 595 (2016).

[228] J. Binney and S. Tremaine. *Galactic Dynamics: Second Edition*. 2008.

[229] D. C. Heggie, P. Hut, et al., *Astrophys. J.* 467 (1996).

[230] Y. Ali-Haımoud and M. Kamionkowski, *Phys. Rev. D* 95 (2017).

[231] B. J. Carr, K. Kohri, et al., *Phys. Rev. D* 81 (2010).

[232] B. V. Lehmann, S. Profumo, et al., *JCAP* 04 (2018).

[233] S. Jung and C. S. Shin, *Phys. Rev. Lett.* 122 (2019).

[234] K. Griest, A. M. Cieplak, et al., *Astrophys. J.* 786 (2014).

[235] R. A. Allsman et al., *Astrophys. J. Lett.* 550 (2001).

[236] Z.-C. Chen and Q.-G. Huang, *JCAP* 08 (2020).

[237] B. P. Abbott et al., *Phys. Rev. Lett.* 123 (2019).

[238] B. J. Kavanagh, D. Gaggero, et al., *Phys. Rev. D* 98 (2018).

[239] B. J. Kavanagh (2019).

[240] B. Carr, K. Kohri, et al., *Rept. Prog. Phys.* 84 (2021).

[241] P. Mroz et al., arXiv: `2403.02386 [astro-ph.GA]` (2024).

[242] A. Esteban-Gutiérrez, E. Mediavilla, et al., *Astrophys. J.* 954 (2023).

[243] M. Gorton and A. M. Green, *JCAP* 08 (2022).

[244] T. Chiba and S. Yokoyama, *PTEP* 2017 (2017).

[245] M. Mirbabayi, A. Gruzinov, et al., *JCAP* 03 (2020).

[246] V. De Luca, V. Desjacques, et al., *JCAP* 05 (2019).

[247] R. Abbott et al., *Astrophys. J. Lett.* 900 (2020).

[248] A. Lamberts, S. Garrison-Kimmel, et al., *Mon. Not. Roy. Astron. Soc.* 480 (2018).

[249] C. J. Conselice, A. Wilkinson, et al., ApJ 830 (2016).

[250] T. R. Lauer et al., *Astrophys. J.* 906 (2021).

[251] J. Margot, P. Pravec, et al., *Asteroids IV* (2015).

[252] P. Pravec et al., Icarus 267 (2016).

[253] W. M. Grundy, K. S. Noll, et al., Icarus 334 (2019).

[254] K. S. Noll, M. E. Brown, et al., Space Sci. Rev. 219 (2023).

[255] K. J. Walsh and S. A. Jacobson, *Asteroids IV* (2015).

[256] K. Noll, W. M. Grundy, et al., *The Trans-Neptunian Solar System* (2020).

[257] J. Petit and O. Mousis, Icarus 168 (2004).

[258] W. J. Merline, S. J. Weidenschilling, et al., *Asteroids III* (2002).

[259] R. Caputo et al., *J. Astron. Telesc. Instrum. Syst.* 8 (2022).

[260] A. Arbey and J. Auffinger, *Eur. Phys. J. C* 79 (2019).

[261] A. Arbey and J. Auffinger, *Eur. Phys. J. C* 81 (2021).

[262] A. Arbey, J. Auffinger, et al., *PoS* ICHEP2020 (2021).

[263] M. Calzà and J. G. Rosa, arXiv: `2312.09261 [hep-ph]` (2023).

[264] Q. Taylor, G. D. Starkman, et al., *Phys. Rev. D* 109 (2024).

[265] A. Arbey and J. Auffinger, arXiv: `2006.02944 [gr-qc]` (2020).

[266] J. Scholtz and J. Unwin, *Phys. Rev. Lett.* 125 (2020).

[267] Y. N. Eroshenko, *New Astron.* 103 (2023).

[268] S. Seager. *Exoplanets*. 2010.

[269] J. N. Winn, AJ 164 (2022).

[270] M. L. Marcussen and S. H. Albrecht, AJ 165 (2023).

[271] G.-Y. Xiao, Y.-J. Liu, et al., *Research in Astronomy and Astrophysics* 23 (2023).

[272] A. T. Stevenson, C. A. Haswell, et al., MNRAS 526 (2023).

[273] M. Perryman, J. Hartman, et al., ApJ 797 (2014).

[274] Y. Bai, S. Lu, et al., *Phys. Rev. D* 108 (2023).

[275] Gaia Collaboration, A. G. A. Brown, et al., A&A 649 (2021).

[276] K. El-Badry, H.-W. Rix, et al., MNRAS 506 (2021).

[277] K. El-Badry et al., *Mon. Not. Roy. Astron. Soc.* 518 (2023).

[278] P. Panuzzo et al., *Astron. Astrophys.* 686 (2024).

[279] K. El-Badry, arXiv: `2404.13047 [astro-ph.SR]` (2024).

[280] A. Tanikawa, K. Hattori, et al., *Astrophys. J.* 946 (2023).

[281] T. Bensby, S. Feltzing, et al., *Astron. Astrophys.* 562 (2014).

[282] T. Sukhbold, T. Ertl, et al., *Astrophys. J.* 821 (2016).

[283] S. Justham, S. Rappaport, et al., *Mon. Not. Roy. Astron. Soc.* 366 (2006).

[284] S. Rastello, G. Iorio, et al., *Mon. Not. Roy. Astron. Soc.* 526 (2023).

[285] I. Kotko, S. Banerjee, et al., *arXiv e-prints* (2024).

[286] A. Tanikawa, S. Cary, et al., MNRAS 527 (2024).

[287] D. Marín Pina, S. Rastello, et al., A&A 688 (2024).

[288] G. Iorio et al., arXiv: `2404.17568 [astro-ph.GA]` (2024).

[289] J. Calcino, J. Garcia-Bellido, et al., *Mon. Not. Roy. Astron. Soc.* 479 (2018).

[290] B. Carr, S. Clesse, et al., *Phys. Dark Univ.* 31 (2021).

[291] K. Jedamzik, *JCAP* 09 (2020).

[292] K. Jedamzik, *Phys. Rev. Lett.* 126 (2021).

[293] R. G. Carlberg and C. J. Grillmair, *Astrophys. J.* 922 (2021).

[294] S. Mashchenko and A. Sills, *Astrophys. J.* 619 (2005).

[295] J. Shin, S. S. Kim, et al., *J. Korean Astron. Soc.* 46 (2013).

[296] A. Sollima, F. R. Ferraro, et al., MNRAS 462 (2016).

[297] K. J. Mack, J. P. Ostriker, et al., *Astrophys. J.* 665 (2007).

[298] M. Ricotti, *Astrophys. J.* 662 (2007).

[299] Y. N. Eroshenko, *Astron. Lett.* 42 (2016).

[300] A. Ireland, *Phys. Rev. D* 111 (2025).

[301] R. D. Mathieu, *Symposium - International Astronomical Union* 113 (1985).

[302] C. de Rham, J. T. Deskins, et al., *Rev. Mod. Phys.* 89 (2017).

[303] E. G. Adelberger, B. R. Heckel, et al., *Ann. Rev. Nucl. Part. Sci.* 53 (2003).

[304] T. Clifton, P. G. Ferreira, et al., *Phys. Rept.* 513 (2012).

[305] D. Brzeminski, Z. Chacko, et al., *Phys. Rev. D* 106 (2022).

[306] T. Damour and J. F. Donoghue, *Class. Quant. Grav.* 27 (2010).

[307] B. S. Acharya, A. Maharana, et al., *JHEP* 03 (2019).

[308] G. Kane, K. Sinha, et al., *Int. J. Mod. Phys. D* 24 (2015).

[309] D. Croon, A. E. Nelson, et al., *Astrophys. J. Lett.* 858 (2018).

[310] J. A. Dror, B. V. Lehmann, et al., *Phys. Rev. D* 104 (2021).

[311] J. Kopp, R. Laha, et al., *JHEP* 11 (2018).

[312] S. Alexander, E. McDonough, et al., *Class. Quant. Grav.* 35 (2018).

[313] T. K. Poddar, A. Ghoshal, et al., arXiv: `2302.14513 [hep-ph]` (2023).

[314] M. I. Gresham, V. S. H. Lee, et al., *JCAP* 02 (2023).

[315] A. Kehagias and K. Sfetsos, *Phys. Lett. B* 472 (2000).

[316] D. B. Kaplan and M. B. Wise, *JHEP* 08 (2000).

[317] P. Callin and F. Ravndal, *Phys. Rev. D* 70 (2004).

[318] S. Fichet, E. Megias, et al., *Phys. Rev. D* 107 (2023).

[319] S. Fichet, E. Megias, et al., *Phys. Rev. D* 107 (2023).

[320] P. Brax, S. Fichet, et al., *Phys. Rev. D* 97 (2018).

[321] H. Banks and M. Mccullough, *Phys. Rev. D* 103 (2021).

[322] A. Costantino, S. Fichet, et al., *JHEP* 03 (2020).

[323] X.-j. Xu and B. Yu, *JHEP* 02 (2022).

[324] C. Talmadge, J. P. Berthias, et al., *Phys. Rev. Lett.* 61 (1988).

[325] T. Johannsen, *Class. Quant. Grav.* 33 (2016).

[326] A. Hees et al., *Phys. Rev. Lett.* 118 (2017).

[327] C. M. Will, *Phys. Rev. D* 57 (1998).

[328] V. Cardoso, C. F. B. Macedo, et al., *JCAP* 05 (2016).

[329] Babak et al., *Phys. Rev. D* 95 (2017).

[330] C. P. L. Berry, S. A. Hughes, et al., arXiv: `1903.03686 [astro-ph.HE]` (2019).

[331] S. Barsanti, A. Maselli, et al., *Phys. Rev. Lett.* 131 (2023).

[332] A. Maselli, N. Franchini, et al., *Nature Astron.* 6 (2022).

[333] P. Amaro-Seoane et al., arXiv: `1702.00786 [astro-ph.IM]` (2017).

[334] M. Colpi et al., arXiv: `2402.07571 [astro-ph.CO]` (2024).

[335] A. Sesana et al., *Exper. Astron.* 51 (2021).

[336] B. C. Seymour and K. Yagi, *Phys. Rev. D* 102 (2020).

[337] R. D. Blandford and C. F. McKee, *The Astrophysical Journal* 255 (1982).

[338] B. M. Peterson, *Publications of the Astronomical Society of the Pacific* 105 (1993).

[339] J. K. Hoormann et al., *Monthly Notices of the Royal Astronomical Society* 487 (2019).

[340] A. Akylas, I. Papadakis, et al., *Astron. Astrophys.* 666 (2022).

[341] P. Amaro-Seoane, arXiv: `2011.03059 [gr-qc]` (2020).

[342] V. Vazquez-Aceves, Y. Lin, et al., *Astrophys. J.* 952 (2023).

[343] P. Amaro-Seoane, *Phys. Rev. D* 99 (2019).

[344] J. Binney and S. Tremaine. *Galactic dynamics*. 1987.

[345] M. C. Miller, T. Alexander, et al., arXiv: `0903.0285 [astro-ph.GA]` (2009).

[346] Z. Pan and H. Yang, *Phys. Rev. D* 103 (2021).

[347] R. Abuter et al., *Astron. Astrophys.* 677 (2023).

[348] GRAVITY Collaboration, *Astron. Astrophys.* 618 (2018).

[349] R. Abuter et al., *Astron. Astrophys.* 615 (2018).

[350] S. Thater, D. Krajnović, et al., *Astron. Astrophys.* 625 (2019).

[351] C.-P. Ma, J. E. Greene, et al., *The Astrophysical Journal* 795 (2014).

[352] N. J. McConnell and C.-P. Ma, *The Astrophysical Journal* 764 (2013).

[353] B. M. Peterson, L. Ferrarese, et al., *The Astrophysical Journal* 613 (2004).

[354] M. C. Bentz and S. Katz, *Publications of the Astronomical Society* 127 (2015).

[355] U. Malik et al., *Mon. Not. Roy. Astron. Soc.* 520 (2023).

[356] Y. Shen et al., arXiv: `2305.01014 [astro-ph.GA]` (2023).

[357] L. S. Finn and K. S. Thorne, *Phys. Rev. D* 62 (2000).

[358] S. A. Teukolsky, *Astrophys. J.* 185 (1973).

[359] S. L. Detweiler, *The Astrophysical Journal* 225 (1978).

[360] M. Shibata, *Phys. Rev. D* 50 (1994).

[361] K. Glampedakis and D. Kennefick, *Phys. Rev. D* 66 (2002).

[362] Ø. Christiansen, J. Beltrán Jiménez, et al., *Class. Quant. Grav.* 38 (2021).

[363] P. K. Gupta, T. F. M. Spieksma, et al., *Phys. Rev. D* 104 (2021).

[364] L. Liu, Z.-K. Guo, et al., *Phys. Rev. D* 102 (2020).

[365] L. Liu, Ø. Christiansen, et al., *Phys. Rev. D* 102 (2020).

[366] L. Liu and S. P. Kim, *JCAP* 03 (2022).

[367] C. Zhang and Y. Gong, *Phys. Rev. D* 105 (2022).

[368] M. Sasaki and T. Nakamura, *Prog. Theor. Phys.* 67 (1982).

[369] M. Maggiore. Oxford University Press, 2007.

[370] C. J. Moore, R. H. Cole, et al., *Class. Quant. Grav.* 32 (2015).

[371] Y. A. El-Neaj et al., *EPJ Quant. Technol.* 7 (2020).

[372] M. A. Fedderke, P. W. Graham, et al., *Phys. Rev. D* 105 (2022).

[373] L. Barack and C. Cutler, *Phys. Rev. D* 69 (2004).

[374] C. Zhang, Y. Gong, et al., *Physical Review D* 103 (2021).

[375] B. P. Abbott et al., *Nature* 551 (2017).

[376] E. Barausse, V. Cardoso, et al., *Phys. Rev. D* 89 (2014).

[377] E. Berti et al., *Class. Quant. Grav.* 32 (2015).

[378] S. Kejriwal, L. Speri, et al., arXiv: `2312.13028 [gr-qc]` (2023).

[379] E. Barausse, V. Cardoso, et al., *J. Phys. Conf. Ser.* 610 (2015).

[380] L. B. Fries et al., *The Astrophysical Journal* 948 (2023).

[381] G. Bertone, D. Hooper, et al., *Phys. Rept.* 405 (2005).

[382] J. L. Feng, *Ann. Rev. Astron. Astrophys.* 48 (2010).

[383] K. A. Olive, arXiv: `astro-ph/0301505` (2003).

[384] N. Aghanim et al., *Astron. Astrophys.* 641 (2020).

[385] G. Hinshaw et al., *Astrophys. J. Suppl.* 208 (2013).

[386] G. Steigman and M. S. Turner, *Nucl. Phys. B* 253 (1985).

[387] L. Bergström, *Rept. Prog. Phys.* 63 (2000).

[388] E. Aprile et al., *Phys. Rev. Lett.* 121 (2018).

[389] D. S. Akerib et al., *Nucl. Instrum. Meth. A* 953 (2020).

[390] M. Aaboud et al., *Eur. Phys. J. C* 77 (2017).

[391] F. D'Eramo and J. Thaler, *JHEP* 06 (2010).

[392] J. Huang and Y. Zhao, *JHEP* 02 (2014).

[393] K. Agashe, Y. Cui, et al., *JCAP* 10 (2014).

[394] J. Berger, Y. Cui, et al., *JCAP* 02 (2015).

[395] K. Kong, G. Mohlabeng, et al., *Phys. Lett. B* 743 (2015).

[396] A. Bhattacharya, R. Gandhi, et al., *JCAP* 03 (2015).

[397] J. Kopp, J. Liu, et al., *JHEP* 04 (2015).

[398] J. F. Cherry, M. T. Frandsen, et al., *Phys. Rev. Lett.* 114 (2015).

[399] L. Necib, J. Moon, et al., *Phys. Rev. D* 95 (2017).

[400] H. Alhazmi, K. Kong, et al., *JHEP* 04 (2017).

[401] D. Kim, J.-C. Park, et al., *Phys. Rev. Lett.* 119 (2017).

[402] A. Bhattacharya, R. Gandhi, et al., *JCAP* 05 (2017).

[403] Y. Cui, M. Pospelov, et al., *Phys. Rev. D* 97 (2018).

[404] G. F. Giudice, D. Kim, et al., *Phys. Lett. B* 780 (2018).

[405] A. Chatterjee, A. De Roeck, et al., *Phys. Rev. D* 98 (2018).

[406] D. Kim, K. Kong, et al., *JHEP* 08 (2018).

[407] M. Aoki and T. Toma, *JCAP* 10 (2018).

[408] D. McKeen and N. Raj, *Phys. Rev. D* 99 (2019).

[409] D. Kim, J.-C. Park, et al., *Phys. Rev. D* 100 (2019).

[410] J. Berger, Y. Cui, et al., *Phys. Rev. D* 103 (2021).

[411] L. Heurtier, D. Kim, et al., *Phys. Rev. D* 100 (2019).

[412] D. Kim, P. A. N. Machado, et al., *JHEP* 07 (2020).

[413] A. De Roeck, D. Kim, et al., *JHEP* 11 (2020).

[414] B. Fornal, P. Sandick, et al., *Phys. Rev. Lett.* 125 (2020).

[415] H. Alhazmi, D. Kim, et al., *JHEP* 05 (2021).

[416] S. Chigusa, M. Endo, et al., *JCAP* 10 (2020).

[417] D. Borah, M. Dutta, et al., *Phys. Lett. B* 820 (2021).

[418] D. Borah, M. Dutta, et al., *Nucl. Phys. B* 979 (2022).

[419] T. Toma, *Phys. Rev. D* 105 (2022).

[420] T. Bringmann and M. Pospelov, *Phys. Rev. Lett.* 122 (2019).

[421] Y. Ema, F. Sala, et al., *Phys. Rev. Lett.* 122 (2019).

[422] C. V. Cappiello and J. F. Beacom, *Phys. Rev. D* 100 (2019).

[423] J. B. Dent, B. Dutta, et al., *Phys. Rev. D* 101 (2020).

[424] W. Wang, L. Wu, et al., *JHEP* 12 (2020).

[425] S.-F. Ge, J. Liu, et al., *Phys. Rev. Lett.* 126 (2021).

[426] Q.-H. Cao, R. Ding, et al., *Chin. Phys. C* 45 (2021).

[427] Y. Jho, J.-C. Park, et al., *Phys. Lett. B* 811 (2020).

[428] W. Cho, K.-Y. Choi, et al., *Phys. Rev. D* 102 (2020).

[429] J. B. Dent, B. Dutta, et al., *Phys. Rev. D* 103 (2021).

[430] N. F. Bell, J. B. Dent, et al., *Phys. Rev. D* 104 (2021).

[431] C. Xia, Y.-H. Xu, et al., *JCAP* 02 (2022).

[432] Y. Jho, J.-C. Park, et al., arXiv: 2101.11262 [hep-ph] (2021).

[433] A. Das and M. Sen, *Phys. Rev. D* 104 (2021).

[434] W. Chao, T. Li, et al., arXiv: 2108.05608 [hep-ph] (2021).

[435] C. Kouvaris, *Phys. Rev. D* 92 (2015).

[436] P.-K. Hu, A. Kusenko, et al., *Phys. Lett. B* 768 (2017).

[437] H. An, M. Pospelov, et al., *Phys. Rev. Lett.* 120 (2018).

[438] T. Emken, C. Kouvaris, et al., *Phys. Rev. D* 97 (2018).

[439] R. Calabrese, M. Chianese, et al., *Phys. Rev. D* 105 (2022).

[440] J.-W. Wang, A. Granelli, et al., *Phys. Rev. Lett.* 128 (2022).

[441] J. Alvey, M. Campos, et al., *Phys. Rev. Lett.* 123 (2019).

[442] L. Su, W. Wang, et al., *Phys. Rev. D* 102 (2020).

[443] J. F. Acevedo, J. Berger, et al., *JHEP* 11 (2024).

[444] D. Alonso-González, D. Cerdeño, et al., *Phys. Rev. D* 111 (2025).

[445] D. Alonso-González, D. Cerdeño, et al., *Phys. Rev. D* 111 (2025).

[446] F. Lin, N. Liu, et al., arXiv: 2504.13007 [hep-ph] (2025).

[447] W. Yin, *EPJ Web Conf.* 208 (2019).

[448] J. Jaeckel and W. Yin, *JCAP* 02 (2021).

[449] C. Kachulis et al., *Phys. Rev. Lett.* 120 (2018).

[450] C. Ha et al., *Phys. Rev. Lett.* 122 (2019).

[451] X. Cui et al., *Phys. Rev. Lett.* 128 (2022).

[452] K. Abe et al., *Phys. Rev. Lett.* 130 (2023).

[453] X. Shang et al., *Phys. Rev. Lett.* 133 (2024).

[454] C. Giunti and C. W. Kim. *Fundamentals of Neutrino Physics and Astrophysics*. 2007.

[455] K. Zuber. *Neutrino Physics*. Boca Raton: Taylor & Francis, 2020.

[456] D. Casper, *Nucl. Phys. B Proc. Suppl.* 112 (2002).

[457] Y. Fukuda et al., *Phys. Rev. Lett.* 81 (1998).

[458] K. Abe et al., *Phys. Rev. D* 83 (2011).

[459] K. Abe et al., *Phys. Rev. D* 91 (2015).

[460] E. Richard et al., *Phys. Rev. D* 94 (2016).

[461] Q. R. Ahmad et al., *Phys. Rev. Lett.* 87 (2001).

[462] S. Andringa et al., *Adv. High Energy Phys.* 2016 (2016).

[463] G. Alimonti et al., *Nucl. Instrum. Meth. A* 600 (2009).

[464] H. Back et al., *JINST* 7 (2012).

[465] S. Abe et al., *Phys. Rev. Lett.* 100 (2008).

[466] A. Gando et al., *Phys. Rev. C* 92 (2015).

[467] K. Asakura et al., *Astrophys. J.* 818 (2016).

[468] M. G. Aartsen et al., *JINST* 9 (2014).

[469] M. G. Aartsen et al., *Science* 342 (2013).

[470] M. G. Aartsen et al., *JINST* 12 (2017).

[471] F. An et al., *J. Phys. G* 43 (2016).

[472] Z. Djurcic et al., arXiv: `1508.07166 [physics.ins-det]` (2015).

[473] C. Guo, arXiv: `1910.10343 [physics.ins-det]` (2019).

[474] L. M. Krauss, S. L. Glashow, et al., *Nature* 310 (1984).

[475] G. L. Fogli, E. Lisi, et al., *Phys. Rev. D* 86 (2012).

[476] S. Horiuchi, P. J. Humphrey, et al., *Phys. Rev. D* 89 (2014).

[477] B. Abi et al., arXiv: `1807.10327 [physics.ins-det]` (2018).

[478] B. Abi et al., arXiv: `1807.10340 [physics.ins-det]` (2018).

[479] B. Abi et al., *JINST* 15 (2020).

[480] B. Abi et al., arXiv: `2002.03005 [hep-ex]` (2020).

[481] B. Abi et al., *JINST* 15 (2020).

[482] K. Abe et al., arXiv: `1109.3262 [hep-ex]` (2011).

[483] K. Abe et al., *PTEP* 2018 (2018).

[484] K. Abe et al., arXiv: `1805.04163 [physics.ins-det]` (2018).

[485] H. A. Bethe, *Rev. Mod. Phys.* 62 (1990).

[486] A. Burrows, *Rev. Mod. Phys.* 85 (2013).

[487] P. J. E. Peebles, *Astrophysical Journal* 277 (1984).

[488] D. K. Ghosh, T. Gupta, et al., *Phys. Rev. D* 111 (2025).

[489] C. Blanco, M. Escudero, et al., *JCAP* 11 (2019).

[490] K. Murase, *Phys. Rev. D* 78 (2008).

[491] K. Blum and D. Kushnir, *Astrophys. J.* 828 (2016).

[492] A. M. Suliga, I. Tamborra, et al., *JCAP* 08 (2020).

[493] T. Fischer, N.-U. F. Bastian, et al., *Nature Astron.* 2 (2018).

[494] G. G. Raffelt, *Phys. Rept.* 198 (1990).

[495] W. DeRocco, P. W. Graham, et al., *Phys. Rev. D* 100 (2019).

[496] B. P. Abbott et al., *Phys. Rev. Lett.* 116 (2016).

[497] T. Akutsu et al., *Class. Quant. Grav.* 36 (2019).

[498] M. G. Aartsen et al., *Astrophys. J.* 843 (2017).

[499] B. Dutta, D. Kim, et al., *JHEP* 01 (2022).

[500] B. Dutta, W.-C. Huang, et al., *Phys. Rev. Lett.* 133 (2024).

[501] S. M. Adams, C. Kochanek, et al., *The Astrophysical Journal* 778 (2013).

[502] A. Abed Abud et al., *JINST* 19 (2024).

[503] B. Abi et al., *Eur. Phys. J. C* 81 (2021).

[504] G. Zhu, S. W. Li, et al., *Phys. Rev. C* 99 (2019).

[505] K. Abe et al., *Astrophys. J.* 916 (2021).

[506] X. Fang, Y. Zhang, et al., *JINST* 15 (2020).

[507] A. Abusleme et al., *Prog. Part. Nucl. Phys.* 123 (2022).

[508] S. Navas et al., *Phys. Rev. D* 110 (2024).

[509] R. L. Workman et al., *PTEP* 2022 (2022).

[510] J. A. Formaggio and G. P. Zeller, *Rev. Mod. Phys.* 84 (2012).

[511] M. Honda, M. Sajjad Athar, et al., *Phys. Rev. D* 92 (2015).

[512] Z. Yang et al., *Phys. Rev. D* 109 (2024).

[513] G. Krnjaic and S. D. McDermott, *Phys. Rev. D* 101 (2020).

[514] J. C. Wheeler and E. Chatzopoulos, *Astronomy & Geophysics* 64 (2023).

[515] H. Saio, D. Nandal, et al., *Mon. Not. Roy. Astron. Soc.* 526 (2023).

[516] J. G. Hills, AJ 88 (1983).

[517] M. Xiang et al., *Astrophys. J. Suppl.* 237 (2018).

[518] M. S. Nitschai, A.-C. Eilers, et al., ApJ 916 (2021).

[519] H.-W. Rix and J. Bovy, *Astron. Astrophys. Rev.* 21 (2013).

[520] G. Bozzola and V. Paschalidis, *Phys. Rev. Lett.* 126 (2021).

[521] S. Peirani and J. A. de Freitas Pacheco, *Phys. Rev. D* 77 (2008).

[522] A. S. Eddington. *The Internal Constitution of the Stars*. 1926.

[523] K. Inayoshi, E. Visbal, et al., *Ann. Rev. Astron. Astrophys.* 58 (2020).

[524] M. A. Abramowicz, B. Czerny, et al., *The Astrophysical Journal* 332 (1988).

[525] M. Volonteri, J. Silk, et al., *Astrophys. J.* 804 (2015).

[526] K. Inayoshi, Z. Haiman, et al., *Mon. Not. Roy. Astron. Soc.* 459 (2016).

[527] M. J. Hardcastle and J. H. Croston, *New Astron. Rev.* 88 (2020).